Università degli Studi di Firenze
Dottorato di Ricerca in Scienze Chimiche XXI Ciclo

Synthesis and Characterization of Metallic Nanoparticles for Innovative Applications

Ester Falletta

Tutor: Prof. Piero Baglioni

PhD Coordinators: Prof. Gianni Cardini

Prof. Giacomo Martini

CHIM/02-CHIMICA FISICA

Index

1. Introduction to Metallic Nanoparticles

2. Clusters of Poly(acrylates) and Silver Nanoparticles

3. Tunable Gold Nanostructures

4. Magnetic Nanocomposites

1. Metallic Nanoparticles

1.1. Introduction

The interest in nanoscale materials arises from the fact that new properties are acquired at this length scale and, equally important, that these properties change with size or shape. The change in the properties at this length scale is not a result of scaling factors but it results from different causes in different materials. As noble metals are reduced in size to tens of nanometers, for example, a new very strong absorption is observed resulting from the collective oscillation of the electrons in the conduction band from one surface of the particle to the other. This oscillation has a frequency that absorbs the visible light. This is called "the surface plasmon absorption". This strong absorption, giving rise to vivid characteristic color, has been observed and used, but not understood, since the 17^{th} century. The gold particles, giving rise to a brilliant rose color, have been used throughout Europe in stained glass windows of cathedrals and by the Chineses in coloring vases and other ornaments. In transition metal nanoparticles, the decrease in the particle size to the nanometer scale increases the surface-to-volume ratio. This, together with our ability to make them in different sizes and shapes, makes them potentially useful in the field of catalysis. The past couple of decades have witnessed an exponential growth of activities in this field worldwide, driven both by the excitement of understanding new science and by the potential hope for applications and economic impacts. The largest activity in this field at this time has been in the synthesis of new nanoparticles of different sizes and new shapes. The unraveling of the physics of these particles and the application of computational methods to understand their behavior is being investigated. Self-assembly of these nanoparticles by different techniques, either from the bottom-up techniques (assembling particles synthesized in solution) or from the top-down techniques (different lithographic methods), is being pursued. Although many future

applications will make use of the properties of the individual nanoparticles (sensors, medical diagnostics, homogeneous catalysis, etc.), there are other important applications that would require self-assembled nanoparticles (nanoelectronics, optoelectronics, photonics, heterogeneous catalysis, etc). Besides achieving new properties, creating novel nanostructures requires new understanding of the properties of their surfaces. In most of their potential applications, the quality and the structure of the surface of nanoparticles will undoubtedly play the pivotal role in determining their functions. Being small could make the nanoparticle unstable due to the high surface energy and the large surface curvature. Thus, the properties change as these particles are used. Not only could the surface structure and shape change, but the chemical nature of their surface could be altered, too. Thus, it is clear that using these nanoparticles fully and effectively will depend on our understanding of their general properties and also of their surface properties and stability.

1.2. Nanoparticles' syntheses

Many synthetic method to produce size and shape-tunable metallic nanostructures have been developed: syntheses by coprecipitation, sol-gel processing, microemulsions, hydrothermal/solvothermal methods, templated syntheses, and biomimetic syntheses are the most common method used.

1.2.1. Nanoparticle Synthesis by Coprecipitation

Many of the earliest syntheses of nanoparticles were achieved by the coprecipitation of sparingly soluble products from aqueous solutions followed by thermal decomposition of those products to oxides. Coprecipitation reactions involve the simultaneous occurrence of nucleation, growth, coarsening, and/or agglomeration processes. Due to the difficulties in isolating each process for independent study, the fundamental mechanisms of coprecipitation are still not

thoroughly understood.

1.2.1.1. Theory and Thermodynamics of Coprecipitation

The theory of coprecipitation is not a trivial subject. Numerous books [1,2] and review articles [3-7] cover this topic much more thoroughly than the discussion reported here. As a brief overview, coprecipitation reactions tend to exhibit the following characteristics:
(i) The products of precipitation reactions are generally sparingly soluble species formed under conditions of high supersaturation.
(ii) Such conditions dictate that nucleation will be a key step of the precipitation process and that a large number of small particles will be formed.
(iii) Secondary processes, such as Ostwald ripening and aggregation, will dramatically affect the size, morphology, and properties of the products.
(iv) The supersaturation conditions necessary to induce precipitation are usually the result of a chemical reaction.
As such, any reaction conditions influencing the mixing process, such as rate of reactant addition and stirring rate, must be considered relevant to product size, morphology, and particle size distribution. Although precipitation can be induced in any number of ways, chemical reactions are by far the most common method for the synthesis of nanoparticles. Generally, chemical reactions are chosen that result in products with low solubilities, such that the solution quickly reaches a supersaturated condition. The chemical reactions used to induce coprecipitation can take numerous forms. For illustrative purposes, we consider the case of a simple addition reaction for the formation of an electrolyte, A_xB_y:

$$xA^{y+}(aq) + yB^{x-}(aq) \leftrightarrows A_xB_y(s) \qquad (1.1)$$

The equilibrium relationship between the product and its reactants is expressed as the solubility product constant, K_{sp}:

$$K_{sp} = (a_A)^x(a_B)^y \qquad (1.2)$$

where a_A and a_B are the activities of cation A and anion B in aqueous solution. K_{sp} values (and therefore solubilities) tend to be very low for many hydroxides, carbonates, oxalates, and chalcogenides in aqueous solutions, and the precipitation reactions for several of these species are specifically discussed in later sections. Tables of K_{sp} values are widely available in reference volumes and in textbooks. Solubility data for compounds in solvents other than water are substantially more sparse. Beyond simple addition/exchange reactions, precipitation can be induced by numerous other methods, such as chemical reduction, photoreduction, oxidation, and hydrolysis. Alternatively, precipitation can be induced by altering other parameters related to solubility, most notably temperature and concentration. When the product contains only one or two elements (e.g. a metal, binary oxide, etc.), precipitation reactions are relatively straightforward. In more complicated ternary and quarternary systems, the process becomes more complex, as multiple species must be precipitated simultaneously (hence, the term *coprecipitation*). Merely inducing precipitation of a compound, however, does not guarantee that the product will be nanoparticulate and/or monodispersed. The processes of nucleation and growth govern the particle size and morphology of products in precipitation reactions. When precipitation begins, numerous small crystallites initially form (nucleation), but they tend to quickly aggregate together to form larger, more thermodynamically stable particles (growth).

Nucleation

The key to any precipitation process is the degree of supersaturation, S, given by

$$S = \frac{a_A a_B}{K_{SP}} \tag{1.3}$$

where a_A and a_B are the activities of solutes A and B and K_{sp}

is the solubility product constant, or alternatively by $S = C/C_{eq}$, where C and C_{eq} are the solute concentrations at saturation and at equilibrium, respectively. Indeed, the literature frequently refers to the difference in C and C_{eq}, $\Delta C = C - C_{eq}$, as the "driving force" for precipitation [5]. As nucleation begins in a supersaturated solution, there exists an equilibrium critical radius, R^*:

$$R^* = \frac{\alpha}{\Delta C} \tag{1.4}$$

The term α is given by

$$\alpha = \left(\frac{2\sigma_{SL}}{kT \ln S} \right) \nu C_\infty \tag{1.5}$$

where σ_{SL} is the surface tension at the solid-liquid interface, ν is the atomic volume of solute, k is the Boltzmann constant, T is temperature, and S is the supersaturation as defined in eq. 1.3. Nucleated particles with $R > R^*$ will continue to grow, while those with $R < R^*$ will dissolve. The activation energy of the cluster formation is given by [7]:

$$\Delta G = \frac{4\pi\sigma_{SL} R^{*2}}{3} = \frac{16\pi\sigma_{SL}{}^3 \nu^2}{3k^2T^2 \ln^2 S} \tag{1.6}$$

Thus, for stationary conditions, the homogeneous nucleation rate, R_N, is then:

$$R_N = \left(\frac{dN}{dt} \right) \frac{1}{V} = A \exp\left[\frac{-(\Delta G^*)}{kT} \right] \tag{1.7}$$

where N is the number of nuclei formed per unit time per unit volume, V, and A is a pre-exponential factor typically ranging from 10^{25} to 10^{56} s^{-1} m^{-3}.
Combining eqs. 1.6 and 1.7:

$$R_N = A\exp\left(\frac{-16\pi\sigma_{SL}{}^3 v^2}{3k^3T^3\ln^2 S}\right) \tag{1.8}$$

revealing that R_N is an exponential function of S. It follows that R_N remains negligible until a certain critical supersaturation, S^*, is reached.

Growth

The growth process of the precipitated particles is as crucial as nucleation. The process can be either diffusion-limited or reaction-limited. Experimental evidence suggests, however, that the overwhelming majority of precipitation reactions are diffusion-limited. As such, concentration gradients and temperature become the predominant factors determining growth rate as new material is supplied to the particle surface via long-distance mass transfer. The balance of that material, as a monomer, crossing the surface of a spherical crystallite is given by:

$$\frac{dr}{dt} = D\Omega\left(\frac{1}{\delta}+\frac{1}{r}\right)\left(C_b - C_i\right) \tag{1.9}$$

where r is the crystal radius, t is time, D is the diffusivity of the monomer, Ω is the molar volume, and δ_i is the thickness of the layer over which the concentration changes from C_b, the bulk solute concentration, to C_i, the solute concentration in the vicinity of the crystal surface [8, 9].
The relationship between monomer concentration and crystal size is established by the Gibbs-Thomson equation [10]:

$$C_e(r) \cong C_\infty\left(\frac{1+2\Omega\gamma}{R_G TR}\right) \tag{1.10}$$

where γ is the interfacial tension, R_G is the universal gas constant, T is the temperature, and C_∞ is a constant.
Finally, the relationship between the rate of growth, G, and the supersaturation ratio, S, can be expressed as a power-law

equation [5]:

$$G = \frac{dL}{dt} = k_G S^g \qquad (1.11)$$

where k_G is the growth rate constant and g is the growth order.

Ostwald Ripening

Ostwald ripening (also referred to as *coarsening*) is the phenomenon by which smaller particles are essentially consumed by larger particles during the growth process and is itself a topic of considerable investigation and postulation [11-17]. This behavior can, to some extent, be predicted by eq 1.10, which establishes that the solubility of particles increases with decreasing particle size. A detailed mathematical description of Ostwald ripening was first developed by Lifshitz and Slyozov and also independently by Wagner; their combined models are today referred to as *LSW theory* [8, 9]. Some authors have taken exception to various approximations and assumptions of LSW theory, most notably the theory's failure to adequately account for cooperative effects between nuclei and the theory's assumption of a steady change in solute concentration with time [18]. Those authors' criticisms are justified, insofar as the assumptions in LSW theory have lead to frequent disagreements between theoretical and experimental results. Nonetheless, most competing or expanded theories of Ostwald ripening are still based on the original LSW model, and for the purposes of this discussion, the theory is adequate to make several important points concerning the precipitation of nanoparticles. The principles of LSW theory, however, are summarized as follows:
(i) For a diffusion-controlled process, the average radius of the precipitate particles, $\bar{r}$, as a function of time, t, is [15]:

$$\bar{r}(t) = \sqrt[3]{Kt} \qquad (1.12)$$

where K is the coarsening rate, given by $4\alpha D/9$, and D is the diffusion current of solute across the grain boundary. Particle size is thus proportional to the cube-root of time.
(ii) During diffusion-controlled ripening, the number density N of nucleated particles decays as [15]

$$N(t) = \frac{0.22Q_0}{\bar{R}(t)^3} = \frac{0.22}{2D\alpha t} \tag{1.13}$$

where Q_0 is the total initial supersaturation. The number of solute particles therefore decreases as t^{-1} during ripening.
(iii) The size distribution of particles is given by

$$f(R,t) = \left[\frac{N(t)}{\bar{R}(t)}\right] p_0(\rho(t)) \tag{1.14}$$

where $\rho(t) \equiv R/\bar{R}(t)$ and $p_0(\rho)$ is a time-independent function of the absolute dimension of the grains, ρ.
Equations 1.1-1.14 provide several useful insights into the precipitation of nanoparticles. To produce nanoparticles, the nucleation process must be relatively fast while the growth process remains relatively slow. The formation of particles with a narrow size distribution further requires that the nuclei of all species present form simultaneously and without subsequent nucleation of smaller particles. Park et al. have recently published a study specifically addressing the coprecipitation of nanoparticles [19].

Growth Termination and Nanoparticle Stabilization

Due to the thermodynamics discussed that favor the maximization of the surface/volume ratio, the agglomeration of small particles precipitated from solutions is practically inevitable in the absence of a stabilizer. For the purposes of this discussion, we are primarily interested in nanoparticles that can be prepared as stable colloids or isolated as powdered products. It should be pointed out, however, that agglomeration can occur at any stage during synthesis; aggregation and agglomeration of particles during

precipitation is itself a subject of investigation [20].
There are generally two approaches to nanoparticle stabilization: (a) steric repulsion between particles caused by surfactants, polymers, or other organic species bound to the nanoparticles' surfaces (generically referred to as *capping ligands*) and (b) electrostatic (van der Waals) repulsions resulting from the chemisorption of charged species (usually, though not necessarily, H^+ or OH^-) at the surfaces. Scanning Tunnelling Microscopy and Transmission Electron Microscopy studies of Pd clusters capped with tetrabutylammonium bromide have shown that, at least in some cases, capping ligands indeed form monolayers at the particles' surfaces [21]. Steric stabilization is somewhat more common, probably due to issues concerning the chemical stability of the nanoparticles at very high or very low pH values.

1.2.1.2. Coprecipitation Synthetic Methods

Synthesis of Metals from Aqueous Solutions

Due to their widespread application as catalysts [22], metals precipitated from aqueous solutions continue to be a thoroughly investigated subject. The precipitation of metals from aqueous or nonaqueous solutions typically requires the chemical reduction of a metal cation. Reducing agents take many forms, the most common of which are gaseous H_2, solvated ABH_4 (A=alkali metal), hydrazine hydrate ($N_2H_4 \cdot H_2O$), and hydrazine dihydrochloride ($N_2H_4 \cdot 2HCl$).
For a typical reduction reaction of a transition metal cation,

$$M^{n+} + ne^- \rightarrow M^0 \qquad (1.15)$$

there must, of course, be a corresponding oxidation process of some species X, such that

$$X^m - ne^- \rightarrow X^{m-n} \qquad (1.16)$$

In order for the electron transfer to occur, the free energy

change, ΔG, must be favorable. As a matter of convention, the favorability of oxidation-reduction processes is reflected in the standard electrode potential, $E°$, of the corresponding electrochemical half-reaction.
Since the $E°$ values of all reactions are stated relative to that of H_2, the half-reaction and $E°$ for H_2 are, by definition,

$$2H^+ + 2e^- \leftrightarrows H_2 \qquad E_0 = 0.00\text{V} \qquad (1.17)$$

at standard temperature and pressure (STP). Numerous metal ions can be reduced from aqueous solution to the metallic state in the presence of gaseous H_2 with proper adjustment of pH [23, 24]. The electrochemical half-reaction and $E°$ for borohydride ion are given by:

$$B(OH)_3 + 7H^+ + 8e^- \leftrightarrows BH_4^- + 3H_2O \qquad E^0 = -0.481\text{V} \qquad (1.18)$$

Borohydride ions, however, should be employed judiciously, as they are known to reduce some cations to metal borides, particularly in aqueous systems [25-28]. The use of borohydride specifically for the precipitation of metal nanoparticles has recently been reviewed [29].
Hydrazine hydrate is freely soluble in water, but since N_2H_4 is basic, the chemically active free-ion is normally represented as $N_2H_5^+$:

$$N_2H_4 \cdot H_2O \leftrightarrows N_2H_5^+ + OH^- \qquad (1.19)$$

or, in the case of hydrazine dihydrochloride,

$$N_2H_4 \cdot 2HCl \leftrightarrows N_2H_5^+ + H^+ + 2Cl^- \qquad (1.20)$$

The standard reduction potential for the hydrazinium ion, $N_2H_5^+$, is

$$N_2 + 5H^+ + 4e^- \leftrightarrows N_2H_5^+ \qquad E° = -0.23\text{ V} \qquad (1.21)$$

In theory, the reduction of any metal with an $E°$ more positive than -0.481 V or -0.23 V, respectively, should be possible at room temperature, given a sufficient excess of reducing agent

and proper control of pH. With respect to precipitating metals from solution, this would obviously include many first-row transition metal ions, such as Fe^{2+}, Fe^{3+}, Co^{2+}, Ni^{2+}, and Cu^{2+}, but also many second- and third-row transition metals, as well as most post-transition elements and a few nonmetals.

As a practical matter, the reduction of some metal ions with $E° > -0.481$ V is either not feasible or exceedingly difficult, but this is usually due to the instability of the cation in aqueous environments. However, in some instances, transition metal cations, such as Rh^{3+}, form stable complexes with hydrazine, thereby greatly limiting the available options for carrying out a reduction [30]. We should further emphasize that consideration of pH and relative redox potentials is, at best, only a guide for predicting which metals may or may not be prepared by this method.

The reduction of gold cations to gold metal is easily the single most thoroughly studied metal precipitation reaction. Gold cations, usually in the form of $AuCl_4^-$, are easily reduced by gaseous H_2:

$$2AuCl_4^-(aq) + 3H_2(g) \leftrightarrows 2Au(s) + 6H^+(aq) + 8Cl^-(aq) \quad (1.22)$$

although $AuCl_4^-$ is so strongly oxidizing ($E°=+1.002$V) that weaker reducing agents such as carboxylates or alcohols are usually sufficient. Tan et al. have recently reported the synthesis of Au, Pt, Pd, and Ag nanoparticles by reduction with potassium bitartrate; all of the products formed stable colloids with the addition of a suitable stabilizing agent [31].

In many cases, an organic capping agent that is normally used to prevent agglomeration can also serve as the reducing agent. This is the case in the well-known Turkevich process for the synthesis of gold colloids [32]. In their 1951 paper, Turkevich et al. described a synthetic method for colloidal gold prepared by boiling a mixture of dilute $HAuCl_4$ and sodium citrate [33]. This method is still widely used today.

Normally, if thiol stabilizing agents are used, the reduction of $AuCl_4^-$ in aqueous solution must be performed with borohydride or similar reducing agents because the complexes formed between $AuCl_4^-$ and thiols are too stable to be reduced by citrate or other weak reducing agents.

Yonezawa et al., however, have demonstrated that reduction of $AuCl_4^-$ with citrate in the presence of a thiol is possible, if the thiol and citrate are added to the gold solution simultaneously [34]. Gold colloids with 2-10 nm dimensions are achievable with this method, and narrow size distributions are possible at high [thiol]/[Au] ratios.

The reduction of metals with highly negative reduction potentials requires reducing agents with considerably stronger reducing ability than that afforded by most amines, hydroxycarboxylic acids, or alcohols. The reduction of ions such as Ni^{2+} ($E°$= -0.257 V), Co^{2+} ($E°$= -0.28 V), and Fe^{2+} ($E°$= -0.447 V) is therefore typically performed with borohydride salts (eq. 1.18).

Silver can similarly be reduced with borohydride from aqueous Ag^+ in a solution containing bis (11- trimethyl ammoniumdecanoylaminoethyl) disulfide dibromide (TADDD), producing monodisperse nanoparticles as small as 3.3 nm [35]. In this case, the excess borohydride reduces the disulfide to a thiol that serves as a capping ligand. The particles are easily redispersed into stable colloids in slightly acidified water.

Precipitation of Metals by Radiation-Assisted Reduction

The most obvious example of radiation-assisted reduction is the photoreduction of aqueous $AgNO_3$ solutions upon exposure to UV light. Huang et al. adapted this method to the synthesis of Ag nanoparticles by exposing a solution of $AgNO_3$ to 243 nm radiation in the presence of poly(*N*-vinylpyrrolidone) (PVP) as stabilizer [36]. The average particle size could be varied from 15 to 22 nm by adjusting the [PVP]/ [Ag+] ratio.

At the extreme end of radiation-assisted reductions, all of the noble metals, as well as many other electronegative metals, can be reduced in aqueous solutions by exposure to γ-radiation. γ-rays decompose H_2O to H_2, H_2O_2, •OH and •H radicals, and aqueous, solvated electrons [37]:

$$H_2O \xrightarrow{\gamma-rays} \bullet OH(2.8), e_{aq}^-(2.7), H_2O_2(0.71), \bullet H(0.55), H_2(0.45)$$

where the numbers in parentheses represent the radical chemical yields expressed as the number of species per 100 eV of energy absorbed.
The reactions are usually performed under a nitrous oxide atmosphere that acts as a scavenger for the hydrated electrons (e_{aq}^-):

$$N_2O + e_{aq}^- + H_2O \rightarrow N_2 + OH^- + \bullet OH \qquad (1.23)$$

The •OH and •H radicals are subsequently scavenged by short-chain alcohols such as methanol:

$$\bullet OH + CH_3OH \rightarrow H_2O + \bullet CH_2OH \qquad (1.24)$$
$$\bullet H + CH_3OH \rightarrow H_2 + \bullet CH_2OH \qquad (1.25)$$

The $\bullet CH_2OH$ radical then serves as a reducing agent for the metal and is oxidized to an aldehyde:

$$M^{n+} + n\bullet CH_2OH \rightarrow M^0 + nCH_2O + nH^+ \qquad (1.26)$$

In instances where the strong reducing power of e_{aq}^- is necessary to perform the reduction, the nitrous oxide atmosphere can be foregone, thereby allowing some degree of control over the strength of the active reducing agent.
The nanoparticle metals produced by radiolytic reduction include Au (2 nm, stabilized in poly(vinyl alcohol) or poly(vinylpyrrolidone))[38], Co (2-4 nm, stabilized by polyacrylate) [39] and Cu (20-100 nm in poly(vinyl sulfate) [40]. 20 nm particles of Ag stabilized with sodium dodecyl sulfate have also been reported, but the resulting colloidal suspensions were not stable against agglomeration [41].
The radiolytic reduction method is perhaps most useful when enlarging colloidal metals or layering dissimilar metals over one another, forming core-shell type arrangements. In these reactions, a metal colloid is usually prepared by a conventional chemical route such as the Turkevich (citrate) method discussed previously. The metal colloids are then essentially used as seed particles for subsequent growth of the same or a different metal from aqueous solutions. For

instance, starting from a solution of 15 nm Au prepared by the citrate method, Henglein et al. enlarged the Au particles sequentially up to diameters of 120 nm by adding aqueous $Au(CN)_2^-$ and methanol to the colloidal solution and irradiating with a ^{60}Co source [42]. The size distribution and monodispersity of the nanoparticles do not appear to be adversely affected throughout the process.

In Henglein's method, rather than the organic radicals directly reducing the metal cations, they instead charge the colloidal Au particles that subsequently act as reducing agents for the aqueous $Au(CN)_2^-$ ions [43]:

$$\bullet CH_2OH + Au_n^{x-} \rightarrow Au_n^{(x+1)-} + CH_2O + H^+ \qquad (1.27)$$

$$Au_n^{(x+1)-} + Au(CN)_2^-(aq) \rightarrow Au_{(n+1)}^{x-} + 2\ CN^- \qquad (1.28)$$

There is, of course, no requirement that the nanoparticle seeds and aqueous metal ions consist of the same metals. A dissimilar metal cation dissolved in the aqueous solution would essentially coat the surfaces of the existing metal colloid particles, creating a core-shell type composite. Henglein et al. have published extensively on this method, and their successes include nanocomposites of $Au_{core}Pt_{shell}$ [44], $Pt_{core}Au_{shell}$ [44], $Au_{core}Hg_{shell}$ [45], $Au_{core}Pb_{shell}$ [46] and $Pd_{core}Au_{shell}Ag_{shell}$ [47].

Recently, Lee et al. have reduced aqueous solutions of Ni^{2+} and $NaPH_2O_2,H_2O$ to 100-300 nm Ni-P nanocomposites with synchrotron X-rays [48]. The particle sizes could be controlled by adjusting the temperature of the solution, although considerable aggregation of the products was observed. Nonetheless, this appears to be the first report of nanoparticles prepared by irradiation with synchrotron X-rays.

Yeh et al. have reported the synthesis of Au-Ag, Au-Pd, Ag-Pd, and Au-Ag-Pd nanoparticles by irradiating the appropriate mixtures of metal colloids with an Nd:YAG laser [49-51]. Although this method cannot be classified as a precipitation reaction, since the metals were already in colloidal form prior to irradiation, it is nonetheless noted here as a potentially very useful method of preparing bi- and

trimetallic nanoparticles.

Precipitation of Oxides from Aqueous Solutions

The precipitation of oxides, from both aqueous and nonaqueous solutions, is somewhat less straightforward than the precipitation of metals. Reactions for the synthesis of oxides can generally be broken into two categories: those that produce an oxide directly and those that produce what is best termed a precursor that must be subjected to further processing (drying, calcination, etc.). In either case, monodispersed nanoparticles of oxides, like those of metals, frequently require a capping ligand or other surfacebound stabilizer to prevent agglomeration of the particles.

In those cases where calcination or annealing of the samples is necessary, some agglomeration will be unavoidable. Nanoparticles can nonetheless be so obtained, but there is little chance of the particles being monodispersed. For many of the reported syntheses of oxides, monodispersity of the products was neither a requirement nor a priority for the researchers involved.

The products of coprecipitation reactions, particularly those performed at or near room temperature, are usually amorphous. In those cases where hydroxides or carbonates of mixed metals are precipitated from solution and subjected to a calcination or postannealing process, it is extremely difficult to experimentally determine whether the as-prepared precursor is a single-phase solid solution or a multiphase nearly-homogeneous mixture of the constituent metal hydroxides-carbonates-oxides that react to form a single-phase mixed-metal oxide when heated.

Many nanoparticulate metal oxides are prepared by calcining hydroxide coprecipitation products. Albuquerque et al. prepared spinel-structured $Ni_{0.5}Zn_{0.5}Fe_2O_4$ by precipitating a mixture of Fe, Ni, and Zn nitrates with NaOH and calcining at 300 °C or higher [52]. Particle sizes ranged from 9 to 90 nm, depending on the calcination temperature. $MgFe_2O_4$ [53] and $Sm_{1-x}Sr_xFeO_{3-\delta}$ [54] have been prepared by nearly identical methods.

The coprecipitation of metal cations as carbonates, bicarbonates, or oxalates, followed by their subsequent

calcination and decomposition, is a common method for producing crystalline nanoparticulate oxides. The calcination will, however, almost invariably lead to agglomeration or, at high temperatures, aggregation and sintering. Fortunately, nanoparticulate hydroxide, carbonate, and oxalate precursors tend to decompose at relatively low temperatures (<400 °C) due to their high surface areas, thereby minimizing agglomeration and aggregation [55].

Du et al. were able to prepare the $Bi_4Ti_3O_{12}$ ferroelectric by calcining the product from the reaction between a basic solution of TiO_2 and $Bi(NO_3)_3$ performed in acidic solution [56]. Agglomerate sizes ranged from 16 to 48 nm after calcining between 500 and 800 °C. When the calcination temperature was kept at 500 °C or below, $Bi_4Ti_3O_{12}$ appeared to crystallize in a metastable tetragonal phase previously thought to be stable only at high temperatures.

In some rare instances, crystalline oxides can be precipitated from aqueous solution, eliminating the need for a calcination step and greatly reducing the risk of agglomeration. This approach is most common for simple binary oxides. 50-60 nm aggregates of 4 nm rutile-structured TiO_2, for instance, can be prepared by precipitating aqueous $TiCl_3$ with NH_4OH under ambient conditions and stabilizing the products with poly(methyl methacrylate) [57].

The direct coprecipitation of more complex ternary oxides, while somewhat uncommon, is nonetheless possible, particularly when the product assumes a very thermodynamically favorable structure such as spinel. In such cases, the precipitation reactions are normally carried out at elevated temperatures (50-100 °C), such that the hydroxide intermediates are condensed into oxides in the same reaction vessel as where coprecipitation was induced. Such “one-pot” synthesis techniques render calcination steps unnecessary. Fe_3O_4, for example, has been prepared as an oxide by the simple coprecipitation of (Fe^{2+} + 2 Fe^{3+}) with NaOH at temperatures above 70 °C [58]. 5-25 nm particles of $MnFe_2O_4$ were similarly prepared from aqueous Mn^{2+} and Fe^{2+} solutions at temperatures up to 100 °C [59].

Chinnasamy et al. reported an extensive series of experiments for the spinel-structured $CoFe_2O_4$ designed to determine the

influence of reaction temperature, reactant concentration, and reactant addition rate on the size of the products [60]. In each case, aqueous solutions of Fe^{3+} and Co^{2+} were precipitated with dilute NaOH. The results showed that increasing the temperature from 70 to 98 °C increased the average particle size from 14 to 18 nm. Increasing the NaOH concentration from 0.73 to 1.13 M increased particle size from 16 to 19 nm. NaOH concentrations of 1.5 M or greater resulted in the formation of a secondary FeOOH phase, and slowing the NaOH addition rate appeared to broaden the particle size distribution.

Li et al. prepared 12 nm $CoFe_2O_4$ by a similar route but stabilized the product by acidification with dilute nitric acid [61]. The electrostatic repulsion of the particles created by the adsorption of H^+ at the particle surfaces resulted in an indefinitely stable colloid of ferromagnetic particles (a *ferrofluid*). By contrast, Fe_3O_4 ferrofluids, which tend to not be stable under acidic solutions, have been sterically stabilized by coating Fe_3O_4 nanoparticles with oleic acid, poly(vinyl alcohol), or starch [62, 63].

1.2.2. Templated Syntheses

The synthesis of nanoparticles on templates has garnered an increasing amount of attention in the past few years. As will be discussed here, this approach encompasses a broad array of synthetic strategies and frequently involves methods that are best described as hybrids between previously discussed techniques.

The technique of heterogeneous nucleation, in which “seed” crystals serve as nucleation sites for further deposition and growth of crystallites, can essentially be considered one of the simpler forms of a templated synthesis. This technique can be used to increase the average particle size of nanoparticles, such as when aqueous Au^{3+} is deposited on colloidal Au, or Ag^+ is deposited on colloidal Ag [64, 65]. The method can also be used for the synthesis of core-shell and onion structures [66-75].

To maintain the narrow size distribution of the nanoparticles,

care must be taken to ensure that smaller particles do not nucleate from solution during the deposition process. Several new techniques have recently emerged to prevent this occurrence. Brown et al. used hydroxylamine (NH_2OH) for the seed-mediated growth of colloidal Au, increasing the average diameter from 12 nm up to 50 nm [76]. The use of hydroxylamine is critical to this process. While hydroxylamine can theoretically reduce $AuCl_4^-$ to Au^0, the reduction kinetics of this process are greatly enhanced in the presence of the colloidal Au seed particles, in which the Au surfaces serve as catalysts. The reduction of $AuCl_4^-$ therefore preferentially occurs at the Au surfaces, as opposed to leading to the nucleation of new, smaller Au particles from solution. This process can therefore be described as *electroless plating* [77]. Taking the process one step further, Schmid et al. deposited ~9 nm thick Pd shells on 18 nm colloidal Au particles from solutions of H_2PdCl_4 using hydroxylamine hydrochloride ($NH_2OH{\cdot}HCl$) as the reducing agent and *p*-$H_2NC_6H_5SO_3^-Na^+$ as a stabilizer [66].

In recent years, a great deal of interest has developed in the synthesis of metal and metal oxide nanoparticles on polymer templates. Initially, these reactions consisted simply of the reduction of transition metals, the decomposition of metal carbonyls, or precipitation of metal oxides in polymer matrixes. Platonova et al. prepared 1 nm Co in a polystyrene (PS)-PVP copolymer this way [78]. The syntheses of nanoparticulate $CoFe_2O_4$ [79] and Fe_3O_4 [80] have recently been achieved by similar methods. In recent years, various researchers have developed increasingly complex variations of these syntheses. Bronstein et al. prepared 1-2 nm Au, Pd, and Pt using poly(octadecylsiloxane), which formed a bilayer structure of opposing Si-O-Si chains with water intercalated between the layers [81]. Metal cations were inserted into the aqueous layers prior to reduction with borohydride ion. Liang et al. have reported a process by which Au was deposited on spherical particles of polystyrene (PS) by first coating the PS with a positively charged polymer like poly(allylamine hydrochloride) and combining it with colloidal Au stabilized with 4-(dimethylamino)pyridine (DMAP) [82]. The capping ligands of the colloidal Au particles were consequently

attached electrostatically to the coated PS particles. The gold particles could then be enlarged by the hydroxylamine method described previously. The polymers were subsequently removed either by calcination of the products at 310 °C under oxygen or by washing with THF, resulting in the formation of 500 nm diameter hollow gold spheres.

In an inverse approach to the above process, Marinakos et al. used colloidal Au particles as templates for the formation of hollow polymer spheres [83]. They deposited the colloidal Au (prepared by the citrate method) into the spheres of a porous alumina membrane and applied one or more layers of a polymer, such as polypyrrole, to the Au by diffusing pyrrole vapor through the membrane in the presence of a polymerization initiator. Au was subsequently dissolved by washing with a cyanide solution, and the alumina membrane could be removed by treatment with dilute KOH. The polymer coating could be varied from 5 to 100 nm thick, depending on the time allowed for vapor deposition. The sizes of the cores were controlled by varying the diameters of Au particles in the colloids from 5 to 200 nm. Nair et al. have similarly prepared hollow ZrO_2 nanoparticles by leaching Ag from $Ag@ZrO_2$ particles with CCl_4 [84].

Crooks et al. have encapsulated Pd and Pt nanoparticles as small as 1 nm with dendrimers such as poly(amidoamine) by absorbing the respective metal cations into the dendrimer structure prior to chemical reduction [85]. The authors have extended this process to the encapsulation of Cu, Ni, Fe, Au, and Ru and have recently reviewed this work in detail [86].

Kim et al. prepared Au nanoparticles in mesoporous carbon by first encapsulating colloidal Au with SiO_2 shells formed by the hydrolysis of aminopropyltrimethoxysilane in the presence of sodium silicate [87]. The $Au@SiO_2$ particles were subsequently encapsulated in mesoporous silica by initiating a second hydrolysis reaction of TEOS and octadecyltrimethoxysilane. After calcination, the particles containing $Au@SiO_2$ cores and porous silica shells were saturated with phenol and a polymerization initiator and heated under vacuum, resulting in the formation of an amorphous carbon-silica composite. The silica could be subsequently removed by etching with an HF solution. The

final product consisted of 13 nm Au cores surrounded by 15-25 nm thick carbon shells with hollow cores. Because the interiors of the carbon shells are larger than the 13 nm Au particles, the resulting product is referred to as a *nanorattle*. The subject of carbon-encapsulated metal nanoparticles, including their various methods of syntheses, has been reviewed [88].
Morley et al. deposited 10-100 nm Ag particles within the pores of poly(styrene-divinylbenzene) beads and silica aerogels by solvothermal treatment in supercritical CO_2 [89]. The silver precursor, in the form of Ag(hfpd)(tetraamine) or Ag(hfpd)(tetraglyme) (hfpd = 1,1,1,5,5,5-hexafluoropentane-2,4-dione), was combined with the host material and CO_2 in an autoclave and heated to 40 °C (270 atm). Subsequent decomposition of the complexes to Ag metal was performed in a second step, in which the autoclave was filled with H_2 and heated to 60 °C (67 atm).

1.2.3. Surface-Derivatized Nanoparticles

As already outlined, the most common methods of synthesizing nanocrystalline inorganic substances are based on reactions performed in solutions. Solution techniques allow maintainance of the desired composition of the reaction mixtures while eliminating the diffusion restrictions; such methods therefore permit accurate control of the stoichiometry. Solution techniques also allow management of the reaction kinetics and the course of crystallization of the insoluble target product. Solution reactions facilitate tuning the equilibrium between the reagents, products, and solvent and, therefore, provide the opportunity for controlling the interaction of growing crystals with the environment. One of the familiar examples of a system where these interactions are tuned to the desired extent is the synthesis of aqueous colloids (sols) of metals, metal oxides, sulfides, and so forth. Stability of these colloids is optimized as the interaction of the nanocrystals with the solvent and solvated ions is maintained to overcome the van der Waals interaction between the nanocrystals that otherwise leads to

agglomeration. The mechanism of sol stabilization involves the adsorption of multiple layers of solvent molecules and solvated ions on the nanocrystals' surfaces, forming electric double layers (EDLs). The resulting highly dynamic assemblies possess excessive electrical charges at their peripherals that cause electrostatic repulsion between them [90].

Application of the EDL-stabilization method to the synthesis of colloidal inorganics is limited primarily to aqueous solutions, although it may be used with other polar protic solvents as well. The dynamic nature of EDLs and their sensitivity to their environment impose a significant limitation to the stability of the corresponding colloids, but they also open up exceptional possibilities for further chemical steps toward the modification of the nanoparticles' surfaces, such as depositing a layer of another inorganic substance (inorganic core-inorganic shell composites), attaching certain organic capping ligands (inorganic core-organic shell composites), depositing/assembling the surfactant-free nanoparticles on the preferred substrate, covalent binding to the desired (bio)molecular systems, and so forth.

According to an alternative method, van der Waals interparticle attractions that lead to agglomeration are compensated by surrounding the nanocrystals with bulky organic shells that help keep them apart from each other. This organic interface possessing either hydrophilic or lipophilic properties efficiently stabilizes colloids in aqueous or nonpolar solvent media. There are different types of substances used as components of organic shells, the most common being ionic surfactants, coordinating polymers, and capping ligands. All these compounds possess polar groups that can be attached to the nanoparticle surface and a bulky component within the molecule that provides spatial isolation of the nanocrystal from the environment and provides the solubility properties.

The term "surfactant" is used here for the substances commonly used for preparation of water-oil microemulsions, such as AOT, sodium dodecyl sulfate, CTAB, DDAB, DPB, and TOAB, and for other similar compounds with

amphiphilic properties. The AOT and sodium dodecyl sulfate surfactants have an anionic sulfate ester group with a bulky lipophilic substituent. Stabilization of colloids is achieved when the polar group ("head") of these compounds adsorbs on the surfaces of nanocrystals and the organic nonpolar "tail" faces the peripherals of the resulting assembly, thereby providing steric repulsion. In the case of quarternary ammonium halides (CTAB, DDAB, DPB, TOAB, etc.), halide anions surround the nanoparticle surface while their bulky cationic partners form the external protecting shell. The nanoparticle- surfactant assemblies can be viewed as water-free surfactant micelles bodied with the nanocrystals.

The term "capping ligand" is used for organic molecules that contain a donor group with substituents of varying steric bulk. The main distinction between capping ligands and surfactants lies in the differences of the strength of their binding to metal atoms at the nanocrystal surface, which is greater in the case of capping ligands. These molecules usually closely relate to complexing agents, whose binding to metal atoms or ions has a pronounced covalent character. Generally, colloids containing surfactants have only limited stability, while nanocrystals surrounded by capping ligands are similar to giant metal-cluster complexes that are described as individual substances. To reach the same stability, a smaller mass of capping ligand per unit mass of nanocrystals is required than if surfactant (or polymeric) stabilizer is used. In many cases a monolayer of the molecules of capping ligand around the nanocrystal is sufficient to attain stability against agglomeration with the possibility of isolating and redissolving the solute. The borderline between capping ligands and surfactants, however, is not always clearly defined.

In some methods of synthesizing nanoparticles, the passivating agents are introduced into the reaction solution at the initial step. If capping ligands are used, they interact with metal ions in solution and therefore affect the reaction equilibrium and the rates of crystal nucleation and growth, thus influencing the entire course of the precipitation reaction. Adjustment of the complexing properties of reaction solutions allows tuning not only the nanocrystal size but also

the shapes from spheres to polygons, rods, and wires.
The importance of capping ligands is not only in providing suitable synthesis conditions and the ability to tune the nanocrystals' sizes and shapes: due to differences in electronic and binding properties, capping ligands influence the optoelectronic and magnetic properties of functional nanocrystalline inorganic materials. For this reason, it seems useful to classify capping ligands on the basis of their donor group.
Typical capping ligands can be classified as anionic and neutral. The most common anionic ligands are O- and S-donor type carboxylates, phosphonates, sulfonates, alkoxides, and thiolates. Among common neutral ligands are amines (aliphatic and aromatic), phosphines, phosphine oxides, alcohols, amides, ethers, and sulfides. The nature of the substituents in capping ligands is variable, depending on the specific application of the nanocomposite. Hydrocarbon chains are used for oil-soluble particles, but polar functional groups are preferred when an application requires solubility in water or other polar solvents and a certain reactivity is required for obtaining more complex molecular assemblies.

1.3. Properties of nanocrystals of different shapes

1.3.1. Surface Plasmon Resonant Transitions in Metal Nanoparticles.

Colloidal solutions of spherical gold nanoparticles exhibit a deep red color due to the well-known surface plasmon absorption. The surface plasmon resonance is caused by the coherent motion of the conduction band electrons, which interact with an electromagnetic field [91-95] In a classical picture, polarization of the electrons with respect to the much heavier ionic core of a spherical nanoparticle is induced by the electric field of an incoming light wave. A net charge difference exists only at the nanoparticle surface, which in turn acts as a restoring force. In the simplest case, a dipolar

oscillation of all the electrons with the same phase is created, as shown in Figure 1.1. The observed color originates from the strong absorption of the metal nanoparticles when the frequency of the electromagnetic field becomes resonant with the coherent electron motion.

The frequency and width of the surface plasmon absorption depends on the size and shape of the metal nanoparticles as well as on the dielectric constant of the metal itself and the surrounding medium [91-95]. Noble metals such as copper, silver, and gold have a strong visible-light plasmon resonance, whereas most other transition metals show only a broad and poorly resolved absorption band in the ultraviolet region [91, 92, 96]. This difference is attributed to the strong coupling between the plasmon transition and the interband excitation. In addition, the conduction band electrons of the noble metals can move freely, independently from the ionic background, and the ions act only as scattering centers [97, 98]. This gives the electrons in the noble metals a higher polarizability, which shifts the plasmon resonance to lower frequencies with a sharp bandwidth. The surface plasmon resonance was theoretically explained by Mie in 1908, including linear optical properties such as extinction and scattering of small spherical metal particles [99].

Mie's theory and experimental spectra agree well in the size regime >20 nm until the normal incidence absorption no longer shows a plasmon resonance for bulk metals. The spectrum is composed of the sum of size-dependent absorption and scattering modes. Higher order modes become more dominant with increasing particle size, causing the plasmon absorption band to red shift and resulting in increased bandwidth, because for larger particles, the light cannot polarize the nanoparticles homogeneously and retardation effects lead to the excitation of higher order modes [93]. The optical absorption spectra depend directly on the size of the nanoparticles, which is called the extrinsic size effect [93].

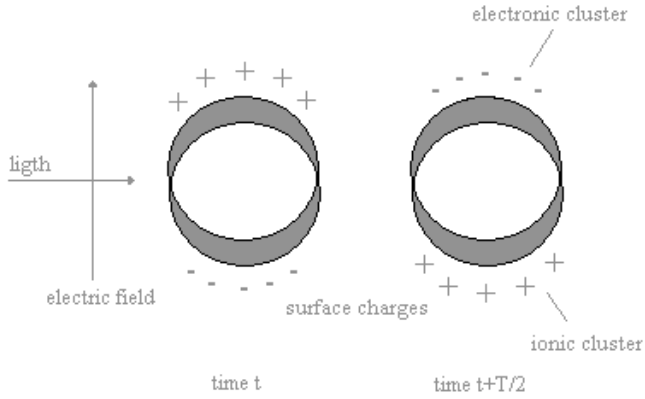

Figure 1.1. Illustration of the excitation of the dipole surface plasmon oscillation. A dipolar oscillation of the electrons is created with period *T*. [91].

When the size of nanoparticles is much smaller than the wavelength (<20 nm) of the interacting light, only the dipole oscillation contributes significantly to the extinction cross section. Mie's theory can be approximately expressed [91-96]

$$\sigma_{ext} = \frac{9V\varepsilon_m^{3/2}}{c} \cdot \frac{\omega\varepsilon_2(\omega)}{\left[\varepsilon_1(\omega) + 2\varepsilon_m\right]^2 + \varepsilon_2(\omega)^2} \qquad (1.29)$$

where V is the particle volume, ω is the angular frequency of the exciting light, and c is the speed of light. ε_m and $\varepsilon(\omega)=\varepsilon_1(\omega)+i\varepsilon_2(\omega)$ are the dielectric functions of the surrounding medium and the metal, respectively. For the metal, the dielectric function is complex and depends on the frequency. The resonance condition is fulfilled roughly when $\varepsilon_1(\omega) = -2\varepsilon_m$ if ε_2 is small or weakly dependent on ω.

Within the dipole approximation (eq. 1.29), the surface plasmon resonance is independent of the particle size. This is contradicted with experimental results on metallic nanoparticles much smaller than 10 nm [93] where the plasmon band shows a size dependence for small particles and even disappears completely for nanoparticles of ≤2 nm [100-102]. Thus, the assumption of a free electron gas is no longer valid in the size range below 2 nm. Very small

nanoparticles are better treated as molecular clusters with discrete electronic states. The question arises about the validity of bulk optical properties stemming from a bulk dielectric function, even for particles within an intermediate size range from 2 to 20 nm with established electronic bands. Thus, the dielectric function is modified for the smaller sized nanoparticles. The dielectric function is decomposed into the interband transitions and a free electron part; the latter can be modified to account for enhanced electron-surface scattering as a function of the particle radius (R) within the Drude free-electron model. Therefore, the dielectric function becomes size dependent [$\varepsilon(\omega,r)$], and this explains the observed $1/r$ dependence of the plasmon bandwidth [93]. The size effects for smaller nanoparticles are called intrinsic size effects because the dielectric function of the material itself is size-dependent [93]. Many other effects such as the spill out of the conduction electrons have also been considered and were incorporated by changing the bulk dielectric function appropriately [103-113].

Mie's theory for spherically shaped particles was extended within the dipole approximation by Gans for cylindrical or oblate nanoparticles [114]. The particles are usually characterized by their aspect ratio (ratio between the length and width of the particle). For elongated ellipsoids, the extinction cross section σ_{ext} is given by [115]:

$$\sigma_{ext} = \frac{\omega}{3c}\varepsilon_m^{3/2} V \sum_j \frac{(1/P_j^{\,2})\varepsilon_2}{\left\{\varepsilon_1 + \left[(1-P_j)/P_j\right]\varepsilon_m\right\}^2 + \varepsilon_2^2} \tag{1.30}$$

where P_j are the depolarization factors along the three axes A, B, and C of the nanorod with $A > B = C$, defined as

$$P_A = \frac{1-e^2}{e^2}\left[\frac{1}{2e} In\left(\frac{1+e}{1-e}\right) - 1\right] \tag{1.31}$$

$$P_B = P_C = \frac{1-P_A}{2} \tag{1.32}$$

and the aspect ratio (r) is included in e as follows:

$$e = \left[1 - \left(\frac{B}{A}\right)^2\right]^{1/2} = \left(1 - \frac{1}{r^2}\right)^{1/2} \quad (1.33)$$

The plasmon resonance for nanorods splits into two bands. As the aspect ratio increases, the energy separation between the resonance frequencies of the two plasmon bands also increases [116-118]. The high energy band corresponds to the oscillation of the electrons perpendicular to the major axis of the rods and is referred to as the transverse plasmon absorption. The other absorption band, which is red-shifted to lower energies, is caused by the oscillation of the electrons along the major axis of the nanorods and is known as the longitudinal surface plasmon absorption. The transverse plasmon absorption has linear dependence on the aspect ratio and the dielectric constant of the medium.

Photoluminescence from bulk copper and gold has been used extensively in characterizing the carrier relaxation and the band structure of metals [119-124]. The emission peak is centered near the interband absorption edge of the metal and attributed to direct radiative recombination of the excited electrons with holes in the d band. In bulk noble metals, the quantum efficiency of the photoluminescence is very low, typically on the order of 10^{-10} [125]. On rough metal surfaces, the luminescence is enhanced by several orders of magnitude, known as the lightning rod effect [120,126,127]. Rough metal surfaces can be treated as a collection of randomly oriented nanometer hemispheroids on the smooth surfaces, which have a surface plasmon resonance similar to the gold nanorods, and therefore the incoming and outgoing electric fields are amplified by the plasmon resonances around the hemispheroids. The luminescence efficiency of gold nanorods increases by 6 orders of magnitude due to this lightning rod effect [128].

Luminescence was also found to be absent in 15 nm spherical nanoparticles, whereas the enhancement of the photoluminescence was found for very small gold clusters (<5 nm) [129]. The origin of the photoluminescence was attributed to the radiative recombination of an electron-hole

pair. The electrons from the filled d band to electronic states were promoted to the sp conduction band above the Fermi level by the incident photons. Both electrons and holes relax by scattering with phonons and recombine radiatively to emit luminescence, which is modified by the local field created around the nanoparticles caused by excitation of the plasmon resonance. The theory of the local field effect has been successfully applied in various cases, including second harmonic generation, surface-enhanced Raman scattering, luminescence from rough noble metal surfaces [120,126,127] and luminescence of gold nanorods, where the observed linear dependence of the luminescence maximum and quadratic dependence of the quantum yield on the aspect ratio can be reproduced [128].
Plasmon resonance spectra with three or more resonance bands are also observed for silver nanocrystals with different shapes, such as silver nanodisks [130-131]. It could be concluded that the number of asymmetric dimensions in the shape of metal nanocrystals can break the plasmon band. The number of plasmon bands increases from one to two, three, or more as the shape changes from sphere to rod, disk, or irregular. This is because the plasmon band breaks or degenerates from one band into two, three, or more bands.

1.3.2. High Surface-to-Volume Ratio

The key factors controlling the properties of nanomaterials are mainly the size and surface characteristics of nanoparticles [98,132-135]. These two factors are interrelated because the S/V ratio increases as the size decreases. For a spherical particle, the S/V ratio is inversely proportional to its radius, R ($S/V = 3/R$).
Full-shell clusters are built up by hexagonal (hcp) or cubic (ccp) close-packed atoms. This assumes that the particles are built on a center atom by adding one, two, or three dense-packed shells. The number of atoms per shell is $N_s = 10n^2 + 2$, where n is the number of the shell [98]. The total number (N) of atoms of the n shell is $N = (10n^3 + 15n^2 + 11n + 3)/3$. Thus, the surface/volume ratio is N_s/N. For example, when

the smallest full-shell cluster consists of 13 atoms, the surface atom ratio is 12/13 = 92.3%. Assuming that the thickness per shell is 6 Å, we can calculate the surface/volume ratio.
It is clear that the surface of nanoparticles plays an important role in their fundamental properties, from structural transformation via light emission to solubility. The surface atoms are chemically more active if compared to the bulk atoms because they usually have fewer adjacent coordinate atoms and unsaturated sites. At the same time, the imperfection of the particle surface induces additional electronic states in the band gap, which act as electron or hole trap centers. At high densities of surface defects, a decrease in the observed transition energy and a red-shifted emission band can be observed due to defect band formation. As the size of the materials decreases, the surface-to-volume ratio increases and the surface effects become more prominent, thereby easier to explore. In addition, the surface states near the gap can mix with the intrinsic states to a substantial extent, and these effects may also influence the spacing of the energy levels of nanoparticles [98,132-135].
In a system containing only a few hundred atoms, a large fraction of these atoms will be located on the surface. Because surface atoms tend to be coordinatively unsaturated, there is a large energy associated with this surface.

1.3.3. Nanocatalysis

The field of nanocatalysis (in which nanoparticles are used to catalyze reactions) has undergone an exponential growth during the past decade. Two types of studies have been carried out: homogeneous catalysis in solution and heterogeneous catalysis in which the nanoparticles are supported on a substrate. Because nanoparticles have a large surface-to-volume ratio compared to bulk materials, they are attractive to use as catalysts. In 1996, it was demonstrated that transition metal nanoparticles can be synthesized with different shapes, and the potential of using different shapes to catalyze different reactions was discussed [136]. Recently, it has been shown that the activities of platinum nanoparticles

of different shapes are indeed different for the same electron-transfer reaction in colloidal solution [137]. This potential shape-dependent catalysis adds to the advantage of using nanoparticles as catalysts. Of course, being small with corners and edges could make their surface atoms unstable during the chemical reaction they catalyze, and shape changes could occur [138].

Homogeneous Catalysis

In homogeneous catalysis, transition metal nanoparticles in colloidal solution are used as catalysts. In this type of catalysis, the colloidal metal nanoparticles are dispersed in an organic or aqueous solution or in a solvent mixture. The colloidal nanoparticles must be stabilized to prevent their aggregation and also to be good potential recyclable catalysts. However, it was shown that the better the capping, which makes the nanoparticles stable in solution, the lower the catalytic activity becomes because the active surface sites are better protected [139].
Being small has the advantage that a larger fraction of the atoms is used in the catalysis process. Furthermore, surface atoms can occupy the corners and edges of the nanoparticles and thus become chemically unsaturated and also much more active. Recently, Narayanan and El-Sayed [137] showed that there is a reasonable correlation between the catalytic activity of nanoparticles with different shapes and the fraction of atoms located on corners or edges. However, this high reactivity could lead to surface reconstruction and shape changes in colloidal solution [138]. Thus, being small could make the surface atoms dynamically active and could also lead to surface reconstruction. In the electron-transfer reaction catalyzed with tetrahedral shaped Pt nanoparticles in colloidal solution, it is found that the activity of the nanoparticles decreases during the course of the reaction as a result of changes toward a spherical shape (which is the most stable having the lowest surface/volume value) [140].
There have been a number of reviews that discuss the use of colloidal transition metal nanoparticles as catalysts for

homogeneous catalysis and also some of the major reactions that this type of nanoparticles can catalyze. One review has focused on whether transition metal colloidal nanoparticles are potential recyclable catalysts [141]. The synthesis, structure, and catalytic properties of ligand-stabilized giant palladium clusters and nanosized palladium complexes have also been reported [142]. The use of transition metal nanoparticles stabilized with various polymers as homogeneous catalysts has been reviewed [143]. The use of monometallic and bimetallic nanoparticles stabilized by solvent and surfactants as catalysts has been surveyed [144]. The application of colloidal transition metal catalysts as low-temperature oxidation catalysts has been reviewed [145]. Finally, a general review on nanoscale transition metal nanoparticles and a description of transition metal colloids has been published [146].

Heterogeneous Catalysis on Support

In heterogeneous catalysis, transition metal nanoparticles are supported on various substrates and used as catalysts. There have been a number of reviews that discuss various reactions conducted using supported transition metal nanoparticles as catalysts [147-156]. In particular, have been reported highly active supported transition metal nanocatalysts for hydrogenations and enantioselective synthesis of organic compounds [147]; functional resins as potential supports for transition metal nanoparticles as complements to traditional supports [148]; the effect of the support used on the catalytic activity of monometallic and bimetallic nanoparticles [149]; the catalytic properties of transition metal nanoparticles that are supported on oxide supports [150]; supported transition metal nanoparticles as catalysts for oxidations and epoxidations [151]; the impact of nanoscience on heterogeneous catalysis [152]; the use of supported bimetallic nanoparticles for catalyzing a variety of hydrogenation reactions [153]. A review has been conducted suggesting that the focus of transition metal nanoparticles as catalysts in heterogeneous catalysis should be on 100% selectivity of the

product to be formed [154]. Adsorbate-induced restructuring of supported transition metal nanocatalysts has been surveyed [155]. A survey of supported transition nanoparticles fabricated by using electron beam lithography and pulsed laser deposition has been conducted [156]. There are three major ways through which heterogeneous transition metal nanocatalysts are prepared: adsorption of the nanoparticles onto supports, grafting of the nanoparticles onto supports, and fabrication of nanostructures onto supports by lithographic techniques. Some common matrixes that have been used in the preparation of supported transition metal nanoparticles include carbon [157, 158], silica [159, 160], alumina [161, 162], titanium dioxide [163], grafting onto polymeric supports [164-166] and lithographic fabrication [167-169] on supports.

1.4. Experimental Techniques

1.4.1. High Resolution TEM (HR-TEM) [170]

The transmission electron microscope (TEM) has become a premier tool for the microstructural characterization of materials. The diffraction patterns measured by X-Ray methods are more quantitative than electron diffraction patterns, but the important advantage of electrons are that they can be focused easily. Electron microscopes can be used to make images of the electron intensity emerging from the sample. For example, variations in the intensity of electron diffraction across a thin specimen, called 'diffraction contrast', is useful for making images of defects such as dislocations, interfaces, and second phase particles. Very often HR-TEM works close to the resolution limit. To understand the image formation it is necessary to study the interactions of the electron beam with the crystal, the role of the lens aberrations and the wave transfer by the microscope.

In a transmission electron microscope, electrons having energy of several keV irradiate a sample in the form of a thin foil. For the interaction of the electrons with the crystal, there are three possibilities:

i) they pass the crystal undeviated;
ii) they are scattered (elastically or inelastically);
iii) they are reflected.

In the process of elastic scattering, the electrons interact with the electrostatic potential of the nuclei of atoms. This potential deviates the trajectory of incident electrons with a very low energy loss; only the direction is changed. There is in fact a small loss of energy by the change of the momentum. However, because of the change of the scattered electron and atom mass ($\Delta E/E^0 \sim 10^{-9}$ at aperture angles used in TEM) the loss is too small to affect the coherency of the beam.

In the inelastic scattering process, energy of the incident electron may be transferred to internal degrees of freedom in the atom or specimen in several ways. This transfer may

cause excitation or ionization of the bound electrons, excitations of free electrons or lattice vibrations and possibly heating or radiation damage of the specimen. The most common are interactions with the electrons in the crystal. Here the energy loss ΔE is important, because the interacting electrons are of the same mass m. However, the fraction of energy is small when compared to the incident energy E. This kind of interaction as well as different secondary processes like X-ray emission, Auger electrons emission, cathodoluminiscence etc. (Figure 1.2) allow to link the structural aspect of the sample with the information about its chemical nature, if the microscope is equipped with appropriate detectors.

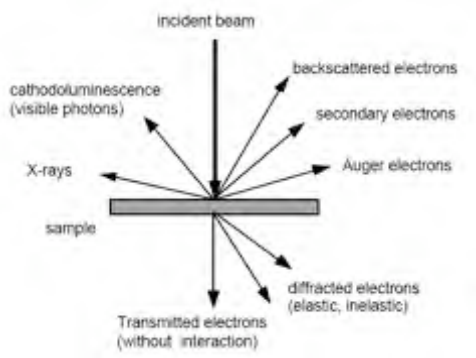

Figure 1.2. Interactions of an electron beam with a thin foil

2.1.1. Image forming by a lens without aberrations

Image formation in a High Resolution Electron Microscope is an interference phenomenon. The thin crystal placed in the object plane of the objective lens (Figure 1.3) diffracts a parallel, coherent incident electron beam. The lens forms in its image plane a magnified and inverted image $\psi(\vec{r}')$ of the wavefunction $\psi(\vec{r})$ at the exit face of the crystal. In the back focal plane the electron beams converge and form Fraunhofer diffraction pattern, representing a Fourier transform $\tilde{\psi}(\vec{q})$ of the wave $\psi(\vec{r})$.

The pass from the focal plane to the image plane may be described as an inverse Fourier transform. Thus, for the overall relation between the object and the image eq. 1.34 is obtained:

$$\psi(\vec{r}') = F^{-1}\left\{\tilde{\psi}(\vec{q})\right\} = F^{-1}\left\{F\left\{\psi(\vec{r})\right\}\right\} \qquad (1.34)$$

As the illumination of the object is coherent, image A' of each of the points *A* results from an interference of several (spherical) waves admitted by the opening of the contrast aperture.

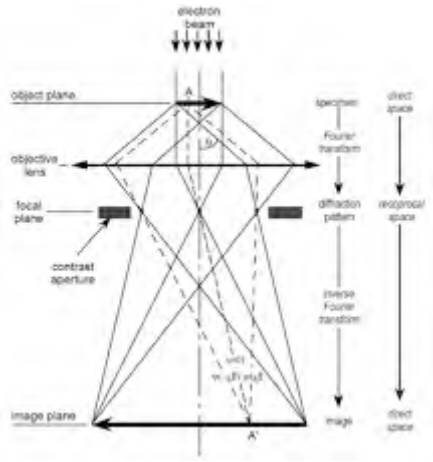

Figure 1.2. Image forming by a lens without aberrations.

2.1.2. Interpretation of the interference image

Interpretation of HRTEM interference images with the atomic resolution consists in the exact determination of the positions of atomic columns with respect to the black and white contrast on the micrograph. A direct interpretation is possible only in very special cases of 'weak phase objects', where the final image corresponds to the projected potential of the whole specimen. Real crystals are 'strong phase objects'. There is no linearity of their interaction with the incident electron beam, nor the transfer of the intensity of the image. Consequently, it is not possible to assign an intuitive manner

to an experimental image of a crystal structure that diffracted the incident beam.
The main problem is that the positions of the maxima and minima of interference with respect to the atomic columns depend at the same time on the crystal thickness and on the defocus of the objective lens. Apart from this, it is also difficult to determine the values of both these experimental parameters.
Figure 1.4 shows the distribution of minima and maxima of interference with respect to the position of the atomic columns for a wave emerging from a perfect crystal. Independently on the transfer of the contrast by microscope, the maxima are placed at the position of atomic columns (z_1) or at 'tunnels' between them (z_3). Although at certain thicknesses (z_2) the emerging wave has an intermediate form between (z_1) and (z_3) and another series of 'supplementary' maxima appears. These three forms of waves repeat periodically with the crystal thickness.

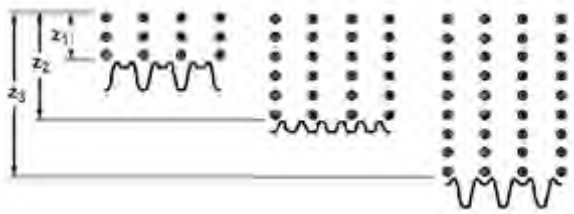

Figure 1.4. Distribution of maxima and minima of interference at the exit of the crystal.

Now an electron wave emerging from the crystal is considered. This wavefunction has its maxima at the position of the atomic columns (Figure 1.5). As shown in the previous section, the objective lens creates in its image plane an inverted and magnified image of this wavefunction. The particularity of the coherent interference imaging is that a series of Fourier images spread around the image plane of the objective lens is obtained. The difference to incoherent interference is that it would just give one sharp image, under the conditions of exact focus (Gauss focus). Fourier images repeat with a period Δz, which depends on the lateral

periodicity of the sample, represented by the planar d_{hkl} and on the wavelength of the electrons:

$$\Delta z = \frac{2d_{hkl}^2}{\lambda} \tag{1.35}$$

As an example, the period for the imaging of {111} crystal planes of aluminium with 200 keV electrons is Δz = 43 nm.
From Figure 1.5 it is obvious that, depending on the focus of the objective lens the so-called 'structure images', on which the atoms appear as 'white' or 'black' are obtained. There is also a third possibility: the maxima of intensity at the positions of atoms and at the position of 'tunnels' between them are nearly the same. In this case, the interference image does not correspond at all to the geometry of the crystal. Thus, a model of the corresponding crystal has to be created, followed by simulation of the interaction of the crystal with the electrons in order to obtain the wavefunction emerging from the crystal. At the end the results from the calculation has to be compared with the experimental results.

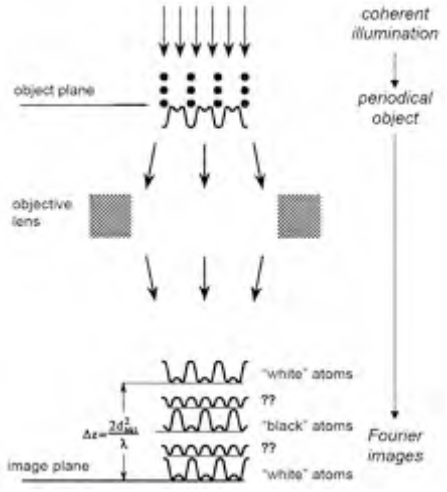

Figure 1.5. Fourier images.

1.4.2. Small Angle Scattering techniques [171]

Small Angle Scattering (SAS) is the collective name given to the techniques of Small Angle Neutron (SANS), X-ray (SAXS) and Light (SALS, or LS) Scattering. In each of these techniques, radiation is elastically scattered by a sample and the resulting small angle scattering pattern is analysed to provide information about size, shape, interaction and orientation of some component of the sample. The type of sample that can be studied by SAS, the sample environment that can be applied, the actual length scale that can be probed and the information that can be obtained, all depend on the nature of the probe (photons or particles) applied. For example, LS cannot be used to study optically opaque samples and SAXS cannot be employed easily to study thick samples. Furthermore SANS and SAXS probe different length scales to LS. Even if these techniques are complementary, they share various similarities. One of the most important of these is the fact that with minor adjustments to account for the different types of probe, the same basic equations and scattering 'laws', like the Guinier, Zimm, Kratky and Porod law can be used to analyse data from any of these three techniques. As the basic equations and 'laws' for SANS, SAXS and LS are more or less the same, this section will refer mainly to neutron scattering techniques.

Properties of Neutron radiation

Neutron radiation can be used to cover a range of wavelengths: 0.01 – 3 nm would not be atypically. This range is comparable to that which can be obtained with the Cu-K_α line at 0.1542 nm for X-ray scattering, but is orders of magnitude smaller than that of visible light (400–700 nm). The usefulness of SAS to colloid and polymer science becomes clear when one considers the different length scales involved. For example, bond lengths are typically around 0.1 nm, the radius of gyration of a polymer in solution is usually 1–10 nm, a surfactant micelle may be 1–100 nm in diameter,

whereas latex particles and emulsion droplets are often 100–1000 nm in diameter.

In the case of electromagnetic radiation, energy, E, and wavelength, λ, are related through the well-known Planck's equation:

$$E = \frac{hc}{\lambda} \tag{1.36}$$

where h = $6.626 \cdot 10^{-34}$ Js is the Planck's constant and c=$2.997 \cdot 10^{8}$ ms^{-1} is the velocity of light in vacuum. But because the neutron has a finite mass (m = $1.674 \cdot 10^{-27}$ kg) it is necessary to consider its kinetic energy instead, given by eq. 1.37:

$$E = \frac{h^2}{2m\lambda^2} = \frac{mv^2}{2} \tag{1.37}$$

where E is the kinetic energy in Joule, λ is the wavelength of the neutron in metres, v is the neutron velocity in $m \cdot s^{-1}$. Because of that, a neutron with a wavelength of 0.15 nm has an energy of $5.83 \cdot 10^{-21}$ J or 36.4 meV. In comparison, the energy of a 0,15 nm X-ray photon is ~8.2 keV, more than 200,000 times greater than the energy of a neutron. Apart from the effects that radiative heating may have, depositing this much energy in a sample can easily bring about serious molecular degradation. The C-C bond energy is only ~4 eV. Neutrons therefore have a particular advantage over X-rays in the study of sensitive samples, such as biological materials. Substituting the kinetic energy of the neutron into eq. 1.36 and solving for λ yields an equivalent wavenumber for the 0.15 nm neutron of ~293 cm^{-1}. This value is comparable to those of typical IR/Raman vibrational modes and demonstrates that neutrons can also be used to study dynamic properties of a sample.

The most important difference between neutron and electromagnetic radiation is the mechanism by which the incident radiation interacts with matter. Light and X-rays are both scattered by the electrons surrounding the nuclei, while

neutrons are scattered by the nucleus itself. This fact has several important consequences.
In the case of light or X-rays, the scattering cross-section of an atom increases proportionally to the number of electrons present. This concept can be linked to the collision cross-section encountered in the classical derivation of chemical kinetic energy. Thus, it increases with increasing the atomic number, *Z*. However, the strength of the neutron-nucleus interaction varies randomly with *Z*. There is also variation in the neutron scattering cross-section, σ of isotopes of the same element. The most significant isotopic variation occurs when Z=*1*. Hydrogen has a (coherent) σ_{coh} of $1.75 \cdot 10^{-24}$ cm^2 (in physicists units *1.75 barns*) which is roughly that of manganese. On the other hand, for deuterium σ_{coh} = *5.6 barns*, which is similar to that of ^{12}C. Thus, it is possible to differentiate between hydrogen isotopes. Only coherently scattered neutrons, where the phase is conserved, carry any structural information about the sample. All nuclei with non-zero spin also scatter neutrons incoherently, because different isotopes may be present in different amounts and/or have different nuclear spin states). In SANS incoherent scattering manifests itself as an isotropic background signal, which can be a problem if the coherent scattering is small (e.g. hydrogen has a much greater incoherent neutron cross-section, σ_{inc}, than most other common nuclei so that hydrogenated samples have always an higher background). Thus for measurements in aqueous solutions deuterated water is usually used as solvent. Table 1.1 [172] gives a selection of neutron scattering cross-sections and neutron scattering lengths, *b*. Where no atomic number is given, natural isotopic abundance is assumed. The relation between the scattering cross-section and scattering length is given by eq. 1.38:

$$\sigma = 4\pi b^2 \qquad (1.38)$$

Thus, atomic nuclei being four to six times of magnitude smaller than typical neutron wavelengths, the nuclei act as point scatterers. The result of this is that the nuclear scattering remains constant as the scattering angle increases, allowing

scattering patterns to be collected over the full range from backward to forward angles.

Table 1.1. Selection of neutron scattering cross-sections, σ and neutron scattering lengths, b. fm=10^{-15}m.

Atomic Nucleus	b_{coh} (fm)	σ_{coh} (barns)	σ_{inc} (barns)
^{1}H	-3.741	1.8	80.3
^{2}D	+6.671	5.6	2.1
B	+5.304	3.5	1.7
C	+6.646	5.6	0.0
N	+9.362	11.0	0.5
O	+5.803	4.2	0.0
Na	+3.580	1.6	1.7
Si	+4.153	2.2	0.0
P	+5.131	3.3	0.0
S	+2.847	1.0	0.0
Cl	+9.577	11.5	5.3
Ti	-3.438	1.5	2.9
V	-0.382	0.0	5.1
Cd	+5.130	3.3	2.5
Gd	+6.550	29.4	151.2

The scattering is spherically symmetric. This is, in contrast to the case with X-rays, where atomic diameters are only 0.1–10 times of the typical wavelengths, resulting in a decrease in the scattering with increasing angle.

Interaction between neutrons and matter is weak and the absorption of neutrons by most materials is correspondingly small. Neutron radiation is therefore very penetrating. For example, X-rays with energies of some 10^5 eV would be required to penetrate a sample and its container more than one or two millimetre thick. On the other hand, neutrons can be used to examine bulk properties of a sample with path lengths of several centimetres or surrounded by thick and complex containers.

The neutron has a small magnetic moment. This can interact with the spin and orbital magnetic moments present in a sample containing atoms with unpaired electrons. Thus, some magnetic properties of a sample can be probed.

Another important similarity between electromagnetic and neutron radiation is the fact that, conferring to the De Broglie/Schrödinger wave-particle duality principle, both may be polarised, which gives rise to birefringence. Both may have the plane of polarisation rotated by an optical 'active' material and both demonstrate the concept of refractive indices. Interestingly, the neutron refractive index of a material

$$n = \left(1 - \frac{Nb_{coh}\lambda^2}{2\pi}\right) \tag{1.39}$$

where N is the atomic number density, typically, slightly less than unity, whereas optical refractive indices are greater than unity. This allows neutrons to be totally externally reflected from a surface.

Unfortunately, there are some drawbacks with using neutron radiation. An obvious one is that it is not a technique for the laboratory benchtop. Neutron sources, like synchrotron radiation sources (SRS), are very large, costly facilities that are best constructed and shared between several nations. A second disadvantage compared to X-rays is that neutron sources are relatively weak. The flux of neutrons on SANS instrument at the most powerful neutron sources is typically several orders of magnitude smaller than the flux of X-ray photons on a SRS SAXS beamline. The third drawback is that it is rather difficult to focus neutrons whereas it is comparatively easy to focus light or X-rays.

1.4.2.1. Small Angle Neutron Scattering

In any SAS experiment, a beam of collimated, not necessarily monochromatic, radiation is directed at a sample, illuminating a small volume, $V = A \cdot t_s$, where A is the cross-sectional area of the beam and t_s is the pathlength of the sample. The volume is typically < 0.5 cm^3 for solvated systems. Some of the incident radiation is transmitted by the sample, some is

adsorbed, and some is scattered. A detector of the dimensions $dx \cdot dy$ positioned at the distance, L_{sd}, and scattering angle, θ, from the sample then records the flux of radiation scattered into a solid angle element, $\Delta\Omega = \frac{dxdy}{L^2_{sd}}$. This flux is given by

$$I(\lambda,\theta) = I_0(\lambda) \cdot \Delta\Omega \cdot \eta(\lambda) \cdot T \cdot V \cdot \frac{\partial\sigma}{\partial\Omega}(Q) \qquad (1.40)$$

where I_0 is the incident flux, η is the detector efficiency, T is the sample transmission and $\frac{\partial\sigma}{\partial\Omega}(Q)$ is a function known as the *(microscopic) differential cross-section*. There are existing analogous functions for light and X-rays. The first three terms of eq. 1.40 are instrument specific, whereas the last three terms are sample dependent.

The goal of a SANS experiment is to determine the differential cross-section, since it contains all information on the shape, size and interactions of the scattering bodies in the sample. It is given by

$$\frac{\partial\sigma}{\partial\Omega} = N_P \cdot V_P^2 \cdot (\Delta\delta)^2 \cdot P(Q) \cdot S(Q) + B_{inc} \qquad (1.41)$$

where N_P is the number concentration of scattering bodies, where the subscript P stands for particles, V_P is the volume of the scattering body, $(\Delta\delta)^2$ is the square of the difference in *neutron scattering length density*, which is also called the *contrast*, $P(Q)$ is a function known as the *form or shape factor*, $S(Q)$ is the *interparticle structure factor*, Q is the modulus of the *scattering vector* and B_{inc} is the isotropic incoherent background signal. $\frac{\partial\sigma}{\partial\Omega}(Q)$ has dimensions of $(length)^{-1}$ and is normally expressed in units of cm^{-1}.

In literature the microscopic differential cross section is sometimes replaced by the *macroscopic differential cross-section*, $N_P \cdot \frac{\partial\sigma}{\partial\Omega}(Q)$. In such cases, eq. 1.41 is modified

accordingly. Found is also the expression $f_P = N_P \cdot V_P$ known as the volume fraction of scattering bodies.
Unfortunately, there is not a uniform nomenclature in neutron, light, or X-ray scattering. For example, $\frac{\partial \sigma}{\partial \Omega}(Q)$ or $\frac{\partial \Sigma}{\partial \Omega}(Q)$ is often written as *I(Q)*, whilst the form factor is variously expressed as *P(Q)*, *F(Q)* or even very confusingly *S(Q)*. Still worse are the different expressions for the scattering vector as *Q*, *q*, η, κ and σ.

The Scattering Vector

The quantity referred to as '*the scattering vector*' is the modulus of the resultant between the incident, k_i, and scattered, k_s, wavevectors, see Figure 1.6, and is given by

$$Q = \left|\vec{Q}\right| = \left|\vec{k}_f - \vec{k}_i\right| = \frac{4\pi n}{\lambda}\sin(\theta/2) \qquad (1.42)$$

where *n*, given by eq. 1.39 is the neutron refractive index, which is in neutron scattering ~1. *Q* has dimensions of *(length)*$^{-1}$; normally quoted in nm^{-1} or Å^{-1}.

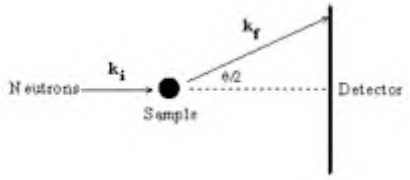

Figure 1.6. Schematic representation of a scattering experiment

By substituting eq. 1.42 into Bragg's Law of Diffraction

$$\lambda = 2d\sin(\theta/2) \qquad (1.43)$$

a very useful expression is obtained:

$$d = \frac{2\pi}{Q} \tag{1.44}$$

where d is a distance. Equations 1.42 and 1.44 are central to SANS experiments because through their combined use it is possible to configure an instrument, i.e. to ensure that its 'Q-range' allows you to see what you expect), and to quickly and rapidly 'size' the scattering bodies in a sample from the position of any diffraction peak in Q-space. For example, the SANS instrument at the ISIS Spallation Neutron Source, called *LOQ*, has a Q-range of ~0.06–10 nm^{-1}, allowing it to probe a range of length scales from ~0.6–100 nm.

The Contrast Term

The neutron scattering length density, δ, of a molecule of I atoms can be calculated from the expression

$$\delta = \sum_i b_i \cdot \frac{D \cdot N_A}{M_W} \tag{1.45}$$

where D is the bulk density of the scattering body and M_w is its molecular weight. With polymers, it is only necessary to calculate δ for one repeat unit. δ has dimensions of $(\text{length})^{-2}$ and can also be negative. The contrast, $\Delta\delta$ is given by

$$(\Delta\delta)^2 = (\delta_P - \delta_m)^2 \tag{1.46}$$

where δ_P is the scattering length density of the sample of interest and δ_m is the scattering length density of the surrounding medium or matrix.
The values of equations 40 and 41 are zero, if $(\Delta\delta)^2$ is zero and there is no scattering. When this condition is met, the scattering bodies are said to be at *contrast match*. Since the SANS from a multi-component sample is essentially a contrast-weight summation of the SANS from each individual component, the technique of contrast matching can be used to dramatically simplify the scattering pattern. For

example, in the study of adsorbed layers it is quite common to contrast match the substrate to the dispersion medium, typically by mixing hydrogenous and deuterated forms of the medium in the appropriate ratio, so that the only scattering observed is that of the absorbed layer. Table 1.2 shows a selection of neutron scattering length densities for the fully hydrogenated and deuterated forms of common solvents and polymers. Table 1.3 shows scattering length densities of common substrates.

Table 1.2. Scattering length densities of different solvents and polymers (PB= polybutadiene, PE= polyethylene, PS= polystyrene, PEO= polyethylene oxide, PMMA=polymethylmethacrylate)

Solvent	δ (h form) (10^{10}cm^{-2})	δ (d form) (10^{10}cm^{-2})	Polymer	δ (h form) (10^{10}cm^{-2})	δ (d form) (10^{10}cm^{-2})
Water	-0.56	+6.38	PB	-0.47	+6.82
Octane	-0.53	+6.43	PE	-0.33	+8.24
Cyclohexane	-0.28	+6.70	PS	+1.42	+6.42
Toluene	+0.94	+5.66	PEO	+0.64	+6.46
Chloroform	+2.39	+3.16	PMMA	+1.10	+7.22

Table 1.3. Scattering length densities of different substrates.

Substrate	δ (10^{10} cm^{-2})	Substrate	δ (10^{10} cm^{-2})
Silicon	+2.07	SiO_2	+3.15
Quartz	+3.47	TiO_2	+2.57

In LS the contrast term arises out of the difference in refractive indices between the different components, whereas in SAXS it arises out of the differences in electron density.

The Form Factor

In the case of very diluted systems the S(Q) contribution can be neglected since it approaches 1 and only P(Q) counts to describe the intensity scattering distribution.

The form factor is a function that describes how $\frac{\partial\sigma}{\partial\Omega}(Q)$ is modulated by interference effects between radiations scattered by different parts of the same scattering body. It is very dependent on the shape of the scattering body. The general form of *P(Q)* is given by Van de Hulst's equation [173]:

$$P(Q) = \frac{1}{V_P^2}\left|\int_0^V \exp\left[if\left(Q\alpha\right)\right]dV_P\right| \qquad (1.47)$$

where α is the 'shape parameter' that represents, for example, a length of gyration. Analytic expressions exist for most common shapes and expressions for more complex topologies, as concentric cylinders [174] or hinged rods [175] can usually be deduced from these. Table 1.4 gives a selection of common form factors.

Table 1.4. Expressions for different form factors

Sphere of radius R_p	$P(Q) = \left[\frac{3\left(Sin\left(QR_p\right) - QR_p\, Cos\left(QR_p\right)\right)}{\left(QR_p\right)^3}\right]^2$
Disc of negligible thickness and radius R_p (J_1 is a first-order Bessel function)	$P(Q) = \frac{2}{\left(QR_p\right)^2}\left[1 - \frac{J_1(2QR_p)}{QR_p}\right]$
Rod of negligible cross-section and length L (S_i is the Sine integral function)	$P(Q) = \frac{2S_i(QL)}{QL} - \frac{Sin^2\left(QL/2\right)}{\left(QL/2\right)}$
Gaussian random coil with z-average radius of gyration R_g, polydispersity (Y+1) and $U = \frac{\left(QR_g\right)^2}{(1+2Y)}$	$P(Q) = \frac{2\left[(1+UY)^{-Y} + U - 1\right]}{(1+Y)\,U^2}$
Concentrated polymer solution with screening length x where $\xi = R_g\left(\frac{\phi}{\phi^*}\right)^{\frac{-3}{4}}$	$P(Q) = P(0)\left[\frac{1}{1+(Q\xi)^2}\right]$

There is an asymptotic behaviour of *P(Q)* which is general and independent of the shape of the particle. This is because at small *Q*-values, i.e. at values smaller than the inverse of the

characteristic dimensions of the particle, the spatial resolution is not sufficient to determine the shape and only information about the size can be obtained. Under these conditions, *P(Q)* is given by the Guinier relation:

$$P(Q)=(\Delta\delta)^2 V_P^2 exp(-Q^2 R_g^2/3) \text{ for } QR_g<1 \qquad (1.48)$$

where R_g is the radius of gyration of the particle and V_P its volume.
At the other extreme, i.e. for values of *Q* much larger than the inverse of the smallest dimensions of the particle, the spatial resolution is too good and just the interface between particle and surface can be probed (see Figure 1.7).

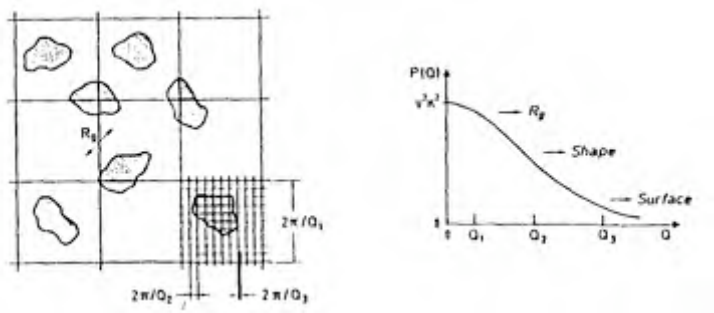

Figure 1.7. Schematic representation of a two-dimensional sample, showing different degrees of resolution and the correspondent regions of the form factor curve.

In the ideal case where the interfacial region is sharp, the equation of Porod is obtained, given by:

$$P(Q)=2\pi(\Delta\delta)^2(S/V_P)Q^{-4} \qquad (1.49)$$

where *S/V* is the total area of the interface per unit of volume of the particle .
At the intermediate range *P(Q)* gives the maximum of information about the size and the shape of the particle.
In a monodisperse system, *P(Q)* shows oscillations related to the characteristic dimensions of the sample even at large *Q* and the derivative of *P(Q)* is not a constant. However, in real

systems, almost every time a certain polydispersity is present (see Figure 1.8).

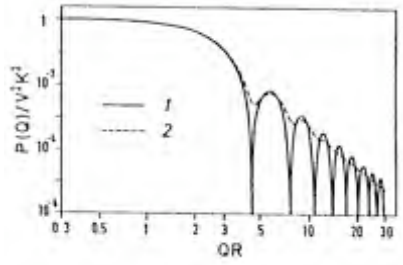

Figure 1.8. Scattered intensity by a diluted of monodispersed spheres of radius R (curve 1) and of a polydispersed and of a polydispersed system with Gaussian distribution of radii, with full width at half maximum equal to 20% of the average radius (curve 2).

The Structure Factor

The structure factor is due, to thermal density or/and concentration fluctuations and to the spatial distribution of the colloidal particles. The first contribution is, most of the time, small compared to the second one. This is because, in most cases, these fluctuations are at a very small scale. In the case of a homogenous fluid, $\frac{\partial\sigma}{\partial\Omega}(Q)$ is given by

$$\frac{\partial\sigma}{\partial\Omega}(Q) = n^2 b^2 k_B T\chi/(1+Q^2\xi^2) \qquad (1.50)$$

where ξ is the correlation length of the sample, k_B is the Boltzman factor, T is the absolute temperature, χ is the osmotic compressibility, b is the scattering length and n is the number density.
The interparticle structure factor, given by

$$S(Q) = 1 + \frac{4\pi N_P}{QV}\int_0^\infty [g(r)-1] r\sin(Qr)dr \qquad (1.51)$$

is a function that describes how $\frac{\partial\sigma}{\partial\Omega}(Q)$ is modulated by interference effects between radiation scattered bodies. It is dependent on the degree of local order in the sample. The result of this is that SAS can be used to gain information on the relative positions of the scattering bodies, usually by the *radial distribution function* given by

$$G(r) = \frac{4\pi N_P r^2}{V} g(r) \qquad (1.52)$$

where *r* is a radial distance from the centre of any scattering body in the sample, and *g(r)* is obtained from eq. 1.47 by Fourier inversion. *G(r)* is typically a damped, oscillating, density distribution function whose maxima correspond to the distance of each nearest-neighbour coordination shell. Moreover, ln*g(r)* is directly related to the potential energy function describing the interactions between the scattering bodies. *g(r)* is related to the probability to find another particle at a distance *r*. Consequently, *g(0)*=0 and remains equal to zero, up to the distance comparable to the particles characteristic size, or at which two particles can interpenetrate. Beyond this distance, *g(r)* passes, by increasing rapidly, through a maximum related to the average next neighbours distance. The function tends to oscillate to unity at infinity (see Figure 1.7)

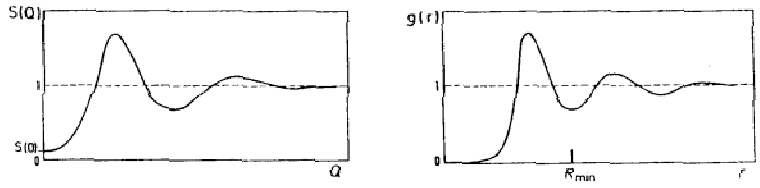

Figure 1.7. Schematic representation of the structure factor S(Q) and of the pair correlation function g(r). The two functions are related by Fourier transformation. S(0) is related to the osmotic compressibility. R_{min} can be used to determine the number of next neighbours of a particle.

Aggregation is another form of arrangements of particles. Aggregates have an irregular shape and there can be just measured their average radius of gyration and polydispersity. In other cases, the connectivity of the particles, forming the aggregate, is loose and eventually self-similar. If this is the case, aggregates can be assimilated to fractal objects. This situation occurs, for example, when particles are much diluted in a solvent and move by Brownian motion. If the repulsive forces reduce to steric interactions, the particles may be kept in contact. A fractal object does not fill the space in a compact way. The number of particles changes inside a sphere of radius r with r^D, with $D \leq 3$. D is called the fractal dimension. The notion of a fractal object applies only within two natural limits: the size, a, of the particle and the size ξ, of the aggregate. As the density of a fractal object changes with r^{D-3}, the scattering factor has approximately the form $S(Q) = AQ^{-D}$, where A is a constant. A straight line in a logarithmic I vs. Q plot represents the power-law, for $\xi^{-1} < Q < a^{-1}$. At low Q values, the characteristic Guinier behaviour gives the radius of gyration of the aggregate. At large values, the scattered intensity is determined by the form factor. An expression can be deduced giving the scattered intensity by a fractal aggregate [176,177]:

$$S(Q) = 1 + \frac{1}{(Q\alpha)^D} \frac{D\Gamma(D-1)}{\left(1 + \frac{1}{Q^2\xi^2}\right)^{(D-1)/2}} \sin[(D-1)tg^{-1}(Q\xi)] \qquad (1.53)$$

Unfortunately, as the concentration of the scattering bodies becomes more and more dilute, with $N_P \rightarrow 0$ and $S(Q) \rightarrow 1$, information about the insight of the microscopic structure can only be obtained in concentrated and/or strongly interacting samples [178].

1.4.2.2 Polarized Small Angle Neutron Scattering (SANSPOL)

It has been shown [179-183] that, using polarized neutrons, the relative contrasts for small-angle scattering of magnetic systems are strongly modified. For polarized neutrons, where the neutron spins are aligned antiparallel (+) or parallel (-) to the magnetic field vector ***H***, which is applied on the studied sample, the scattering cross-sections depend on the polarization P of the incident neutrons $I^+(Q)$ and $I^-(Q)$, respectively [179]. The scattering intensity (denoted as SANSPOL) depends on the polarization state according to

$$I^+(Q,\alpha)=A(Q)+B^+(Q)\sin^2\alpha \qquad (1.54)$$

$$I^-(Q,\alpha)=A(Q)+B^-(Q)\sin^2\alpha \qquad (1.55)$$

where α is the azimuth angle between the vectors ***H*** and ***Q***, while $A(Q)$ is the isotropic and $B(Q)$ is the anisotropic term.
The arithmetic mean of the intensities corresponds to the intensities of a nonpolarized beam (denoted as SANS), given by eq. 1.56:

$$\left[I^+(Q,\alpha)+I^-(Q,\alpha)\right]/2 = I(Q,\alpha)_{non-polarized} \propto \propto \frac{d\sigma}{d\Omega} = A(Q)+B(Q)\sin^2\alpha \qquad (1.56)$$

For complete alignment of the moments along ***H***, and $B(Q)=F_M^2$, where F_N and F_M are the nuclear and magnetic shape factors.
In the case of a system of non-interacting particles, i.e. a dilute system, and if all magnetic moments of the sample are aligned along the external field, the isotropic term contains only the nuclear contribution $A(Q)=F_N^2$. Therefore, both the SANS and the SANSPOL intensity parallel ($\alpha=0$) to ***H*** are independent of the polarization state resulting from pure nuclear contrast and given by

$$I(Q\|H)=A(Q)=F_N^2 \qquad (1.57)$$

In the same dilute system of non-interacting particles with all moments aligned along ***H***, the SANS intensity perpendicular (α = 90°) to the applied field is given by

$$I(Q\perp H)=F_N^2+F_M^2 \qquad (1.58)$$

For more detailed illustration SANS and SANSPOL experiments on a system with weak magnetic contribution will be presented here. Fe_3O_4 particles with super-paramagnetic behaviour embedded in a glass matrix [184] where studied by SANS [185] and SANSPOL [186]. The aspect ratio of the magnetic saturated magnetite is given by:

$$I(Q\perp H)/I(Q\,||\,H)= (F_N^2+F_M^2)/F_N^2 \qquad (1.59)$$

Thus, the magnetic shape factor F_M is small. With a polarized incoming beam, an additional interference term appears in the scattering cross sections [179].

$$I^{\pm} \propto \frac{d\sigma^{\pm}}{d\Omega} = F_N^2 + \left[F_M^2 \mp 2P\left|(1-2f^{\pm})\right|F_N F_M\right]\sin^2\alpha \qquad (1.60)$$

where $f^{\pm}$ is the flipper efficiency with f^{+} = 0 (flipper off and neutrons' magnetic spins down) and $f^{-} = f$ ($f \geq 98\%$; thus ≥ 98% neutrons with spin up), and P is the polarization $P = (N^- - N^+)/(N^- + N^+)$ at the sample position.
The iso-intensity plots of the 2D scattering patterns for I^- and I^+, shown in Figure 1.8, present a pronounced anisotropy with an aspect ratio of 1.32 and 0.76, respectively. The sum signal ($I^- + I^+$) corresponds to the 2D pattern of the experiment with unpolarized neutrons. The difference signal $(I^- - I^+)$ corresponds with the use of eq. 1.60 to the nuclear-magnetic cross term:

$$(I^- - I^+)= 4\,P\,f\,F_N F_M \sin^2\alpha \qquad (1.61)$$

with zero intensity along the direction of ***H***, which is in all the cases horizontal.

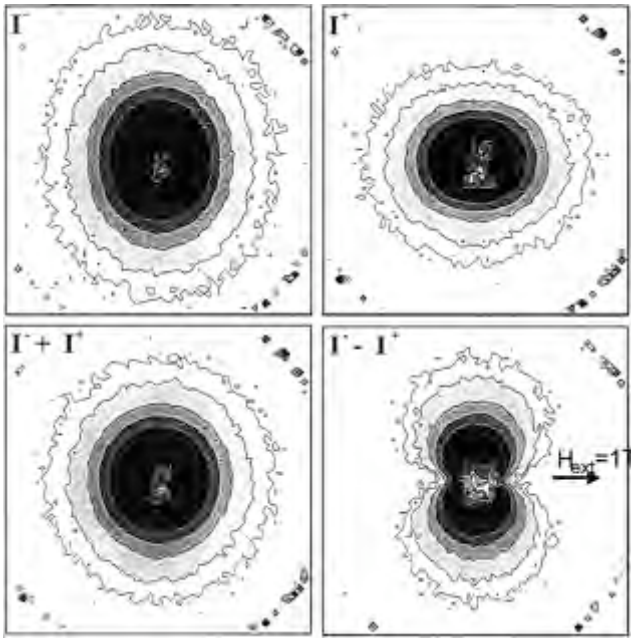

Figure 1.8. SANS iso-intensity scattering patterns from Fe_3O_4 glass ceramic with polarized neutrons for spins antiparallel (I^+, flipper off) and parallel (I^-, flipper on) to the external field H. The sum signal ($I^- + I^+$) corresponds to an unpolarized beam, the difference ($I^- - I^+$) gives an additional interaction term $B_{int}(Q)\sin^2\alpha$.

It becomes clear that according to Figure 1.8 polarized neutron scattering is a very powerful method for dividing weak magnetic contributions from strong nuclear scattering. By adjusting the 2D scattering patterns to the angular dependence given in eq. 1.60, the nuclear part may be determined in two independent ways from the analysis of $I^+(Q)$ and $I^-(Q)$ or from the sum signal ($I^- + I^+$). The cross term $B_{\text{int}}(Q) = 4PfF_NF_M$ is obtained by analyzing the difference signal $(I^- - I^+)$. $A(Q)$ and $B_{int}(Q)$ allow to reconstruct $F_M^2(Q) = B_{\text{int}}^2(Q)/16A(Q)P^2f^2$.

1.4.3. Atomic Force Microscopy

1.4.3.1. Imaging modes [187]

The Atomic Force Microscope is a member of the family of scanning probe microscopes that includes the scanning tunneling microscope and the near field optical microscope (Figure 1.9).

<table>
<tr><th colspan="2">Scanning Probe Microscope Family
Air, Liquid, Vaccum</th></tr>
<tr><td rowspan="2">Atomic Force Microscope (AFM)

Contact Mode
• Lateral Force (LFM)
• Scanning Thermal (SThM)
• Lithography
• Shark

Vibrating Mode
• Close Contact (CC)
• Intermittent Contact (IC)
• Magnetic Force (MFM)
• Electric Force (EFM)
• Kelvin Probe (SKPM)

Electrochemistry</td><td>Scanning Tunnelling Microscope (STM)

Topography
Spectroscopy
Lithography
Echem.
BEEM</td></tr>
<tr><td>Near Field Optical Microscope (NSOM)

Aperture
Aperture-less
Reflection
Transmission</td></tr>
</table>

Figure 1.9. There are several types of Scanning Probe Microscopes that are used for measuring surface topography and physical properties. The primary types of SPM's are the AFM, STM and NSOM. AFM's account for about 80% of the total number of scanning probe microscopes.

Each of these microscopes measures surface topography by raster scanning a small probe across a surface and monitoring the probes motion. A scanning tunneling microscope (STM) operates by monitoring the current flow between a probe and a surface. In the atomic force microscope (AFM) [188], the force between a probe and a surface is monitored. Lastly, in

the near field optical microscope (NSOM) [189] the optical properties of a sample's surface are monitored.
Soon after the invention of the AFM it was realized that these instruments were capable of measuring far more than surface topography. In fact, it is possible to measure almost any physically observable phenomena at the nanometer scale. The only requirement is that a nanoscopic sensor must be developed for the end of a probe. For example, magnetic fields, electric fields, temperature, and hardness may be measured with the AFM probe. Additionally, it is possible to use the AFM probe to modify surfaces. By definition, an AFM mode is a non-topographical measurement made with an AFM.
For the most part, atomic force microscopes are operated in ambient air. At the surface of samples maintained in ambient air, there is always a contamination layer comprised of water and hydrocarbons. Thus, in an AFM, the probe tip is typically immersed in the contamination layer (see Figure 1.10). Because the contamination layer can vary from one environment to the next, the layer can cause uncertainty in AFM measurements.

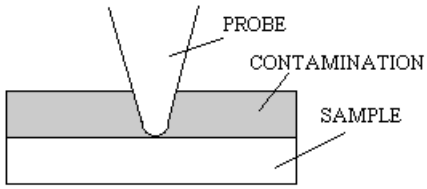

Figure 1.10. In ambient air, the AFM probe must pass through a surface contamination layer to touch the surface.

AFM probes contribute a lot of uncertainty of topography and mode measurements. The uncertainty is due to variations in probe geometry. The typical AFM probe has a diameter of < 15 nm. That is to say it could be 15 or 5 or 10 nm in diameter. The uncertainty goes up when the probe is coated with a thin film of metal or other type of material. Not only are there variations in the probe coating thickness, there can be variations in the integrity of the probe. For example, the

coating on an AFM probe may have grains. Figure 1.11 shows an SEM image of a typical AFM probe and an AFM probe coated with a conductive diamond film.

Figure 1.11 Left: SEM image of standard AFM Probe. Right: SEM image of an AFM probe coated with a conductive diamond film.

Topography Modes

A force sensor in an AFM can only work if the probe interacts with the force field associated with a surface. In ambient air, the potential energy between the probe and surface is shown in Figure 1.12. There are three basic regions of interaction between the probe and surface:

- free space
- attractive region
- repulsive region

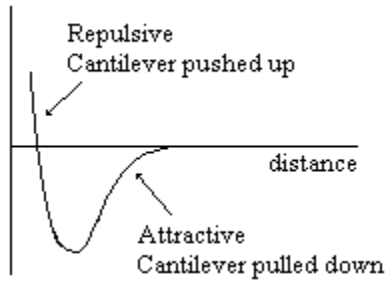

Figure 1.12. Potential energy diagram of a probe and sample. The attractive potential is caused by the capillary forces from surface contamination.

Attractive forces near the surface are caused by a nanoscopic layer of contamination that is present on all surfaces in ambient air. The contamination is typically an aerosol composed of water vapor and hydrocarbons. The amount of contamination depends on the environment in which the microscope is being operated. Repulsive forces increase as the probe begins to "contact" the surface. The repulsive forces in the AFM tend to cause the cantilever to bend up.
There are two primary methods for establishing the forces between a probe and a sample when an AFM is operated. In contact mode the deflection of the cantilever is measured, and in vibrating mode the changes in frequency and amplitude are used to measure the force interaction. As a rule of thumb, the forces between the probe and the surface are greater with contact modes than with vibrating modes.

Contact Modes

In contact mode, the cantilever is scanned over a surface at a fixed deflection (Figure 1.13). Provided that the PID ("Proportional, Integral, Derivative") feedback loop is optimized, a constant force is applied to the surface while scanning. If the PID feedback parameters are not optimized, a variable force is exerted on the surface by a probe during a scan.

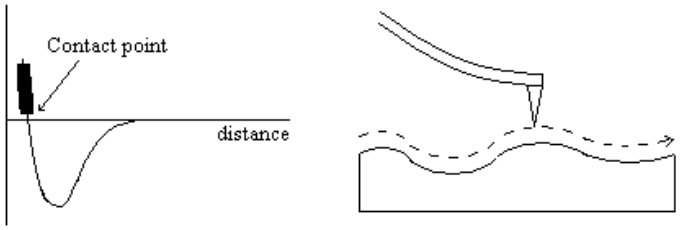

Figure 1.13. Left: Potential diagram showing the region of the probe while scanning in contact mode. Right: In contact mode the probe glides over the surface.

The forces applied to the surface by the probe in contact

mode are given by Hooks law, $F = -k \cdot D$ where F is the force, k is the force constant and D is the deflection distance.

The force constant may be calculated if the dimensions and material of the cantilever are known. Most commercially available cantilevers for the AFM are supplied with the approximate values for the force constant. However, there is typically a very large error in the force constant because of the uncertainties in the thickness of the cantilever. If it is important to know the exact force between the probe and surface, it is recommended to use the Sader [191] method. In this method the length and width of the cantilever are measured with an optical microscope. The so called quality factor, Q, of the cantilever is measured and then the force constant can be calculated.
Contact mode is typically used for scanning hard samples and when a resolution greater than 50 nm is required. The cantilevers used for contact mode may be constructed from silicon or silicon nitride. Resonant frequencies of contact mode cantilevers are typically around 50 kHz and the force constants are below 1 N/m.

Vibrating Modes

In order to make more sensitive measurements requiring better signal/noise ratios in scientific instruments, it is common to modulate the signal being measured and use phase or amplitude detection circuits. Use of modulated techniques shifts the measurement to a higher frequency regime where there is less than *1/f* noise. Such techniques were developed for the AFM soon after it was invented. In order to make the *S/N* ratio higher, and thus be able to measure lower forces with the AFM, the probe is vibrated as it is scanned across a surface. As shown in Figure 1.14, the probe is vibrated in and out of surface potential. The modulated signal can then be processed with a phase or amplitude demodulator.

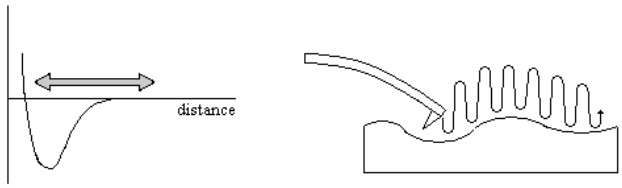

Figure 1.14. Left: Potential diagram showing the motion of the probe in vibrating mode. Right: The probe vibrates as it scans across a surface.

As illustrated in Figure 1.15, the cantilever can be excited with a piezoelectric ceramic. The cantilevers have natural resonant frequency also given by $\omega_0 = c\sqrt{k}$ where c is a proportionality constant and k is the force constant.
At the resonance frequency, there is a 90 degree phase shift. When the probe tip interacts with a surface, the resonance frequency shifts to a lower value, and there is a corresponding change in the phase. When scanning in the vibrating modes, a constant relationship is maintained by the feedback electronics, which keeps either the phase shift or amplitude constant at a given frequency, while scanning.

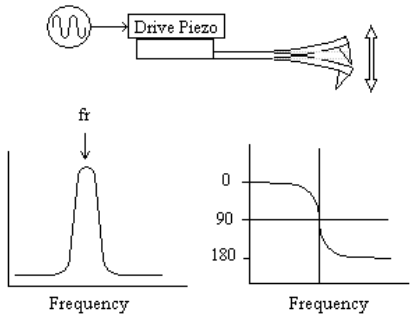

Figure 1.15. Top: a drive piezo causes the cantilever to resonate. Left: at resonance (fr) there is a large increase in the vibration amplitude of the cantilever. Right: at resonance there is a 90° phase shift in the cantilever motion.

As already mentioned, there is a "contamination" layer on surfaces in ambient air with a thickness between 1 and 50 nm.

The probe surface interaction forces are governed by the capillary forces between the probe and the contamination layer. The probe may be vibrated in three separated regimes as it is scanned across the surface (Figure 1.16).
In the first regime, the probe is vibrated across the surface of the contamination layer. The vibration amplitude must be very small and a very stiff probe must be used. The images of the surface contamination layer are typically very "cloudy" and appear to have low resolution. This is because the contamination fills in the nanostructures at the surface.
In the second regime the probe is scanned inside the contamination layer [192]. This technique, named "near contact", requires great care to achieve. The cantilever must be stiff so that the tip does not jump to the surface from the capillary forces caused by the contamination layer. Then very small vibration amplitudes must be used. Often very high resolution images are measured in this regime.
In the third regime the probe is vibrated in and out of the contamination layer. This mode is given several names such as intermittent contact [193] or tapping. In this mode the energy in the vibrating cantilever is much greater than the capillary forces and the probe moves readily in and out of the contamination layer. This mode is the easiest to implement but often results in broken probes because the tip is crashing into the surface upon each oscillation.

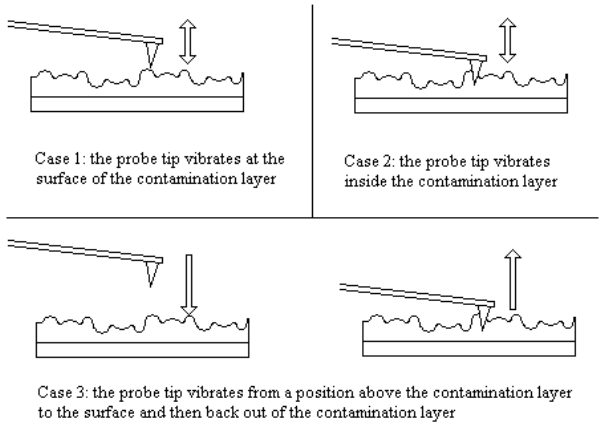

Figure 1.16. Three scenarios for a vibrating probe in relationship to a surface coated with contamination.

One of the unintended benefits of vibrating the probe is that lateral forces that may be acting on the probe during scanning are released. That is, on each oscillation, when the probe is away from the surface, there are no horizontal forces on the probe. This concept was first identified for stylus profilers where it was proposed that vibrating the probe would reduce lateral forces.

Vibrating methods are used when the highest resolution is required or if very soft samples are being scanned. The probes used for vibrating mode are often less than 10 nm in diameter. The integrity of the probe during scanning at these high resolutions can be monitored with a “tip check” sample (Figure 1.17).

Figure 1.17. 2μm×2μm AFM image of a tip checker sample.

1.5. Bibliography

[1] Ring, T. A. *Fundamentals of ceramic powder Processing and Synthesis*; Academic press: San Diego, CA, 1996.

[2] Nielsen, A. E. *Kinetics of Precipitation*; Pergamon Press: Oxford, 1964.

[3] Dirksen, J. A.; Ring, T. A. *Chem. Eng. Sci*. **1991**, *46*, 2389.

[4] Tromp, R.M.; Hanon, J.B. *Surf. Rev. Lett*. **2002**, *9*, 1565.

[5] Karpinski, P.H.; Wey, J.S. In Handbook of Industrial Crystallization, 2nd ed.; Myerson, A.S., Ed.; Butterworth-Heinemann: Stoneham, MA; 2001.

[6] Blackadder, D.A. *Chem. Eng*. **1964**, *CE303*.

[7] Füredi-Milhofer, H. *Pure Appl. Chem*. **1981**, *53*, 2041.

[8] Lifshitz, I.M.; Slyozov, V.V. *J. Phys. Chem. Solids* **1961**, *19*, 35.

[9] Wagner, C.Z. *Elektrochem*. **1961**, *65*, 581.

[10] Sugimoto, T. *Adv. Colloid Interf. Sci*. **1987**, *28*, 65.

[11] Marqusee, J. A.; Ross, J. *J. Chem. Phys.* **1983**, *79*, 373.

[12] Madras, G.; McCoy, B. J. *J. Chem. Phys.* **2002**, *117*, 8042.

[13] Sugimoto, S. *J. Colloid Interface Sci.* **1978**, *63*, 16.

[14] Sugimoto, S. *J. Colloid Interface Sci.* **1978**, *63*, 369.

[15] Tokuyama, M.; Kawasaki, K.; Enomoto, Y. *Physica A* **1986**, *134A*, 323.

[16] Oskam, G.; Hu, Z.; Penn, R. L.; Pesika, N.; Searson, P. C. *Phys. Rev. E* **2002**, *66*, 011403.

[17] Dadyburjor, D. B.; Ruckenstein, E. *J. Cryst. Growth* **1977**, *40*, 279.

[18] Kahlweit, M. Ber. Bunsen-Ges. *Phys. Chem*. **1974**, *78*, 997.

[19] Park, J.; Privman, V.; Matijevic, E. *J. Phys. Chem. B* **2001**, *105*, 11630.

[20] Bramley, A.S.; Hounslow, M.J.; Ryall, R.L. *J. Colloid Interf. Sci.***1996**, *183*,155.

[21] Reetz, M. T.; Helbig, W.; Quaiser, S. A.; Stimming, U.; Breuer, N.; Vogel, R. *Science* **1995**, *267*, 367.

[22] Roucoux, A.; Schulz, J.; Patin, H. *Chem. Rev.* **2002**, *102*, 3757.
[23] Burkin, A. R.; Richardson, F. D. *Powder Metall.* **1967**, *10*, 33.
[24] Schaufelberger, F. A. *J. Metals* **1956**, *8*, 695.
[25] Glavee, G. N.; Klabunde, K. J.; Sorensen, C. M.; Hadjipanayis, G. C. *Langmuir* **1993**, *9*, 162.
[26] Glavee, G. N.; Klabunde, K. J.; Sorensen, C. M.; Hadjipanayis, G. C. *Inorg. Chem.* **1995**, *34*, 28.
[27] Glavee, G. N.; Klabunde, K. J.; Sorensen, C. M.; Hadjipanayis, G. C.; Tang, Z. X.; Yiping, L. *Nanostruct. Mater.* **1993**, *3*, 391.
[28] Glavee, G. N.; Klabunde, K. J.; Sorensen, C. M.; Hadjipanayis, G. C. *Langmuir* **1994**, *10*, 4726.
[29] Dragieva, I. D.; Stoynov, Z. B.; Klabunde, K. J. *Scr. Mater.* **2001**, *44*, 2187.
[30] Boutonnet, M.; Kizling, J.; Stenius, P.; Maire, G. *Colloids Surf.* **1982**, *5*, 209.
[31] Tan, Y.; Dai, X.; Li, Y.; Zhu, D. *J. Mater. Chem.* **2003**, *13*, 1069.
[32] Enüstün, B. V.; Turkevich, J. *J. Am. Chem. Soc.* **1963**, *85*, 3317.
[33] Turkevich, J.; Stevenson, P. S.; Hillier, J. *Discuss. Faraday Soc.* **1951**, *11*, 58.
[34] Yonezawa, T.; Sutoh, M.; Kunitake, T. *Chem. Lett.* **1997**, 619.
[35] Yonezawa, T.; Onoue, S.; Kimizuka, N. *Langmuir* **2000**, *16*, 5218.
[36] Huang, H. H.; Ni, X. P.; Loy, G. L.; Chew, C. H.; Tan, K. L.; Loh, F. C.; Deng, J. F.; Xu, G. Q. *Langmuir* **1996**, *12*, 909.
[37] Draganic, I. G.; Draganic, Z. D. *The Radiolysis of Water*; Academic Press: New York, 1971.
[38] Henglein, A. *Langmuir* **1999**, *15*, 6738.
[39] Ershov, B. G.; Sukhov, N. L.; Janata, E. *J. Phys. Chem. B* **2000**, *104*, 6138.
[40] Henglein, A. *J. Phys. Chem. B* **2000**, *104*, 1206.
[41] Wang, S.; Zin, H. *J. Phys. Chem. B* **2000**, *104*, 5681.
[42] Henglein, A.; Meisel, D. *Langmuir* **1998**, *14*, 7392.
[43] Hodak, J. H.; Henglein, A.; Hartland, G. V. *J. Phys.*

Chem. B **2000**, *104*, 9954.
[44] Henglein, A. *J. Phys. Chem. B* **2000**, *104*, 2201.
[45] Henglein, A.; Giersig, M. *J. Phys. Chem. B* **2000**, *104*, 5056.
[46] Mulvaney, P.; Giersig, M.; Henglein, A. *J. Phys. Chem.* **1992**, *96*, 10419.
[47] Henglein, A. *J. Phys. Chem. B* **2000**, *104*, 6683.
[48] Lee, H. J.; Je, J. H.; Hwu, Y.; Tsai, W. L. *Nucl. Instr. Methods Phys. Res. B* **2003**, *199*, 342.
[49] Chen, Y. H.; Yeh, C. S. *Chem. Commun.* **2001**, 371.
[50] Chen, Y. H.; Tseng, Y. H.; Yeh, C.-S. *J. Mater. Chem.* **2002**, *12*, 1419.
[51] Tsai, S.-H.; Liu, Y.-H.; Wu, P.-L.; Yeh, C.-S. *J. Mater. Chem.* **2003**, *13*, 978.
[52] Albuquerque, A. S.; Ardisson, J. D.; Macedo, W. A. *J. Appl. Phys.* **2000**, *87*, 4352.
[53] Chen, Q.; Rondinone, A. J.; Chakoumakos, B. C.; Zhang, Z. J. *J. Magn. Magn. Mater.* **1999**, *194*, 1.
[54] Wang, J. F.; Ponton, C. B.; Harris, I. R. *J. Magn. Magn. Mater.* **2002**, *242-245*, 1464.
[55] Xiang, L.; Deng, X. Y.; Jin, Y. *Scr. Mater.* **2002**, *47*, 219.
[56] Du, Y.; Fang, J.; Zhang, M.; Hong, J.; Yin, Z.; Zhang, Q. *Mater. Lett.* **2002**, *57*, 802.
[57] Borse, P. H.; Kankate, L. S.; Dassenoy, F.; Vogel, W.; Urban, J.; Kulkarni, S. K. *J. Mater. Sci., Mater. Electron.* **2002**, *13*, 553.
[58] Kuo, P. C.; Tsai, T. S. *J. Appl. Phys.* **1989**, *65*, 4349.
[59] Tang, Z. X.; Sorensen, C. M.; Klabunde, K. J.; Hadjipanayis, G. C. *J. Colloid Interface Sci.* **1991**, *146*, 38.
[60] Chinnasamy, C. N.; Jeyadevan, B.; Perales-Perez, O.; Shinoda, K.; Tohji, K.; Kasuya, A. *IEEE Trans. Magn.* **2002**, *38*, 2640.
[61] Li, J.; Dai, D.; Zhao, B.; Lin, Y.; Liu, C. *J. Nanopart. Res.* **2002**, *4*, 261.
[62] Wu, K. T.; Kuo, P. C.; Yao, Y. D.; Tsai, E. H. *IEEE Trans. Magn.* **2001**, *37*, 2651.
[63] Voit, W.; Kim, D. K.; Zapka, W.; Muhammed, M.; Rao, K. V. 2001; p Y7.8.1.

[64] Zhang, Z.; Han, M. *Chem. Phys. Lett.* **2003**, *374*, 91.
[65] Jana, N. R.; Gearheart, L.; Murphy, C. J. *Chem. Mater.* **2001**, *13*, 2313.
[66] Schmid, G.; Lehnert, A.; Malm, J.-O.; Bovin, J.-O. *Angew. Chem., Int. Ed. Engl.* **1991**, *30*, 874.
[67] Yu, H.; Gibbons, P. C.; Kelton, K. F.; Buhro, W. E. *J. Am. Chem. Soc.* **2001**, *123*, 9198.
[68] Zanella, R.; Giorgio, S.; Henry, C. R.; Louis, C. *J. Phys. Chem. B* **2002**, *106*, 7634.
[69] Li, Y.; Ding, J.; Chen, J.; Xu, C.; Wei, B.; Liang, J.; Wu, D. **2002**, *37*, 313.
[70] Michalski, J.; Konopka, K.; Trzaska, M. *Acta Phys. Pol., A* **2002**, *102*, 181.
[71] Fangli, Y.; Peng, H.; Chunlei, Y.; Shulan, H.; Jinlin, L. *J. Mater. Chem.* **2003**, *13*, 634.
[72] Lalla, N. P.; Hegde, M. S.; Dupont, L.; Tekaia-Elhsissen, K.; Tarascon, J.-M.; Srivastava, O. N. *Curr. Sci.* **2000**, *78*, 73.
[73] Harrison, M. T.; Kershaw, S. V.; Rogach, A. L.; Kornowski, A.; Eychmuller, A.; Weller, H. *Adv. Mater. (Weinheim, Ger.)* **2000**, *12*, 123.
[74] Pileni, M. P. *Cryst. Res. Technol.* **1998**, *33*, 1155.
[75] Pradhan, N.; Jana, N. R.; Mallick, K.; Pal, T. *J. Surf. Sci. Technol.* **2000**, *2000*, 188.
[76] Brown, K. R.; Natan, M. J. *Langmuir* **1998**, *14*, 726.
[77] Mallory, G. O.; Hajdu, J. B. *Electroless Plating: Fundamentals and Applications*; American Electroplaters and Surface Finishers Society: Orlando, FL, 1990.
[78] Platonova, O. A.; Bronstein, L. M.; Solodovnikov, S. P.; Yanovskaya, I. M.; Obolonkova, E. S.; Valetsky, P. M.; Wenz, E.; Antonietti, M. *Colloid Polym. Sci.* **1997**, *275*, 426.
[79] Ahmed, S. R.; Kofinas, P. *Macromolecules* **2002**, *35*, 3338.
[80] Rabelo, D.; Lima, E. C. D.; Reis, A. C.; Nunes, W. C.; Novak, M. A.; Garg, V. K.; Oliveira, A. C.; Morais, P. C. *Nano Lett.* **2001**, *1*, 105.
[81] Bronstein, L. M.; Chernyshov, D. M.; Valetsky, P. M.; Wilder, E. A.; Spontak, R. J. *Langmuir* **2000**, *16*, 8221.

[82] Liang, Z.; Susha, A.; Caruso, F. *Chem. Mater.* **2003**, *15*, 3176.
[83] Marinakos, S. M.; Novak, J. P.; Brousseau, L. C., III; House, A. B.; Edeki, E. M.; Feldhaus, J. C.; Feldheim, D. L. *J. Am. Chem. Soc.* **1999**, *121*, 8518.
[84] Nair, A. S.; Renjis, T. T.; Suryanarayanan, V.; Pradeep, T. *J. Mater. Chem.* **2003**, *13*, 297.
[85] Zhao, M.; Crooks, R. M. *Angew. Chem., Int. Ed. Engl.* **1999**, *38*, 364.
[86] Crooks, R. M.; Zhao, M.; Sun, L.; Chechik, V.; Yeung, L. K. *Acc. Chem. Res.* **2001**, *34*, 181.
[87] Kim, M.; Sohn, K.; Na, H. B.; Hyeon, T. Nano Lett. 2002, 2, 1383. McHenry, M. E.; Subramoney, S. In Fullerenes: Chemistry,
[88] *Physics, and Technology*; Kadish, K. M., Ruoff, R. S., Eds.; Wiley: New York, 2000.
[89] Morley, K. S.; Marr, P. C.; Webb, P. B.; Berry, A. R.; Allison, F. J.; Moldovan, G.; Brown, P. D.; Howdle, S. M. *J. Mater. Chem.* **2002**, *12*, 1898.
[90] Evans, D. F.; Wennerstrom, H. The Colloidal Domain, where Physics, Chemistry and Biology Meet; VCH: New York, 1999.
[91] Link, S.; El-Sayed, M. A. *Int. Rev. Phys. Chem.* **2000**, *19*, 409.
[92] Link, S.; El-Sayed, M. A. *Annu. Rev. Phys. Chem.* **2003**, *54*, 331.
[93] Kreibig, U.; Vollmer, M. *Optical Properties of Metal Clusters*; Springer: Berlin, Germany, 1995.
[94] Kerker, M. *The Scattering of Light and Other Electromagnetic Rediation*; Academic: New York, 1969.
[95] Bohren, C. F.; Huffman, D. R. *Absorption and Scattering of Light by Small Particles*; Wiley: New York, 1983.
[96] Creighton, J. A.; Eadon, D. G. *J. Chem. Soc., Faraday Trans.* **1991**, *87*, 3881.
[97] Ashcroft, N. W.; Mermin, N. D. *Solid State Physics*; Saunders College: Philadelphia, PA, 1976.
[98] Schmid, G. Metals. In *Nanoscale Materials in Chemistry*; Klabunde, K. J., Ed.; Wiley-Interscience:

New York, 2001; Chapter 2, p 15.
[99] Mie, G. *Ann. Phys.* **1908**, *25*, 329.
[100] Schaaff, T. G.; Shafigullin, M. N.; Khoury, J. T.; Vezmar, I.; Whetten, R. L.; Cullen, W. G.; First, P. N.; Gutierrez-Wing, C.; Ascensio, J.; Jose-Yacaman, M. J. *J. Phys. Chem. B* **1997**, *101*, 7885.
[101] Alvarez, M. M.; Khoury, J. T.; Schaaff, T. G.; Shafigullin, M. N.; Vezmar, I.; Whetten, R. L. *J. Phys. Chem. B* **1997**, *101*, 3706.
[102] Hostetler, M. J.; Wingate, J. E.; Zhong, C. J.; Harris, J. E.; Vachet, R. W.; Clark, M. R.; Londono, J. D.; Green, S. J.; Stokes, J. J.; Wignall, G. D.; Glish, G. L.; Porter, M. D.; Evans, N. D.; Murray, R. W. *Langmuir* **1998**, *14*, 17.
[103] Kawabata, A.; Kubo, R. *J. Phys. Soc. Jpn.* **1966**, *21*, 1765.
[104] Genzel, L.; Martin, T. P.; Kreibig, U. *Z. Phys. B* **1975**, *21*, 339.
[105] Ruppin, R.; Yatom, H. *Phys. Stat. Solidi B* **1976**, *74*, 647.
[106] Cini, M. *J. Opt. Soc. Am.* **1981**, *71*, 386.
[107] Wood, D. M.; Aschcroft, N. W. *Phys. Rev. B* **1982**, *25*, 6255.
[108] Kraus, W. A.; Schatz, G. C. *J. Chem. Phys.* **1983**, *79*, 6130.
[109] Hache, F.; Richard, D.; Flytzanis, C. *J. Opt. Am. Soc. B* **1986**, *3*, 1647.
[110] Yannouleas, C.; Broglia, R. A. *Ann. Phys.* **1992**, *217*, 105.
[111] Brack, M. *Rev. Mod. Phys.* **1993**, *65*, 677.
[112] Bonacic-Koutecky, V.; Fantucci, P.; Koutecky, J. *Chem. Rev.* **1991**, *91*, 1035.
[113] Persson, N. J. *Surf. Sci.* **1993**, *281*, 153.
[114] Gans, R. *Ann. Phys.* **1915**, *47*, 270.
[115] Papavassiliou, G. C. *Prog. Solid State Chem.* **1980**, *12*, 185.
[116] Link, S.; Mohamed, M. B.; El-Sayed, M. A. *J. Phys. Chem. B* **1999**, *103*, 3073.
[117] van der Zander, B. M. I.; Bohmer, M. R.; Fokkink, L. G. J.; Schonenberger, C. *J. Phys. Chem. B* **1997**, *101*,

852.
[118] Mohamed, M. B.; Ismael, K. Z.; Link, S.; El-Sayed, M. A. *J. Phys. Chem. B* **1998**, *102*, 9370.
[119] Whittle, D. G.; Burstein, E. *Bull. Am. Phys. Soc.* **1981**, *26*, 777.
[120] Boyd, G. T.; Yu, Z. H.; Shen, Y. R. *Phys. Rev. B* **1986**, *33*, 7923.
[121] Moshovists, M. *Rev. Mod. Phys.* **1985**, *57*, 783.
[122] Heritage, J. P.; Bergman, J. G.; Pinczuk, A.; Worlock, J. M. *Chem. Phys. Lett.* **1979**, *67*, 229.
[123] Apell, P.; Monreal, R. *Phys. Scr.* **1988**, *38*, 174.
[124] Plekhanov, V. G.; Siliukova, T. V. *Sov. Phys. Solid State* **1990**, *32*, 1268.
[125] Mooradian, A. *Phys. Rev. Lett.* **1969**, *22*, 185.
[126] Chen, C. K.; Heinz, T. F.; Ricard, D.; Shen, Y. R. *Phys. Rev. B* **1983**, *27*, 1965.
[127] Boyd, G. T.; Rasing, T.; Leite, J. R. R.; Shen, Y. R. *Phys. Rev. B* **1984**, *30*, 519.
[128] Mohamed, M. B.; Volkov, V. V.; Link, S.; El-Sayed, M. A. *Chem. Phys. Lett.* **2000**, *317*, 517.
[129] Wilcoxon, J. P.; Martin, J. E.; Parsapour, F.; Wiedenman, B.; Kelley, D. F. *J. Chem. Phys.* **1998**, *108*, 9137.
[130] Hao, E.; Kelly, K. L.; Hupp, J. T.; Schatz, G. C. *J. Am. Chem. Soc.* **2002**, *124*, 15182.
[131] Sun, Y.; Mayers, B.; Xia, Y. *Nano Lett.* **2003**, *3*, 675.
[132] Murray, C. B.; Norris, D. J.; Bawendi, M. G. *J. Am. Chem. Soc.* **1993**, *115*, 8706.
[133] Alivisatos, A. P. *J. Phys. Chem.* **1996**, *100*, 13226.
[134] Nirmal, M.; Brus, L. *Acc. Chem. Res.* **1999**, *32*, 407.
[135] Alivisatos, A. P. *Endeavour* **1997**, *21*, 56.
[136] Ahmadi, T. S.; Wang, Z. L.; Green, T. C.; Henglein, A.; El-Sayed, M. A. *Science* **1996**, *272*, 1924.
[137] Narayanan, R.; El-Sayed, M. A. *Nano Lett.* **2004**, *4* (7), 1343.
[138] Narayanan, R.; El-Sayed, M. A. *J. Phys. Chem. B* **2004**, *108* (18), 5726.
[139] Li, Y.; El-Sayed, M. A. *J. Phys. Chem. B* **2001**, *105*, 8938-8943.
[140] Narayanan, R.; El-Sayed, M. A. *J. Am. Chem. Soc.*

2004, *126* (23), 7419.
[141] Roucoux, A.; Schulz, J.; Patin, H. *Chem. Rev.* **2002**, *102* (10), 3757.
[142] Moiseev, I. I.; Vargatfik, M. N. *Russ. J. Gen. Chem.* **2002**, *72* (4), 512.
[143] Mayer, A. B. R. *Polym. Adv. Technol.* **2001**, *12* (1-2), 96.
[144] Boennemann, H.; Braun, G.; Brijoux, G.; Brinkman, R.; Tilling,A.; Seevogal, K.; Siepen, K. *J. Organomet. Chem.* **1996**, *520* (1-2), 143.
[145] Duff, D. G.; Baiker, A. *Stud. Surf. Sci. Catal.* **1995**, *91*, 505.
[146] Bradley, J. S. In *Clusters and Colloids: From Theory to Application*; Schmid, G., Ed.; VCH: New York, 1994; pp 459- 536.
[147] Johnson, Brian, F. G. *Top. Catal.* **2003**, *24* (1-4), 147.
[148] Corain, B.; Centomo, P.; Lora, S.; Kralik, M. *J. Mol. Catal. A: Chem.* **2003**, *204-205*, 755.
[149] Wieckowski, A.; Savinova, E. R.; Vayenas, C. G. *Catal. Electrocatal. Nano. Surf.* **2003**, 847.
[150] Santra, A. K.; Goodman, D. W. *Catal. Electrocatal. Nano. Surf.* **2003**, 281.
[151] Haruta, M. *Chem. Rec.* **2003**, *3* (2), 75.
[152] Bell, A. T. *Science* **2003**, *299* (5613), 1688.
[153] Thomas, J. M.; Johnson, B. F. G.; Raja, R.; Sankar, G.; Midgley, P. A. *Acc. Chem. Res.* **2003**, *36* (1), 20.
[154] Somorjai, G. A.; Borodko, Y. G. *Catal. Lett.* **2001**, *76* (1-2), 1.
[155] Rupprechter, G.; Freund, H.-J. *Top. Catal.* **2001**, *14* (1-4), 3.
[156] Eppler, A.; Rupprechter, G.; Guczi, L.; Somorjai, G. A. *J. Phys. Chem. B* **1997**, *101* (48), 9973.
[157] Chen, S.; Kucernak, A. *J. Phys. Chem. B*, **2004**, *108* (10), 3262.
[158] Liu, Z.; Lee, J. Y.; Chen, W.; Han, M.; Gan, L. M. *Langmuir* **2004**, *20* (1), 181.
[159] Yang, C.; Kalwei, M.; Schuth, F.; Chao, K. *Appl. Catal. A: Gen.* **2003**, *254* (2), 289.
[160] Lang, H.; May, R. A.; Iversen, B. L.; Chandler, B. D. *J. Am. Chem. Soc.* **2003**, *125* (48), 14832.

[161] Balint, I.; Miyazaki, A.; Aika, K. *Phys. Chem. Chem. Phys.* **2004**, *6* (9), 2000.
[162] Ingelsten, H. H.; Beziat, J.; Bergkvist, K.; Palmqvist, A.; Skoglundh, M.; Hu, Q.; Falk, L. K. L.; Holmberg, K. *Langmuir* **2002**, *18* (5), 1811.
[163] Claus, P.; Hofmeister, H. *J. Phys. Chem. B* **1999**, *103* (14), 2766.
[164] Suzuki, K.; Yumura, T.; Mizuguchi, M.; Tanaka, Y.; Chen, C.-W.; Akashi, M. *J. Appl. Polym. Sci*. **2000**, *77*, 2678.
[165] Chen, C.-W.; Chen, M.-Q.; Serizawa, T.; Akashi, M. *Chem. Commun.* **1998**, 831.
[166] Chen, C.-W.; Serizawa, T.; Akashi, M. *Chem. Mater.* **1999**, *11*, 1381.
[167] Yang, M. X.; Gracias, D. H.; Jacobs, P. W.; Somorjai, G. A. *Langmuir* **1998**, *14* (6), 1458.
[168] Eppler, A. S.; Rupprechter, G.; Anderson, E. A.; Somorjai, G. A. *J. Phys. Chem. B* **2000**, *104* (31), 7286.
[169] Grunes, J.; Zhu, J.; Anderson, E. A.; Somorjai, G. A. *J. Phys. Chem. B* **2002**, *106* (44), 11463.
[170] http://www-user.tu-hemnitz.de/~schulze/PRAKTIKA/HREM_AN.pdf
[171] http://www.isis.rl.ac.uk/largescale/loq/documents/sans.htm
[172] V.F. Sears, *Neutron News* **1992**, *3*, 26.
[173] H.C. van de Hulst, "*Light Scattering by Small Particles*", John Wiley, 1957.
[174] I. Livsey, *J. Chem. Soc., Far. Trans. 2* **1987**, *83*, 1445.
[175] Y. Muroga, *Macromol.* **1988**, *21*, 2751.
[176] S.-H. Chen and J.Teixeira, *Phys. Rev. Lett.* **1986**, ***57***, 2583.
[177] J.Teixeira, *J.Appl.Cryst.* **1988**, *21*, 781.
[178] R.H. Ottewill, "*Small Angle Neutron Scattering*", in "*Colloidal Dispersions*", J.W. Goodwin (editor), Special Publication No. 43, Royal Society of Chemistry, 1982
[179] Moon, R. M.; Riste, T.; Koehler, W. C. *Phys. Rev.* **1969**, *181*, 920-931.
[180] Keller, T.; Krist, T.; Danzig, A.; Keiderling, U.; Mezei, F.; Wiedenmann, A. *Nucl. Instrum. Methods Phys. Res.,*

Sect. A **2000**, *451*, 474-479.
[181] Wiedenmann, A. *J. Appl. Crystallogr.* **2000**, *33*, 428-432.
[182] Wiedenmann, A. In *Lecture Notes in Physics*; Odenbach, S., Ed.; Springer: Berlin, 2002; pp 33-61.
[183] Heinemann, A.; Wiedenmann, A. *J. Appl. Crystallogr.* **2003**, *36*, 845-849.
[184] A.Wiedenmann, *Mater. Sci. Forum* **1999**, *312-314*, 315.
[185] U. Lembke, A. Hoell, R. Kranold, R. Müller, G. Goerick, R. Gilles, A. Wiedenmann, *J. Appl. Phys.* **1999**, *85*, 2279.
[186] T.Keller, T.Krist, A.Danzig, U.Keiderling, F.Mezei, A.Wiedenmann; *Nuclear Instrum. Methods Phys. Res.* **2000**, *A 451*, 474-479.
[187] www.afmuniversity.org
[188] G. Binig, C.F. Quate, Ch. Geber, *Phys. Rev. Letters*, **1986**, *56* (9), 930.
[189] H. Heinzelmann, B. Hecht, L. Novotny, and D.W. Pohl. *J. Microsc*. **1995**, *177*, 115.
[190] Nano World Data Sheet- www.nanoworld.com
[191] J.E. Sader, J.W.M. Chon and P. Mulvaney, *Rev. Sci. Instrum*. **1999**, *70*, 3697.
[192] Optimizing AC-Mode Atomic Force Microscopy, Scanning, Vol. 18, No 5 (1996) 339-343, With H. Ho.
[193] A. Ulcinas, V. Snitka, *Ultramicroscopy* **2001**, *86*, 1-2, 217.

2. Clusters of Poly(acrylates) and Silver Nanoparticles [1]

2.1. Introduction

Poly(acrylic acids)-silver nanocomposites have attracted much interest in the last years due to the wide range of their applications that span from inkjet printing [2] and the creation of stimuli-responsive films [3] to the enhancement of fluid thermal conductivity [4] and as surface-enhanced Raman spectroscopy substrates [5]. The early stages of silver reduction in the presence of poly(acrylic acid) chains have been deeply investigated by Ershov and Henglein in radiolysis pulse experiments with γ-rays by means of UV-visible absorption spectroscopy [6,7]. Their studies showed that silver atoms formed during the irradiation are complexed by Ag^+ ions and oligomeric clusters are formed through coalescence processes. These complexes are further reduced to form larger clusters, and eventually, metallic nanoparticles are formed. Recently, Huber et al. studied the formation of silver nanoparticles embedded in long-chain sodium poly-(acrylates) through time-resolved static light scattering and revealed that the addition of silver ions induces coil shrinking and aggregation of the polyelectrolyte, and when exposed to UV radiation, small silver nanoparticles are formed within the shrunk poly(acrylate) coils [8]. Poly(acrylates) can actually act as growth modifiers in inverse micellar solutions for silver nanoparticles [9].

Small-angle X-ray scattering is a powerful tool to investigate nanoparticles' size, shape, and structure [10]. Remita et al. reported on the X-ray radiolysis induced synthesis of silver particles, where X-rays are used for the synthesis and to follow in situ the formation of the nanoparticles [11]. Korgel et al. also used SAXS investigation to characterize dodecanethiol-capped silver nanocrystal and to analysize the order-disorder transition of a self-organized superlattice created with core-shell particles [12]. SAXS is also useful to

have insights into the arrangement of capping molecules on the surface of silver nanoparticles [13] for the characterization of silver nanoparticles synthesized in the interlamellar space of a layered kaolinite clay material [14,15] and of hybrid systems where silver nanoparticles interact with SDS based lamellar phases [16]. Despite such a large number of reports on this subject, to the best of our knowledge, a fine control of the size and polydispersity of silver nanoparticles prepared in the presence of polyelectrolytes in water is still a major issue. In this work, we explored this effect through SAXS measurements. Nanoparticles were obtained through the reduction in water of silver ions in the presence of poly(acrylates) as templating agents. The carboxylic groups/silver ratio was kept constant, while the polymer chain length and the reduction method were changed in order to understand the role of the different synthetic parameters on the final size and shape of the silver clusters. The samples were fully characterized by small angle X-ray scattering and the results confirmed through UV-visible absorption and transmission electron microscopy. The development of new clothing products based on the immobilization of nanoparticles on textile fibers for specific purposes has recently received a growing interest [17–25]. In particular, during the past decade, a great effort has been devoted to the preparation of silver nanoparticles and to the study of their antimicrobial properties [26–28], which have been known for centuries [29]. Recently, the wide-spectrum antimicrobial activity of silver has been exploited in a large number of applications, ranging from the coating of medical devices [30–35] to the direct treatment of wounds or burns [36–39].

Some bacterial strains develop a significant resistance toward antibiotics [40]. For this reason, silver is actually receiving a renewed interest as its antimicrobial activity is known to be efficient against hundreds of bacterial strains [41–44]. Moreover, silver has low toxicity, which is especially important for topical antibacterial treatments [42]. This makes it a very interesting material when designing functional clothing products through the surface treatment. By decreasing the size of the particles, the specific area

available for chemical reactions and surface interactions is increased, and the antimicrobial performance is more efficient [44]. Therefore, the size control in the synthesis of silver nanoparticles represents a crucial step in the preparation of formulations with specific, desired functionalities. A variety of methods for the loading of silver nanoparticles onto textiles has been recently used. Silver-incorporating fibers were prepared by infiltration of silver nitrate on electrospun polyurethane matrixes followed by reduction with sodium borohydride [45]. Silk and nylon fibers loaded with silver nanoparticles were obtained by following the layer-by-layer deposition method [46]. Instead, for cotton, silver nanoparticles were obtained directly in situ by immersing the fabric in a silver nitrate solution, followed by an autoclave cycle [47]. In our study, the silver nanosols have been used to functionalize cotton, polyester, and wool by simply immersing the textiles into the dispersions in order to obtain antimicrobial fabrics. No coating material was spread on the surface of the loaded fabrics in order to optimize the contact between the Ag-treated textile and the bacterial substrate. The antimicrobial activity of such surface-modified fabrics was tested against *Staphylococcus aureus*, *Staphylococcus epidermidis*, *Pseudomonas aeruginosa*, and *Candida albicans*. The results demonstrate the high efficiency of the treatment with the silver nanoparticle dispersions.

2.2. Experimental Section

$AgNO_3$ was purchased from Riedel-de-Haën, poly(acrylates) (sodium salt solutions; M_W = 1200 g/mol, 45 wt% in water and M_W = 15000 g/mol, 35 wt% in water) and $NaBH_4$ were obtained from Aldrich (Milan, Italy). Wool, cotton, and polyester samples were a kind gift from Grado Zero Espace (Florence, Italy). Water was purified with a Millipore system (resistivity 18 MΩ· cm).

Synthesis. Silver nanosols were prepared from $AgNO_3$ and poly(acrylates) (PAA) as the templating material. Two

different reduction methods were used, $NaBH_4$ reduction (method A) and UV radiation exposure (method B).
In order to investigate the effect of the polymer chain length on the nanoparticles size, two PAA molecular weights (1200 and 15000 g/mol; abbreviated as PAA1200 and PAA15000, respectively) were used. In all cases, the synthesis was carried out with a constant PAA/Ag^+) 10 wt/wt ratio. A 0.5% wt/wt concentration of silver was used.
In a typical experiment, 125 mL of a 1% wt/wt $AgNO_3$ solution and 125 mL of a 10% wt/wt PAA solution were mixed and kept under vigorous stirring at room temperature for 10 min. The reduction with $NaBH_4$ was performed by adding 10 mL of a 0.1 M $NaBH_4$ solution (refrigerated in an ice bath) to the solution containing PAA and Ag^+, with an addition rate of 1 mL/min.
UV reduction was performed by irradiating the solutions containing PAA and Ag^+ to a UV lamp for 2 h. The samples, contained in 10 mm path length glass cells, were irradiated with a 130 W Hg lamp (Oriel Arc Lamp Source). The source was equipped with a water-cooled filter holder and focused to irradiate the whole sample.
In order to check the effect of pH on the nanoparticles properties, the pH of the silver nanosols was adjusted from their initial value (around pH 8) to pH 4 and 11 by adding a proper amount of a 0.1 M HCl or KOH aqueous solutions.

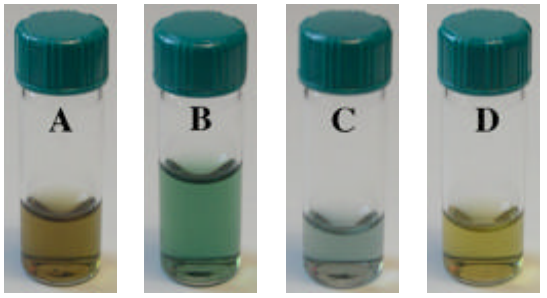

Figure 2.1. Silver nanosols prepared at pH ≈ 8. (A) $NaBH_4$ reduction, PAA1200; (B) $NaBH_4$ reduction, PAA15000; (C) UV reduction, PAA1200; (D) UV reduction, PAA15000.

Textile Treatment. The fabric samples (cotton, wool, and polyester) were conditioned at constant relative humidity (RH 33%) and temperature (20 °C). Wool and cotton samples (5 cm × 5 cm) were soaked for 15 min at room temperature in the Ag nanoparticles dispersion under magnetic stirring. The clothes were then squeezed to remove the excess dispersion, rinsed, and dried in an oven at 130 °C for 15 min at atmospheric pressure (dry heat).

Plating of Loaded Textiles. For antimicrobial tests, a modified standard procedure (agar plate diffusion test/CEN/TC 248 WG 13) was used. The original procedure involves *St. aureus* only. In the present study, we extended the method to three different strains, as indicated below. Suspensions of *Staphylococcus aureus* ATCC 25923, *Staphylococcus epidermidis* from clinical specimen, *Pseudomonas aeruginosa* ATCC 27853, and *Candida albicans* ATCC 10231 were prepared with a turbidity of 0.5 Mc Farland units (about $1.38 \cdot 10^6$, $3 \cdot 10^6$, $3 \cdot 10^8$, and $4.5 \cdot 10^5$ UFC/mL, respectively). A volume of 100 μL of the suspensions was spread on TSA (tryptone-soya agar growth medium from Oxoid, Milan, Italy) in a Petri dish, and the fabric sample (3 × 3 cm) was adjusted on the top of the medium. *St. aureus* and *St. epidermidis* dishes were incubated at 37 °C in a thermostat at room pressure in aerobic atmosphere for 24 h, while *Ps. aeruginosa* and *C. albicans* dishes were incubated at 30 °C for 72 h. At the end of the incubation step, the effect of silver-coated textiles on the population of the bacteria strains was evaluated in terms of the inhibition ring around the fabric portion (at least 1 mm) and of growth underneath of/over the textile. Each sample (cotton, wool, and polyester) was compared to a nontreated blank reference.

UV-Visible Absorption. Absorbance spectra were collected with a Perkin-Elmer Lambda 900 spectrophotometer for solutions of chemicals and with a Perkin-Elmer Lambda equipped with a 60 mm integrating sphere for fabrics. In order to avoid signal saturation, the liquid samples were

diluted by a factor of 70, with a final [Ag] of about $7 \cdot 10^{-3}$ wt%.

Transmission Electron Microscopy. TEM analysis was carried out with a JEM 3010 (JEOL) electron microscope operating at 300 kV, with point-to-point resolution at the Scherzer defocus of 0.17 nm. Specimens for TEM analysis were sonicated in water and then transferred as a suspension to a copper grid covered with a lacey carbon film.

Small-Angle Scattering of X-rays. SAXS experiments were carried out with a Nanoviewer apparatus (Rigaku), equipped with a mercury charge coupled device detector (CCD) containing 1024 × 1024 pixels of width 68 μm. Cu K_α radiation at λ=1.542 Å was emitted by a Micromax007 X-ray rotating anode (Rigaku), operating at a maximum power of 0.8 kW with a circular focal spot size of 70 μm. X-rays were conditioned using the confocal max-flux mirror (Rigaku/Osmic) in order to totally remove the Cu K_β component maintaining the high flux and symmetry of the rotating anode source. X-ray collimation was performed through a three-point collimation system. The sample-to-detector distance was about 605 mm. The volume between the sample and the detector was kept under vacuum during the measurements to minimize scattering from the air. The Q range was calibrated using silver behenate, which is known to have a well-defined lamellar structure (d=58.48 Å) [48]. Scattering curves were monitored in a Q range from 0.01 to 0.45 $Å^{-1}$. The samples were filled into a 1 mm quartz capillary using a syringe and sealed with an epoxyde glue. The temperature was controlled by a Peltier device, with an accuracy of ±0.1 °C. The working temperature was 20 °C. All 2D spectra were corrected for the dark current; the dezinger procedure was applied to all images in order to remove spurious signals. The H_2O/empty cell contribution (quartz capillary) was removed using the relative sample/empty transmissions. Finally, 2-D spectra were azimuthally averaged in order to obtain the correspondent 1-D scattering intensity distribution.

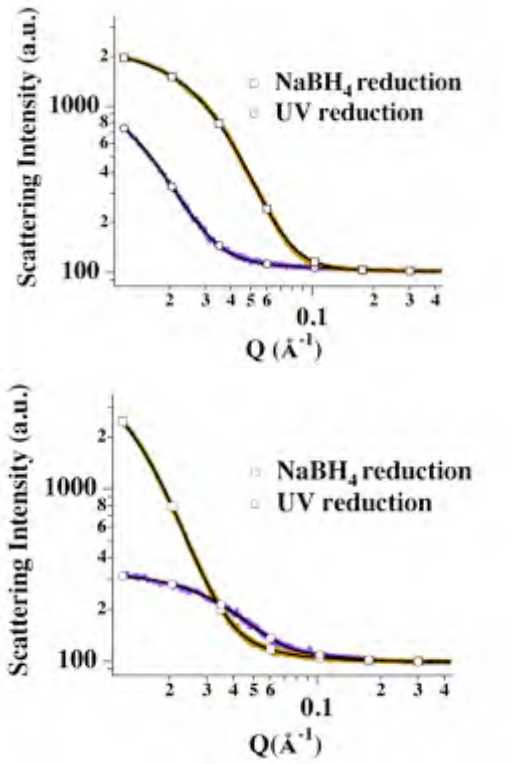

Figure 2.2. SAXS results. Top: A and C samples. Bottom: B and D samples. Error bars are less than the marker size.

SAXS Data Analysis. SAXS results were fitted according to a bimodal size distribution of spherical particles. In a small angle scattering experiment, the measured intensity of the radiation, $I(Q)$, scattered by a collection of uniform particles is given by [49]:

$$I(Q) = \phi \cdot P(Q) \cdot S(Q) + bkg \qquad (2.1)$$

where ϕ is the particle volume fraction, $P(Q)$ is the intraparticle structure factor, $S(Q)$ is the interparticle structure factor, and bkg is the incoherent background. Briefly, $P(Q)$ describes how $I(Q)$ is modulated by interference effects of the radiation scattered by different parts of the same scattering object (i.e., in the present, case the silver nanoparticle). As a result, $P(Q)$ gives direct information on the shape of the scattering object, and it is usually referred to as the "form

factor". On the other hand, $S(Q)$ reflects the modulation of the intensity distribution due to interference effects originating from the radiation scattered by different scattering objects. Therefore, it depends on the degree of local order in the sample. In our case, the final silver concentration was always about 0.32% wt/wt, corresponding to a volume fraction ϕ of about $3 \cdot 10^{-4}$. Due to the very low concentration of the scattering objects, the interparticle correlations in our samples are negligible, and the structure factor is assumed to be equal to 1, leading to a simplified version of eq. 2.1 where S(Q) is missing.
The experimental results were modeled according to a bimodal distribution of scattering particles. Then, eq. 2.1 could be simplified and expanded by taking into consideration a bimodal distribution of the particle size:

$$I(Q)=\phi_{small} \cdot P_{small}(Q)+ \phi_{large} \cdot P_{large}(Q)+bkg \qquad (2.2)$$

where the subscripts stand for the distribution of smaller and larger particles, respectively. It is worth noting that the experimental setup used in these measurements does not allow us to obtain absolute intensities but only intensities in arbitrary units. However, the obtained scattering intensities were corrected for the empty cell contribution and normalized according to the transmissions; therefore the magnitude of scattering and the experimental intensities are reliable on a relative scale and are proportional to the absolute intensity through a coefficient K that depends on the beam intensity and on the geometry of the apparatus. This means that, although in our experiments we do not know the actual values of ϕ_{small} and ϕ_{large}, we can access their ratio. In fact, a correct formulation of eq 2.2 for our experiments would be:

$$I(Q)=C_{small} \cdot P_{small}(Q)+C_{large} \cdot P_{large}(Q)+bkg \qquad (2.3)$$

where C_{small} and C_{large} are defined in eqs 2.4 and 2.5, respectively:

$$C_{small}=K \cdot \phi_{small} \qquad (2.4)$$

$$C_{large}=K \cdot \phi_{large} \quad (2.5)$$

The C_{small}/C_{large} ratio is equal to $\phi_{ratio} = \phi_{small}/\phi_{large}$; therefore, throughout the paper, we will refer only to ϕ_{ratio}.

In order to account for the shape and size distribution of the scattering objects, we used the particle form factor proposed by Bartlett and Ottewill for polydisperse spherical particles with a core-shell structure [50]. In this form factor, the spherical particles have a constant shell thickness and a core described by a Schultz distribution of radii. The contribution to the total scattering intensity arising from such objects was calculated according to the following equations:

$$P(Q) = \frac{1}{V}\int_0^\infty G(r_c) \cdot F^2(Qr_c)dr_c \quad (2.6)$$

$$F(Qr_c) = \frac{4\pi}{Q^3}(\rho_{shell} - \rho_{core})\left\{\rho_{scaled} \cdot j\left(Qr_c + \frac{t}{r_c}Qr_c\right) - j(Qr_c)\right\} \quad (2.7)$$

$$\rho_{scaled} = (\rho_{solv}-\rho_{shell}) \cdot (\rho_{core}-\rho_{shell}) \quad (2.8)$$

$$j(Qr_c) = \sin(Qr_c)-(Qr_c) \cdot \cos(Qr_c) \quad (2.9)$$

where r_c is the core radius, t the shell thickness, V_p the particle volume, and ρ_{core}, ρ_{shell}, and ρ_{solv} the scattering length densities (SLDs) for the core, the shell, and the solvent, respectively.

The $G(r_c)$ function is the normalized probability of finding a particle with a core radius between r_c and $r_c + dr_c$, and it accounts for the polydispersity of the cores according to the Schultz distribution [51,52]:

$$G(r_c) = \frac{r_c^Z}{\Gamma(Z+1)}\left(\frac{Z+1}{\langle r_c \rangle}\right)^{Z+1} \cdot \exp\left[-\frac{r_c}{r_{avg}}(Z+1)\right] \quad (2.10)$$

where $\Gamma(Z + 1)$ is the gamma function and the parameter Z is related to the polydispersity σ_c of the core radius through the

expression:

$$\sigma_c = \frac{\sqrt{\langle r_c^2 \rangle - \langle r_c \rangle^2}}{\langle r_c \rangle} = \frac{1}{\sqrt{Z+1}} \qquad (2.11)$$

For the fitting procedure, we used the theoretical values for the X-ray scattering length densities for silver and water, $7.71 \cdot 10^{-5}$ and $9.36 \cdot 10^{-6}$ Å^{-2}, respectively.

For sodium polyacrylate, we performed the fitting by letting its scattering length density to vary between $9.35 \cdot 10^{-6}$ (the theoretical value for poly(acrylic acid)) and $1.23 \cdot 10^{-5}$ Å^{-2} (theoretical value of sodium polyacrylate). The values returned by the fitting procedure for both the shell thickness and the difference between shell and solvent scattering length densities were always within the experimental error. This shows that the presence of the polyacrylate shell around the silver nanoparticles is not detectable in our case. Therefore, no shell contribution was taken into account any longer in our fitting procedure, and the silver nanoparticles were modeled as "naked" particles dispersed in water.

2.3. Results and Discussion

Stabilization of Silver Nanoparticles. The synthesis of the nanosols was performed at pH 8, the original pH of the sodium salt solutions of poly(acrylates). Other pH values were explored in order to check the stability range of the dispersions by adding 0.1 M KOH (up to pH 11) or HCl solutions (down to pH 4) to the original nanosols. The onset of a precipitate at pH 5 was observed, and at pH 4, the precipitation was complete, as a consequence of the full protonation of the carboxylic groups in the poly(acrylate) chains; in fact, at such pH, the polymer tails cannot prevent the nanoparticles precipitation. Therefore, the stability pH range of the PAA-templated silver nanoparticles spans between 6 and 11. In this pH range, all dispersions are clear and show different colors, as illustrated in Figure 2.1. The synthesis of the nanoparticles was then carried out at pH 8,

the polymer solution original pH. All further measurements were performed in this conditions.

2.3.1. SAXS Results

Figure 2.2 shows the experimental SAXS data and the fitting curves (see Experimental Section). The agreement between the experimental data and the calculated curves is good, indicating that the model used for the fitting was properly chosen. The parameters resulting from the fitting are reported in Table 2.1. Interestingly, all of the samples show the presence of one population of ultrasmall nanoparticles (less than 2 nm in diameter) together with another population of larger nanoparticles (see Figure 2.3). The mean radius of this second distribution of particles ranges between 3 and 5.5 nm. TEM observations (see below) are in agreement with these results. A careful inspection of the values listed in Table 2.1 shows that the relative amount of the distributions depends on the polymer molecular weight and on the reduction method.

Table 2.1. Parameters extracted from the SAXS data.

	PAA1200		*PAA15000*	
	$NaBH_4$ reduction	*UV reduction*	*$NaBH_4$ reduction*	*UV reduction*
ϕ_{ratio}	$9.45 \cdot 10^{-4}$	4.76	0.83	3.33
	Small size distribution			
r_c (nm)	0.60	0.69	0.85	0.83
σ	0.15	0.49	0.54	0.37
	Large size distribution			
R_c(nm)	2.94	4.47	5.41	3.56
σ	0.48	0.65	0.62	0.30

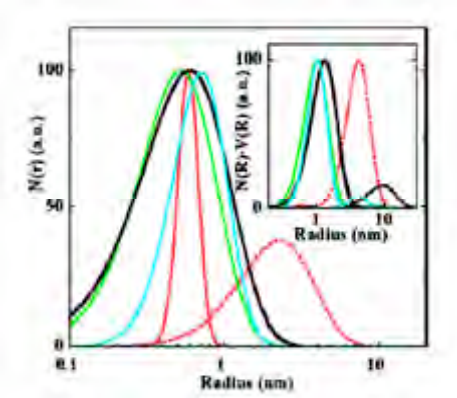

Figure 2.3. Size distributions of small (full lines) and large (dotted line) populations of Ag nanoparticles obtained from the fitting of SAXS data for the samples A (red), B (black), C (light green), and D (light blue). The bigger particle populations for B, C, and D are so small that the curves are near the baseline. The inset shows the same size distributions weighted for the particle volumes.

As far as the reduction method is concerned, when sodium borohydride is used, the population of large particles is predominant, thus leading to smaller ϕ_{ratio} values. For example, for PAA1200, the fitting returns a ϕ_{ratio} value of around 10^{-3}, while for PAA15000, we have $\phi_{ratio} = 0.83$.
On the other hand, the smaller particles dominate when UV irradiation is used. In particular, the sample with PAA1200 consists almost entirely in one population of particles, with a mean radius of about 3 nm.
Regarding the effect of the polymer molecular weight, the sample obtained with $NaBH_4$ and PAA15000 shows a significantly higher amount of ultrasmall clusters than the specimen obtained with PAA1200, where their presence is almost negligible ($\phi_{ratio}=9.5\cdot10^{-4}$). Moreover, the mean radius of the population of larger particles is considerably higher (about 5.5 instead of 2.9 nm).
During the reduction of silver in the presence of polyacrylates, the products are stabilized by the polyacrylate chain [6,7]. As a matter of fact, the idea behind this approach is to keep the nucleating sites (i.e., the polyelectrolyte-silver complexes) as far apart as possible through the electrostatic repulsion between the polyacrylate chains. The formation of

silver nanoparticles can be envisaged as ruled by two processes, (i) the nucleation along the polyacrylate chains and (ii) the growth of metallic particles through the further reduction and interaction of different nuclei. It is important to remind that all of the samples were prepared with the same ratio between acid groups and silver ions (see Materials and Methods section). This means that the number of nucleation sites (carboxylate groups) available for each Ag^+ ion is the same, although the distribution of the nucleation sites is significantly different. In fact, when a longer polymer is used, a single chain can template a large number of small nuclei and leads to the formation of one single cluster within the same chain. At the same time, the chain density in the solution is lower. Both of these factors favor the stabilization of small clusters (higher ϕ_{ratio}), and therefore, the difference in the particles size is simply due to the different chain length. The results show that when a longer chain is used in combination with $NaBH_4$, the largest clusters are obtained as a consequence of the high number of nucleating sites along the polymer chain that, during the reduction, can easily interact with each other to give nanoparticles. Therefore, the mean radius of the final nanoparticles prepared by the $NaBH_4$ reduction method with the longer polymer is around 5.5 nm. The data shown in Table 1 for the large size distribution seem to indicate that the average radius of the nanoparticles increases in going from PAA1200 to PAA15000 with $NaBH_4$ and decreases with UV irradiation. This phenomenon can be interpreted in terms of a kinetic control of the reaction. With the UV method, the formation of the Ag nanoparticles is certainly slower than that with $NaBH_4$. Therefore, the PAA chains can perform their templating effect more efficiently when the reducing agent is the UV radiation. In fact, this effect is more significant with the longer poly(acrylate) chain.

2.3.2. UV-Vis Results

The effect of both the polymer length and the reduction method on the final size distributions of the Ag nanosols is

confirmed by the different colors of the freshly prepared samples (see Figure 2.1).

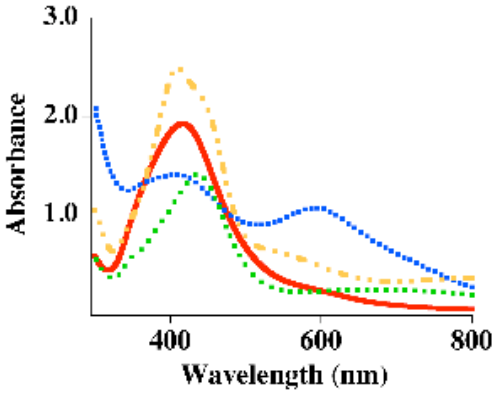

Figure 2.4. UV-visible absorbance spectra of 0.5% Ag nanoparticles: sample A (red), B (green), C (blue), and D (yellow).

In particular, the presence of ultrasmall silver clusters is confirmed by the UV-Vis absorbance results. Figure 2.4 reports the spectra of the nanosols. All samples show a strong absorption peak at around 400 nm, typical of the plasmon absorption band of silver [6,7] and a broad signal in the visible region, especially in the samples prepared by UV irradiation. The latter band is due to the formation of silver-polyacrylate complexes [6,7]. In particular, the Ag_4^{2+} clusters are known to be stabilized by polyacrylate anions and produce a broad absorption peak centered approximately at 540 nm [9]. In the same way, larger [Ag_{m+n}^{m+}-PAA^-] complexes are formed, giving rise to a broad absorption peak at longer wavelengths. These complexes (typically named as "blue species" because of the color of their nanosols) are very stable against reoxidation and represent a sort of intermediate species in the formation of larger silver nanoparticles [6,7].
Comparing the UV-vis spectra of different samples, it is interesting to note that the specimen prepared via UV reduction shows a higher amount of the [Ag_{m+n}^{m+}-PAA^-] complex. In particular, the highest amount is present in the $NaBH_4$-reduced sample with PAA1200. This evidence is consistent with the SAXS results. In fact, the values reported in Table 2.1 indicate that the amount of small nanoparticles is predominant in both UV-reduced samples. The formation of

silver nanoparticles in the presence of polyacrylates begins with the complexation of silver ions by the anion groups of the polyelectrolyte [6]. Small ionic clusters are then formed, producing the typical pink color of the early reduction stages. Afterward, these small clusters agglomerate and lead to the formation of larger blue complexes. Upon further reduction, the blue clusters break apart and form the metallic silver nanoparticles, showing the typical plasmon absorption peak. In the presence of the polyelectrolyte, all of these intermediate steps are affected, especially in terms of their stability. Therefore, the presence of a stronger absorption peak in the visible region in the UV-reduced samples reflects a slower rate in the reduction process in comparison with that of the $NaBH_4$-reduced samples. This can be then reasonably related to the presence of a population of ultrasmall nanoparticles, which represents an early stage in the nanoparticles' growth process. As in the case of the reduction process, the presence of polyacrylates significantly slows down the growth, stabilizing the smaller nanoparticles.

2.3.3. Electron Microscopy

HR-TEM results confirm the conclusions drawn on the basis of SAXS data fitting. In Figure 2.5, two representative micrographs of UV- and $NaBH_4$-reduced samples with PAA1200 are shown. The presence of two populations of silver nanoparticles is evident. The size of the particles agrees very well with the SAXS results. Therefore, we can conclude that all of the prepared nanosols consist of smaller and larger nanoparticles, with different relative amounts. The $NaBH_4$-reduced samples consist almost entirely of large metallic silver nanoparticles, while the UV-reduced samples contain mainly ultrasmall nanoparticles and some $[Ag_{m+n}^{m+}\text{-}PAA^-]$ complexes too.

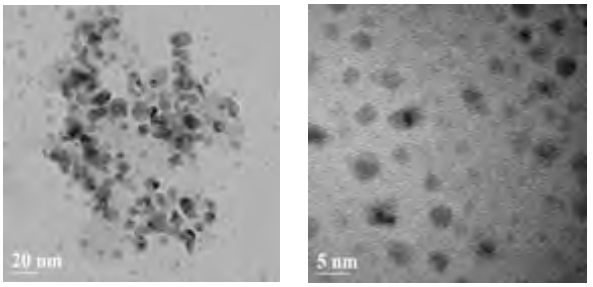

Figure 2.5. Representative TEM micrographs of an UV-reduced sample.

with the PAA1200 sample (left, magnification 80k, bright field mode) and of the $NaBH_4$-reduced sample with PAA1200 (right, magnification 400k, bright field mode).

2.3.4. Textiles and Antibacterial Activity

Once soaked in Ag nanosols, the cotton, wool, and polyester fabric samples turn colored and maintain the color after rinsing and drying, confirming the adhesion of the nanoparticles on the fabric fibers (Figures 2.6, 2.7, and 2.8).

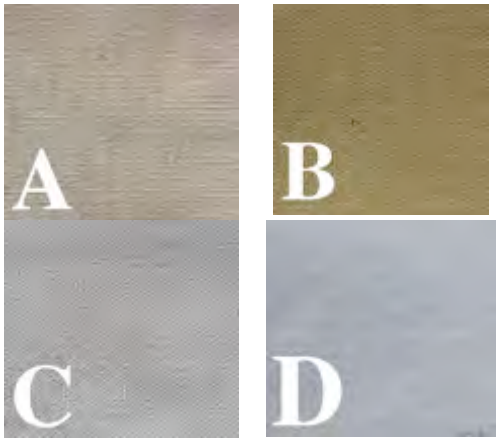

Figure 2.6. Silver-nanosol-loaded cotton fabrics. (A) $NaBH_4$ reduction, PAA1200; (B) $NaBH_4$ reduction, PAA15000; (C) UV reduction, PAA1200; (D) UV reduction, PAA15000.

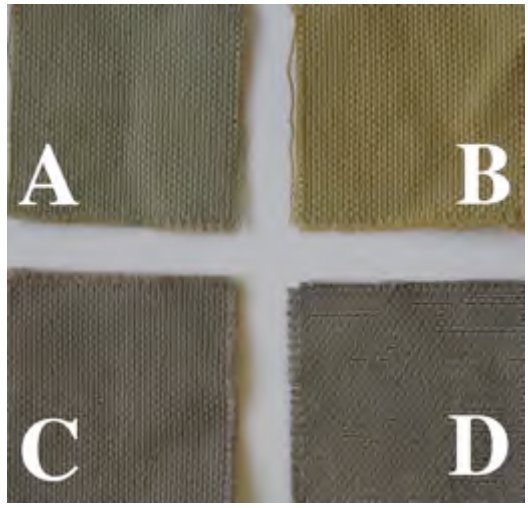

Figure 2.7. Silver-nanosol-loaded wool fabrics. (A) $NaBH_4$ reduction, PAA1200; (B) $NaBH_4$ reduction, PAA15000; (C) UV reduction, PAA1200; (D) UV reduction, PAA15000.

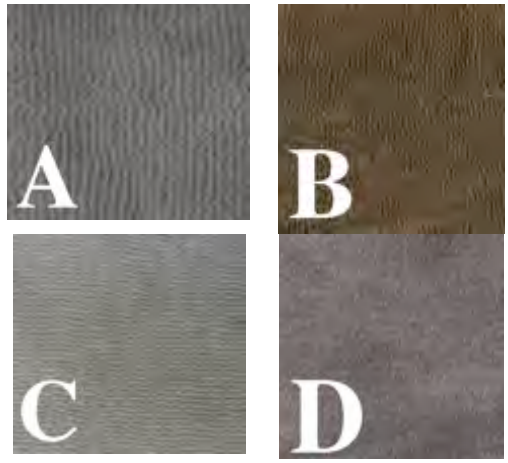

Figure 2.8. Silver-nanosol-loaded polyester fabrics. (A) $NaBH_4$ reduction, PAA1200; (B) $NaBH_4$ reduction, PAA15000; (C) UV reduction, PAA1200; (D) UV reduction, PAA15000.

Untreated polyester, natural cotton and wool samples show no absorption peak between 400 and 800 nm, while after the treatment with silver dispersions, a peak at around 400 nm appears (see Figure 2.9), indicating the presence of Ag

nanoparticles on the fabric. The treated fabric samples were washed according to the standard procedure (UNI EN ISO 26330); the absorption spectra of the treated samples before and after washing is reported in Figure 2.9, revealing the persistence of the particles on the fabric.

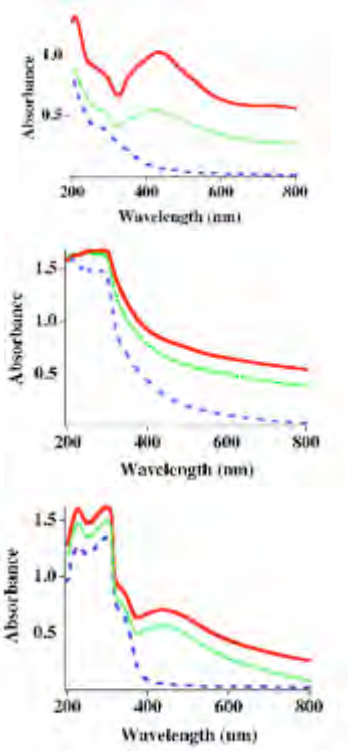

Figure 2.9. UV-vis absorbance spectra on (from top to bottom) cotton, wool, and polyester fabric. Untreated (dashed blue), Ag-nanosol-treated (red), and washed Ag-nanosol-treated (green) fabric.

The textile samples were loaded with Ag nanoparticles and checked against *Staphylococcus aureus*, *Staphylococcus epidermidis*, *Pseudomonas aeruginosa*, and *Candida albicans* cultured TSA plates in order to assess the antimicrobial activity of the silver-loaded textiles both on Gram positive and negative bacteria and on a yeast. For the fabric modification, we chose to perform the experiments with sample A; in fact, the presence of two characteristic sizes of Ag nanoparticles (see Figure 2.3) and of different pore

diameters in the fabric matrix enhances the adhesion between fabrics and nanoparticles. The antimicrobial effect of the treated textiles was assessed by evaluating different parameters, the growth of the bacteria underneath of and over the fabric and the presence of at least 1 mm of inhibition ring around the textile. Table 2.2 summarizes the results obtained on the different untreated and treated samples (cotton, wool, polyester). All untreated samples do not show the presence of the inhibition ring (see Figure 2.10). It is interesting to note that cotton prevents the growth of *St. aureus* underneath of and over the fabric. A significant inhibition ring (at least 1 mm wide) is shown in all treated cotton samples (Figure 2.11), indicating a consistent inhibition in the bacterial growth for the investigated strains, especially against *C. albicans*. In the case of wool, the untreated fabric does not interfere with the bacterial growth (see Figure 2.12). The Ag-loaded wool samples (see Figure 2.13) indicate the presence of an inhibition ring only in the case of *C. albicans*, while all the other strains are not affected by the presence of the fabric. Similarly, untreated polyester (see Figure 2.14) does not stop the microorganisms growth, while the Ag-loaded polyester samples (see Figure 2.15) strongly inhibit the growth of all of the investigated strains. In summary, the tests clearly show that the presence of the silver nanoparticles on the fabrics produces a significant inhibition effect on all studied microorganisms, and especially in the case of cotton and polyester.

TABLE 2.2: Tested Response of the Bacteria Strains to the Untreated and Ag-Loaded Samples of Cotton, Wool, and Polyester.

fabric sample	*St. aureus*	*St. epidermidis*	*Ps. aeruginosa*	*C. albicans*
untreated cotton		+, *	+	+, *
Ag-coated cotton	inh	inh	inh	inh
untreated wool	+	+	+	+
Ag-coated wool				inh
untreated polyester	+	+, *	+	+
Ag-coated polyester	inh	inh	inh	inh

"+" indicates the growth underneath the fabric; "*" indicates the growth on top of the fabric; "inh" indicates the presence of a significant (at least 1 mm) inhibition ring around the textile.

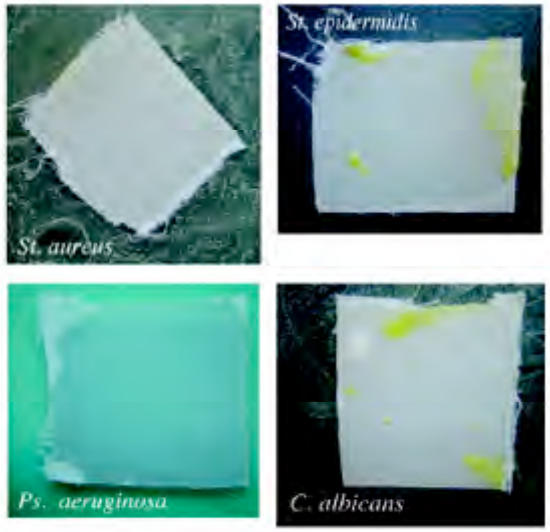

Figure 2.10. Effect of untreated cotton samples toward the growth of the investigated strains.

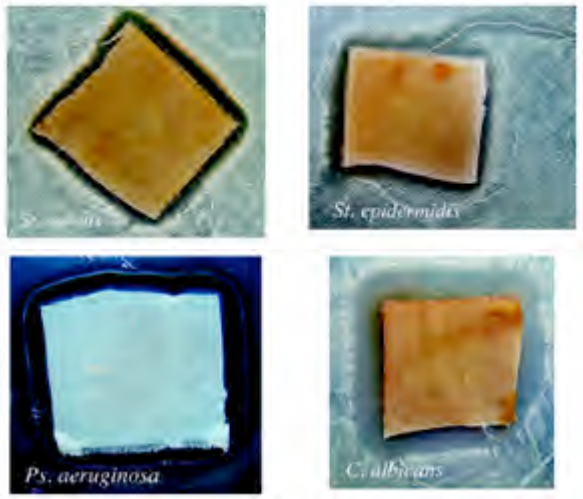

Figure 2.11. Effect of Ag-treated cotton samples toward the growth of the investigated strains.

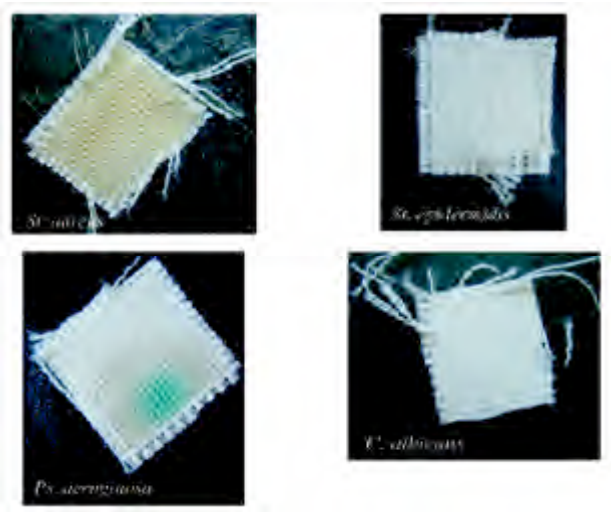

Figure 2.12. Effect of untreated wool samples toward the growth of the investigated strains.

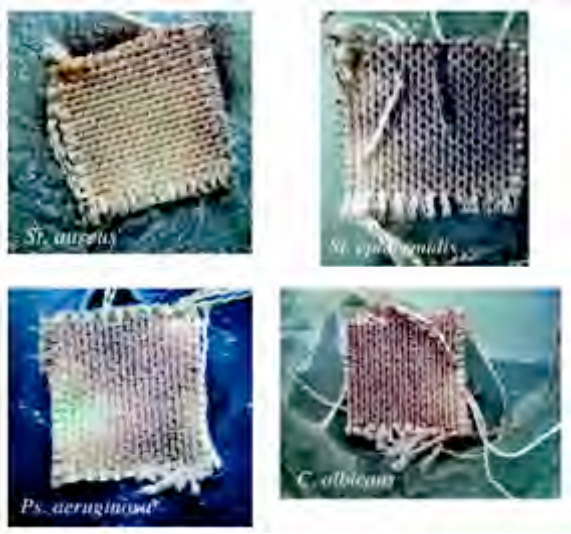

Figure 2.13. Effect of Ag-treated wool samples toward the growth of the investigated strains.

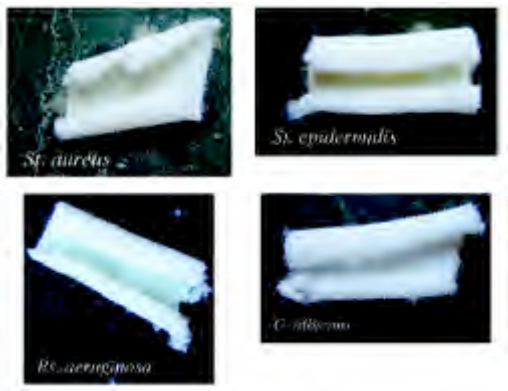

Figure 2.14. Effect of untreated polyester samples toward the growth of the investigated strains.

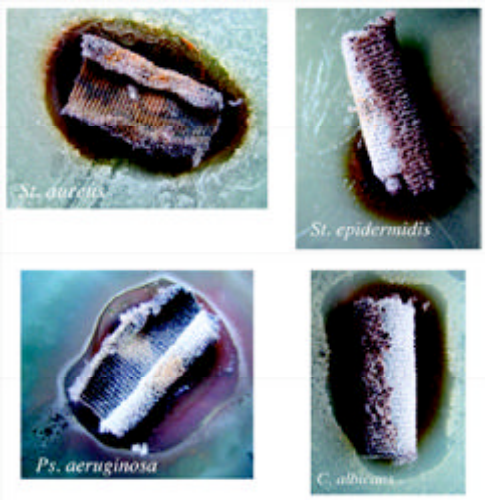

Figure 2.15. Effect of Ag-treated polyester samples toward the growth of the investigated strains.

2.4. Conclusions

A detailed characterization of silver nanoparticles obtained in the presence of polyacrylates as templating agents was conducted through small-angle X-ray scattering. Few-nanometer-sized monodisperse silver nanoparticles were synthesized in water with poly(acrylates) (PAA) of different

molecular weights (1200 and 15000 g/mol) as the templating material. The reduction of Ag^+ was carried out through sodium borohydride or by irradiation with UV light to understand the role of the reduction method on the structure of the final clusters.

The shape, size, and polydispersity of the silver nanosols were established through the SAXS data. By adopting a bimodal distribution of the scattering objects for the fitting procedure, the samples reveal the presence of a population of ultrasmall spherical nanoparticles (with a diameter lower than 2 nm) and of a population of larger particles, with a radius spanning between 3 and 6 nm. In particular, the results show that the reduction with $NaBH_4$ produces nanoparticles with a radius of 3 nm for PAA1200 and of 6 nm for PAA15000. SAXS results were confirmed by TEM and UV-visible absorption experiments. In particular, the UV-Vis spectra reveal that the samples prepared through UV exposure show a higher amount of $[Ag_{m+n}{}^{m+}\text{-}PAA^-]$ complexes (small clusters at the first stage of the silver reduction in the presence of polyacrylates), with a broad absorption peak in the visible region, and the highest amount is present in the sample with PAA1200. These results confirm the analysis of the SAXS data, which showed a predominant amount of small nanoparticles in the UV-reduced samples and of larger particles in the samples obtained through UV exposure. This behavior reflects a slower rate in the UV reduction process with respect to the $NaBH_4$ reduction method.

Cotton, wool, and polyester fabrics were functionalized with the silver nanosols by curing the textiles with the nanoparticles dispersion. The treated textiles exhibit antimicrobial activity against *Staphylococcus aureus*, *Staphylococcus epidermidis*, *Pseudomonas aeruginosa*, and *Candida albicans*, depending on the strain, as indicated by the inhibition ring and the absence of growth underneath of and on the top of the fabric.

2.5. Bibliography

[1] Falletta, E.; Bonini, M.; Fratini, E.; Lo Nostro, A.; Pesavento, G.; Becheri, A.; Lo Nostro, P.; Canton, P. and Baglioni, P. *J Phys. Chem. C*, **2008**, *112* (31) 11758-11766.

[2] Magdassi, S.; Bassa, A.; Vinetsky, Y.; Kamyshny, A. *Chem. Mater.* **2003**, *15*, 2208–2217.

[3] Ayres, N.; Boyes, S. G.; Brittain, W. J. *Langmuir* **2007**, *23*, 182– 189.

[4] Cho, T.; Baek, I.; Lee, J.; Park, S. *J. Ind. Eng. Chem.* **2005**, *11*, 400–406.

[5] Kim, K.; Lee, H. S.; Yu, H. D.; Park, H. K.; Kim, N. H. *Colloids Surf., A* **2008**, *316*, 1–7.

[6] Ershov, B. G.; Henglein, A. *J. Phys. Chem. B* **1998**, *102*, 10663– 10666.

[7] Ershov, B. G.; Henglein, A. *J. Phys. Chem. B* **1998**, *102*, 10667–10671.

[8] Huber, K.; Witte, T.; Hollmann, J.; Keuker-Baumann, S. *J. Am. Chem. Soc.* **2007**, *129*, 1089–1094.

[9] Zhang, Z.; Patel, R. C.; Kothari, R.; Johnson, C. P.; Friberg, S. E.; Aikens, P. A. *J. Phys. Chem. B* **2000**, *104*, 1176–1182.

[10] Chu, B.; Liu, T. *J. Nanopart. Res.* **2000**, *1*, 29–41.

[11] Remita, S.; Fontaine, P.; Lacaze, E.; Borensztein, Y.; Sellame, H.; Farha, R.; Rochas, C.; Goldmann, M. *Nucl. Instrum. Methods B* **2007**, *263*, 436–440.

[12] Korgel, B. A.; Fitzmaurice, D. *Phys. Rev. B* **1999**, *59*, 14191–14201.

[13] Sui, Z. M.; Chen, X.; Wang, L. Y.; Xu, L. M.; Zhuang, W. C.; Chai, Y. C.; Yang, C. J. *Physica E* **2006**, *33*, 308–314.

[14] Patakfalvi., R.; Oszko, A.; Dekany, I. *Colloids Surf., A* **2003**, *220*, 45–54.

[15] Patakfalvi, R.; Dekany, I. *Appl. Clay Sci.* **2004**, *25*, 149–159.

[16] Wang, W.; Efrima, S.; Regev, O. *J. Phys. Chem. B* **1999**, *103*, 5613–5621.

[17] Lee, H. J.; Yeo, S. Y.; Jeong, S. H. *J. Mater. Sci.* **2003**, *38*, 2199–2204.
[18] Bozzi, A.; Yuranova, T.; Kiwi, J. *J. Photochem. Photobiol., A* **2005**, *172*, 27–34.
[19] Ye, W. J.; Leung, M. F.; Xin, J.; Kwong, T. L.; Lee, D. K. L.; Li, P. *Polymer* **2005**, *46*, 10538–10543.
[20] Richardson, M. J.; Johnston, J. H. *J. Colloid Interface Sci.* **2007**, *310*, 425–430.
[21] Brzezinski, S.; Jasiorski, M.; Maruszewski, K.; Ornat, M.; Malinowska, G.; Borak, B.; Karbownik, I. *Polymer* **2007**, *52*, 362–366.
[22] Lo Nostro, P.; Fratoni, L.; Baglioni, P. *J. Inclusion Phenom. Macrocyclic Chem.* **2002**, *44*, 423–427.
[23] Lo Nostro, P.; Corrieri, D.; Ceccato, M.; Baglioni, P. *J. Colloid Interface Sci.* **2001**, *236*, 270–281.
[24] Scalia, S.; Tursilli, R.; Bianchi, A.; Lo Nostro, P.; Bocci, E.; Ridi, F.; Baglioni, P. *Int. J. Pharm.* **2006**, *308*, 155–159.
[25] Becheri, A.; Dürr, M.; Lo Nostro, P.; Baglioni, P. *J. Nanopart. Res.* **2008**, *10*, 679–689.
[26] Kong, H.; Jang, J. *Langmuir* **2008**, *24*, 2051–2056.
[27] Panacek, A.; Kvitek, L.; Prucek, R.; Kolar, M.; Vecerova, R.; Pizurova, N.; Sharma, V. K.; Nevecna, T.; Zboril, R. *J. Phys. Chem. B* **2006**, *110*, 16248–16253.
[28] Baker, C.; Pradhan, A.; Pakstis, L.; Pochan, D. J.; Shah, S. I. *J. Nanosci. Nanotechnol.* **2005**, *5*, 244–249.
[29] In his "Histories" (5th Century B.C.), Herodotus of Halicarnassus reported on the war expeditions of Cyrus, King of Persia: "Wherever he (Cyrus) travels, he is attended by a number of four-wheeled cars drawn by mules, in which the Choaspes water, ready boiled for use and stored in flagons of silver, is moved with him from place to place".
[30] Furno, F.; Morley, K. S.; Wong, B.; Sharp, B. L.; Arnold, P. L.; Howdle, S. M.; Bayston, R.; Brown, P. D.; Winship, P. D.; Reid, H. J. *J. Antimicrob. Chemother.* **2004**, *54*, 1019–1024.
[31] Gosheger, G.; Hardes, J.; Ahrens, H.; Streitburger, A.; Buerger, H.; Erren, M.; Gunsel, A.; Kemper, F. H.;

Winkelmann, W.; von Eiff, C. *Biomaterials* **2004**, *25*, 5547–5556.
[32] Rupp, M. E.; Fitzgerald, T.; Marion, N.; Helget, V.; Puumala, S.; Anderson, J. R.; Fey, P. D. *Am. J. Infection Control* **2004**, *32*, 445–450.
[33] Samuel, U.; Guggenbichler, J. P. *Int. J. Antimicrob. Agents* **2004**, *23*, S75–S78.
[34] Strathmann, M.; Wingender, J. *Int. J. Antimicrob. Agents* **2004**, *24*, 234–240.
[35] Ohashi, S.; Saku, S.; Yamamoto, K. *J. Oral Rehabil.* **2004**, *31*, 364–367.
[36] Ulkur, E.; Oncul, O.; Karagoz, H.; Yeniz, E.; Celikoz, B. *Burns* **2005**, *9*, 874–877.
[37] Parikh, D. V.; Fink, T.; Rajasekharan, K.; Sachinvala, N. D.; Sawhney, A. P. S.; Calamari, T. A.; Parikh, A. D. *Textile Res. J.* **2005**, *75*, 134–138.
[38] Gauger, A.; Mempel, M.; Schekatz, A.; Schafer, T.; Ring, J.; Abeck, D. *Dermatology* **2003**, *207*, 15–21.
[39] Lee, D.; Cohen, R. E.; Rubner, M. F. *Langmuir* **2005**, *21*, 9651–9659.
[40] Soulsby, E. J. *BMJ* **2005**, *331*, 1219–1220.
[41] Cho, K. H.; Park, J. E.; Osaka, T.; Park, S. G. *Electrochim. Acta* **2005**, *51*, 956–960.
[42] Alt, V.; Bechert, T.; Steinrucke, P.; Wagener, M.; Seidel, P.; Dingeldein, E.; Domann, E.; Schnettler, R. *Biomaterials* **2004**, *25*, 4383–4391.
[43] Morones, J. R.; Elechiguerra, J. L.; Camacho, A.; Holt, K.; Kouri, J. B.; Ramirez, J. T.; Yacaman, M. J. *Nanotechnology* **2005**, *16*, 2346–2353.
[44] Yuranova, T.; Rincon, A. G.; Pulgarin, C.; Laub, D.; Xantopoulos, N.; Mathieu, H.-J.; Kiwi, J. *J. Photochem. Photobiol., A* **2006**, *181*, 363–369.
[45] Cho, J. W.; So, J. H. *Mater. Lett.* **2006**, *60*, 2653–2656.
[46] Dubas, S. T.; Kumlangdudsana, P.; Potiyaraj, P. *Colloids Surf., A* **2006**, *289*, 105–109.
[47] Vigneshwaran, N.; Kathe, A. A.; Varadarajan, P. V.; Nachane, R. P.; Balasubramanya, R. H. *J. Nanosci. Nanotechnol.* **2007**, *7*, 1893–1897.

[48] Blanton, T.; Huang, T. C.; Toraya, H.; Hubbard, C. R.; Robie, S. B.; Louer, D.; Gobel, H. E.; Will, G.; Gilles, R.; Raftery, T. *Powder Diffr.* **1995**, *10*, 91–95.
[49] Guinier, A.; Fournet, G. *Small-Angle Scattering of X-Rays*; Wiley: New York, 1955.
[50] Bartlett, P.; Ottewill, R. H. *J. Chem. Phys.* **1992**, *96*, 3306–3318.
[51] Kotlarchyk, M.; Chen, S.-H. *J. Chem. Phys.* **1983**, *79*, 2461–2469.
[52] Hayter, J. B. *Physics of Amphiphiles: Micelles, Vescicles and Microemulsions*; Degiorgio, V., Corti, M., Eds.; North-Holland: Amsterdam, The Netherlands, 1983.

3. Tunable Gold Nanostructures

3.1 Introduction

AuNPs, which have been known for 2500 years, are the subject of an exponentially increasing number of reports and are full of promises for optical, electronic, magnetic, catalytic, and biomedical applications. The reasons for the present extensive efforts in AuNP research are the stability of AuNPs, the extraordinary diversity of their modes of preparations (including biosynthetic modes and template synthesis) involving ceramics, glasses, polymers, ligands, surfaces, films, oxides, zeolithes, biomolecules, and bioorganisms, and their essential properties and role in nanoscience and future nanotechnology [1].

The classic Turkevitch-Frens synthesis [2,3] with citrate stabilizer is practical and still very much used to prepare precursors. However, the stabilization of AuNPs by alkanethiolate and various functional thiolate ligands forming very stable, relatively monodisperse materials and the two-phase Schiffrin synthesis [4] have been a breakthrough. These facile syntheses have been shown to be particularly favorable for easy manipulations, such as place-exchange reactions and extensive physical characterizations, formation of superlattices and crystals, and rich molecular chemistry. For instance, multiple redox states (up to 15) of AuNP-alkanethiolate were characterized at room temperature as charge injection in the core is quantized, and 2D and 3D Au NP superlattices are now common, easily controlled assemblies that use supramolecular principles and are characterized by spectacular imaging and microscopy techniques.

Fascinating aspects are the optoelectronic properties of AuNPs related to the surface plasmon absorption, reflecting the collective oscillation of the conducting electrons of the gold core, a feature relevant to the quantum size effect. Non-Linear-Optic applications of Au NPs are also rapidly growing. The combination of this photonics discipline with

biology and medicine has already been demonstrated by the work on Au NP-DNA assemblies and is very promising for future biomolecular manipulations and applications, such as labeling, detection, and transfer of drugs, including genetic materials.

Electronic conduction correlated with single-electron tunneling is a possible basis for future nanoelectronic digital circuits in connection with selfassembled monolayers, although the quantized capacitance involved will require ultrapure Au NP materials.

Excellent sensory and environmental devices are becoming available by tuning the spectroscopy, fluorescence, luminescence, and electrochemical characteristics of Au NPs with those of substrates including DNA, sugars, and other biological molecules or systems.

Another promising electrochemical field that has just started to develop is that of Au NP ultramicroelectrodes. Thus, it is becoming possible to control molecules at a resolution well below that offered by photolithography. In particular, DNA is a candidate for this task because of its excellent specificity in base pairing, and it can be easily addressed at the nanoscale for applications in biosensing and bionanotechnology.

Finally, although bulk gold is well known for being inert, the reactivity of the gold cores in Au NPs has recently proven very useful in catalytic applications, even at subambient temperatures, and the field of Au NP-catalyzed CO and methanol oxidation and O_2 reduction is now also developing at a rapid rate. Here again, the variety of synthetic possibilities using Au NP components and the understanding of the Au NP nanostructures and their role on the catalytic events is a key toward future applications.

An extraordinary variety of structures, properties, and applications is available for Au NPs and will motivate fundamental studies and applications in connection with those of other molecular, inorganic, and biological nanomaterial components in interdisciplinary research involving chemistry, physics, biology, and medicine [1].

3.2. Synthesis and Assembly

3.2.1. Citrate Reduction

Among the conventional methods of synthesis of AuNPs by reduction of gold(III) derivatives, the most popular one for a long time has been the use of citrate reduction of $HAuCl_4$ in water. This synthesis was introduced by Turkevitch in 1951 [2] and leads to AuNPs of ca. 20 nm. In 1973, Frens et al. [3] reported a method to obtain AuNPs of a given size (16-147 nm) where the trisodium citrate to gold ratio was varied. This method is very often used even now when a rather loose shell of ligands is required around the gold core in order to prepare a precursor to valuable AuNP-based materials. Recently, a practical preparation of sodium 3-mercaptopropionate-stabilized AuNPs was reported in which simultaneous addition of citrate salt and an amphiphile surfactant was adopted; the size could be controlled by varying the stabilizer/gold ratio [5].

3.2.2. The Brust-Schiffrin Method: Two-Phase Synthesis and Stabilization by Thiols

Despite its delicate synthesis [6], Schmid's cluster $[Au_{55}(PPh_3)_{12}Cl_6]$, remained unique for long time since 1981 due to its narrow dispersity (1.4 ± 0.4 nm) and its application in the study of a quantum-dot nanomaterial. The stabilization of AuNPs with alkanethiols was first reported in 1993 by Mulvaney and Giersig, who showed the possibility of using thiols of different chain lengths [7]. The Brust-Schiffrin method for AuNP synthesis, published in 1994, had a considerable impact on the overall field in less than a decade, because it allowed for the first time the facile synthesis of thermally stable and air-stable AuNPs of reduced polydispersity and controlled size (ranging in diameter between 1.5 and 5.2 nm). Indeed, these AuNPs can be repeatedly isolated and redissolved in common organic solvents without irreversible aggregation or decomposition, and they can be easily handled and functionalized just as

stable organic and molecular compounds. The technique of synthesis is inspired by Faraday's two-phase system [8] and uses the thiol ligands that strongly bind gold due to the soft character of both Au and S [4,9]. $AuCl_4^-$ is transferred to toluene using tetraoctylammonium bromide as the phase-transfer reagent and reduced by $NaBH_4$ in the presence of dodecanethiol (Figure 3.1) [4].

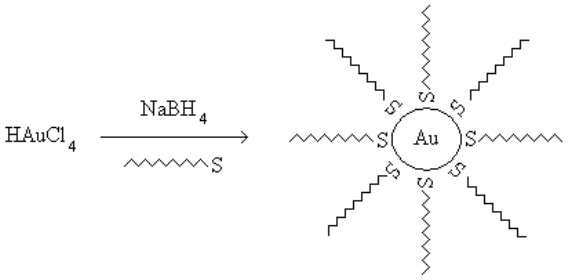

Figure 3.1. Formation of AuNPs coated with organic shells by reduction of Au(III) compounds in the presence of thiols.

The organic phase changes color from orange to deep brown within a few seconds upon addition of $NaBH_4$:

$$AuCl_4^-{}_{(aq)} + N(C_8H_{17})_4^+{}_{(C_6H_5Me)} \rightarrow N(C_8H_{17})_4^+AuCl_4^-{}_{(C_6H_5Me)}$$

$$m AuCl_4^-{}_{(C_6H_5Me)} + n C_{12}H_{25}SH_{(C_6H_5Me)} + 3m e^- \rightarrow 4m\ Cl^-{}_{(aq)} + [Au_m(C_{12}H_{25}SH)_n]_{(C_6H_5Me)}$$

The TEM photographs showed that the diameters were in the range 1-3 nm, with a maximum in the particle size distribution at 2.0-2.5 nm, with a preponderance of cuboctahedral and icosahedral structures. Larger thiol/gold mole ratios give smaller average core sizes, and fast reductant addition and cooled solutions produced smaller, more monodisperse particles. A higher abundance of small core sizes ($\leq$ 2 nm) is obtained by quenching the reaction immediately following reduction or by using sterically bulky ligands [10-14]. Brust et al. extended this synthesis to *p*-mercaptophenol-stabilized AuNPs in a single phase system

[9] which opened new routes to the synthesis of AuNPs stabilized by a variety of functional thiol ligands [4,9-11]. Subsequently, many publications appeared describing the use of the Brust- Schiffrin procedure for the synthesis of other stable AuNPs, as for example the so-called monolayer-protected clusters (MPCs) that contained functional thiols [12-17]. The proportion thiol:$AuCl_4^-$ used in the synthesis controls the size of the AuNPs (for instance, a 1:6 ratio leads to the maximum average core diameter of 5.2 nm, i.e., ca. 2951 Au atoms and ca. 371 thiolate ligands; core diameter dispersity of ~±10%). Murray et al. reported and studied the "place exchange" of a controlled proportion of thiol ligands by various functional thiols [16] (Figure 3.2) and the subsequent reactions of these functional AuNPs [14,16]. Schiffrin reported the purification of dodecanethiol-stabilized AuNPs from tetraoctylammonium impurities by Soxhlet extraction [18]. The influence of nonionic surfactant polyoxoethylene(20) sorbitan monolaurate (Tween 20) on surface modification of AuNPs was studied with mercaptoalkanoic acids [19]. Digestive ripening, i.e., heating a colloidal suspension near the boiling point in the presence of alkanethiols (for instance, 138 °C for 2 min, followed by 5 h at 110 °C), significantly reduced the average particle size and polydispersity in a convenient and efficient way. This technique also led to the formation of 2D and 3D superlattices [20,21], a subject of intense investigation [22-33]. For instance, AuNPs obtained using acid-facilitated transfer are free of tetraalkylammonium impurity, are remarkably monodisperse, and form crystalline superstructures [31]. The truncated icosahedron structure is formed in growth conditions in which the equilibrium shape is achieved [32]. Molecular dynamics simulations showed that AuNPs with 1157 Au atoms attained an icosahedral structure upon freezing [33]. A single-toluene phase method was also reported whereby the ammonium salt-stabilized AuNPs were synthesized, followed by an exchange reaction with dodecanethiol [22,23]. Superhydride [34] and hexadecylaniline [35] have been used as alternative reagents to $NaBH_4$ for the reduction of gold(III) in the synthesis of thiol-stabilized AuNPs. Shape separation of suspended

AuNPs by size-exclusion chromatography was monitored by examining the 3D chromatograms obtained by employing a diode-array detection system [36].

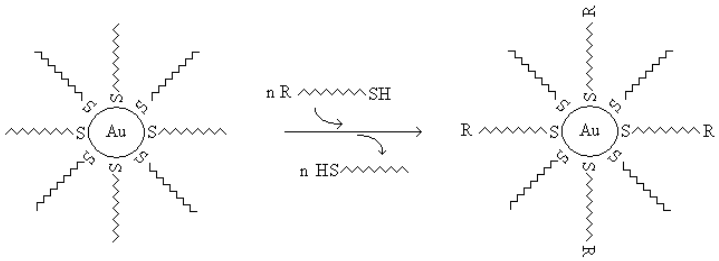

Figure 3.2. General scheme for the ligand-exchange reaction between alkanethiol-AuNPs of the Brust type and various functionalized thiols [16].

3.3. Gold nanoparticles and polymers composites

Since the report in Helcher's treatise in 1718 [38] indicating that starch stabilizes water-soluble gold particles, it has been known that such materials, recognized two centuries later as polymers, favor the isolation of AuNPs [39,40]. With the considerably improved recent understanding of the parameters leading to the stabilization of AuNPs and of their quantum- size-related interest, there has been a revival of activity in the field of polymer-stabilized AuNPs [41-43]. The most commonly used polymers for the stabilization of AuNPs are PVP and poly-(ethylene glycol) [3,449].

Although there are a variety of ways to achieve nanoparticle-polymer composites [45,46] two different approaches dominate. The first one consists of the in situ synthesis of the nanoparticles in the polymer matrix either by reduction of the metal salts dissolved in that matrix [47] or by evaporation of the metals on the heated polymer surface [48]. The second one, less frequently used, involves polymerization of the matrix around the nanoparticles [49,50]. Recently, however, blending of *pre*-made AuNPs into a *pre*-synthesized polystyrene polymer (synthesized by anionic polymerization) bound to a thiol group was also reported [51]. While the physical process involving mechanical crushing or

pulverization of bulk metals and arc discharge yielded large nanoparticles with a wide size distribution, nanoparticles prepared by reduction of metal salts are small, with a narrow size distribution. This reduction process most often uses a reagent such as $NaBH_4$ [52] which is added in situ, or the reductant can also be the solvent, such as an alcohol [53,54]. For instance, $HAuCl_4 \cdot 4H_2O$ gives stable AuNPs upon refluxing in methanol/water in the presence of PVP, even if NaOH is added subsequently to the preparation of the AuNPs [55]. In poly(acrylamide), $AuCl_4^-$ cannot be reduced by alcohol, but it can be reduced by $NaBH_4$ [56]. Other reductants are generated involving radiolysis, photolysis [57], or electrochemistry [58]. The polymer-nanoparticle composite can be generated from solution (the classic mode) or can involve the immobilization by a solid polymer such as poly(acrylic acid), poly(vinyl alcohol), or PVP. Reduction of metal ions in the presence of the polymer is most often chosen because the complexation of the metal cations by the ligand atoms of the polymer is crucial before reduction. In particular, it dramatically limits the particle size [59].

The most important role of the stabilizing polymer is to protect the nanoparticles from coagulation. Toshima has expressed this function quantitatively by the "gold number", i.e. the number of milligrams of protective polymer that just prevents 10 mL of a red gold sol from changing color to violet upon addition of 1 mL of 10% aqueous NaCl. The "gold number" is smaller for protective polymers that are better stabilizers [53]. Core-shell PVP-stabilized Au@Pd [60,61] and Au@Pt [62,63] nanoparticles were prepared by Yonezawa and Toshima by simultaneous alcohol reduction of the two corresponding metal salts and characterized by EXAFS. The relative order of reduction in alcohol/water is seemingly controlled by the relative redox potentials, $HAuCl_4$ being reduced more rapidly than $Pd(OH)_2$ and $PtCl_6^{2-}$. The AuNPs form first, and then the Pd or Pt shell forms around the AuNPs to produce the core-shell bimetallic particles. In fact, the Pd^0 formed reduces $AuCl_4^-$ to Au^0 and thus acts as a mediator or redox catalyst for the reduction of $AuCl_4^-$, as long as any $AuCl_4^-$ is left in the solution [64,65]. Attempts to synthesize Pd-core/Au shell bimetallic particles led instead to

a remarkable cluster-in-cluster structure because of this redox priority.

Many ordered polymer-AuNPs are known. For instance, AuNPs in PVP were prepared by hydrazine reduction of incorporated $HAuCl_4$. The color of the solution of $HAuCl_4^-$ loaded block copolymer changed from yellow to purple, and then to bluish upon addition of a large excess of anhydrous hydrazine. The reduction can be stopped by addition of HCl, which protonates hydrazine in order to avoid coagulation of the AuNPs [67,68]. These phenomena were also obtained with (styrene-*block*-ethylene oxide) [69,70].

The use of a diaminotriazine-functionalized diblock copolymer led to size-controlled synthesis of AuNP aggregates in solution and in thin films with thymine functionality [71]. AuNPs were generated in polymeric micelles composed of amphiphilic block copolymers [72,73] and amphilic star-block copolymers both an ideal choice to serve as a confined reaction vessel [74]. The formation of AuNPs was also controlled by using poly(methylphosphazene), whose lone pairs stabilized the AuNPs [75]. Functionalized polymers have also been used as stabilizers. Poly(ethylene glycol)-based polymer was used to fabricate an AuNP sensor that reversibly binds lectin for recognition and bioassay [76]. The so-called "grafting from" technique has been used to construct highly dense polymer brushes. For instance, several methods [77-79] including the efficient living radical polymerization (LRP), have indeed been applied to the synthesis of AuNPs coated with such a high-density polymer brush. AuNP-based nanoscale architectures could be forecasted using this simple technique (Figure 3.3) [79].

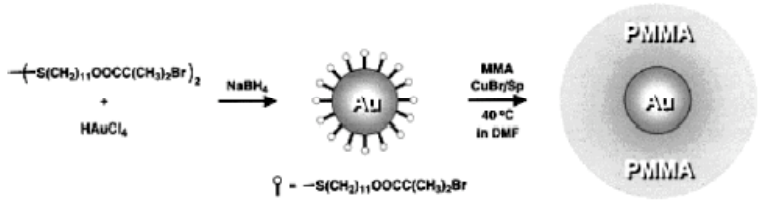

Figure 3.3. Schematic representation for the synthesis of polymer-coated AuNPs by surface-initiated living-radical polymerization (LRP) [79].

Polymer hollow spheres have been synthesized with movable AuNPs at their interiors [80] (Figure 3.4). AuNPs can serve as templates for the synthesis of conductive capsules [81-83] and for the oligomerization of L-cysteine in aqueous solution [84].

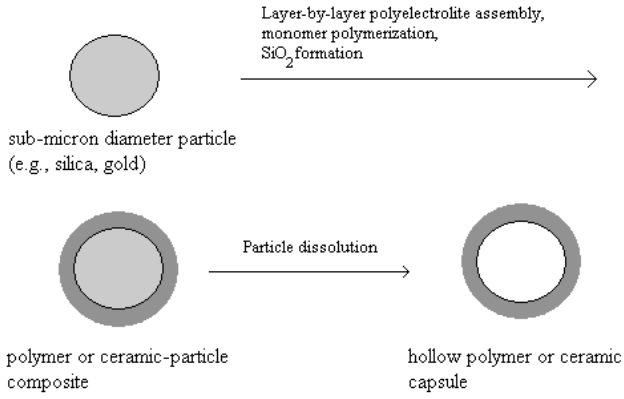

Figure 3.4. AuNPs as templates for the synthesis of hollow polymer capsules [83].

Nanosized domains of block copolymers can be used as nanoreactors to synthesize AuNPs by expansion of the nanosized domains and period of block copolymers, such as polystyrene-*block*-poly(4-vinylpyridine) (PS-PVP) diblock copolymers [85]. Self-assemblies of AuNPs/polymer multilayer films have been formed using surface functionalization [86,87]. AuNPs of average size between 1 and 50 nm have also been stabilized by many water-soluble polymers, and some of them have been shown to be stable after 9 months in air. The most stable ones were obtained with polymers possessing hydrophobic backbones and side groups, allowing good interactions with the $AuCl_4^-$ ion. The preparations were carried out using either UV irradiation or KBH_4 to reduce $HAuCl_4$ in the presence of a mass ratio of polymer:gold 25:1 [88].
Linear polymers having cyano or mercapto groups stabilize AuNPs of 1.5-3 nm diameter and narrow size distributions [89]. AuNPs of Brust type with some thiol chain termini

bearing *exo*-norbornene units were polymerized using ring-opening metathesis polymerization (ROMP) to produce a block copolymer shell [90,91]. Small AuNPs (5 nm diameter) stabilized with sodium citrate [92] were attached to the surface of silica nanoparticles protected by polymer layers to provide contrast in the final TEM image, a strategy also used to obtain TEM contrast for many types of molecular and biological materials [93]. Networks of AuNPs prepared in water were observed by TEM upon adding poly(acrylic acid) to AuNPs stabilized by thiolated poly(ethylene oxide) chains of high molecular weight (necessary to stabilize AuNPs in water). Moreover, thin and linear thermally robust arrangements were formed when chondroitin sulfate c sodium salt (a polysaccharide carrying sulfuric acid groups and carboxylic acid groups) was added [94]. AuNPs of about 20 nm size were formed upon reduction of $AuCl_3$ by polyaniline in *N*-methylpyrrolidinone [95]. An aminefunctionalized polymer was used to simultaneously assemble carboxylic-acid-functionalized AuNPs and silica naoparticles into extended aggregates [96]. Such a strategy also led to spherical silica templates [93]. Macroporous Au spheres with a diameter ~9 μm have been formed by employing porous organic bead templates and preformed AuNPs [97]. AuNPs were stabilized by the lone nitrogen pair on the backbone of polymethylphosphazene, $[Me(Ph)\text{-}PN]_n$, and varying the ratio of $[Me(Ph)PN]_n$ to $HAuCl_4$ prior to reduction allowed control of the AuNP size [98]. AuNPs (4-12 nm) were associated with thiol-functionalized polyoxometalates γ-$[SiW_{10}O_{36}(RSi)O]^{4-}$ ($R = HSC_3H_6$), where the R group played the role of both stabilizing the AuNPs via the thiolate ligand and forming a covalent link to the polyanion through the trimethoxysilane group [99,100]. The preparation of poly-(*N*-isopropylacrylamide)-protected AuNPs has been carried out in a homogeneous phase using various methods, and this polymer was found to be a better passivant than alkanethiols [101].

AuNPs were prepared in both aqueous and organic systems by reducing $HAuCl_4$ with *o*-anisidine in the presence of 1:1 *N*-methyl-2-pyrrolidone/toluene [102]. AuNPs of 6 nm diameter and narrow size distributions were stabilized by π-

conjugated poly(dithiafulvene) polymers, and the oxidized form of this polymer induced a strong red shift of the absorption spectrum of the AuNPs to 550 nm (whereas the theory predicts 510-515 nm for the plasmon band in water) [103]. AuNPs with improved stability against long-term aggregation up to one month were prepared using poly(styrene)-*block*-poly(2-vinylpyridine) star-block copolymer [104].

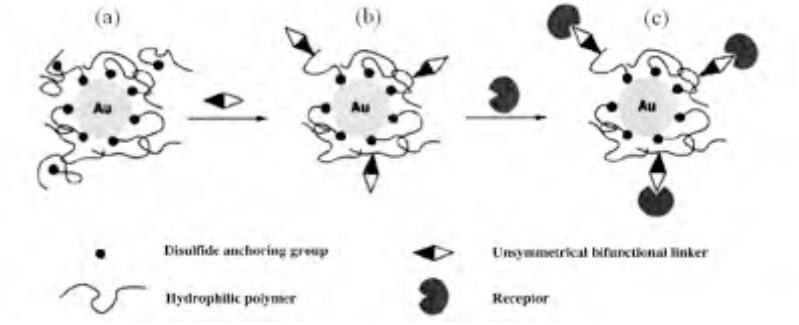

Figure 3.5. Stepwise "grafting-to" derivatization of AuNPs. (a) Fixation of the polymer with disulfide anchoring groups. (b) Activation of the polymer by unsymmetrical bifunctional linker groups. (c) Functionalization of the polymer by receptors. Step (b) is omitted when "activated" polymers are used [105].

Water-soluble polymer-stabilized AuNPs were prepared from citrate-capped AuNPs by simple contact with dilute aqueous solutions of hydrophilic nonionic polymers based on the monomers *N*-[tris(hydroxymethy) methyl]acrylamide and *N*-(isopropyl)acrylamide that were functionalized with disulfide anchoring groups. The resulting polymer-coated AuNPs could be stored in the dry state and redispersed in water to yield sterically stabilized AuNP suspensions. The disulfide-bearing polymers exhibited only a slightly larger affinity for the gold surface than those that do not have the disulfide groups. The polymer layers allowed the free diffusion of small solutes but efficiently minimized the nonspecific absorption of large molecules such as proteins, a promising property (Figure 3.5) [105]. AuNPs have been synthesized in graft copolymer micelles and the diffusion of AuNPs in a

polymer matrix has been analyzed [106]. Core-shell AuNPs have been prepared by the layer-by- layer technique, utilizing polyelectrolyte multilayers assembled onto polystyrene cores as thin films in which to infiltrate AuNPs, and hollow spheres were obtained by removal of the templated polystyrene cores [107].

3.4. A tri-block copolymer templated synthesis of gold nanostructures [108]

3.4.1. Introduction

Several polymeric stabilizers have been designed for size-controlled synthesis of monodisperse gold nanoparticles in water; among these, poly(methylmethacrylate) (PMMA) has shown a good templating ability [109-111]. Moreover, many researches have been focused on the synthesis of amphiphilic polymers incorporating inorganic nanoparticles [112-117] and several studies report the ability of block copolymers to act as templating agents for the synthesis of gold nanoparticle [118]. Many block copolymers can form micellar structure, thus acting as nanoreactors for the synthesis of metallic nanoparticles [119,120] and several reduction methods have been proposed for gold precursors: from photoreduction using UV irradiation [120,121] to chemical reduction [118,122].

Therefore a tri-block copolymer consisting of methacrylic acid and poly(ethylen glycol) methacrylate has been synthesized and used as templating agent for the synthesis of gold nanoparticles. The polymer (BMB) has been synthesized by RAFT polymerization and consists of two PEG-methylacrylate chains (B blocks) anchored to a poly(methacrylic) moiety containing a trithiocarbonate unit (M block).

The synthesis has been performed at the polymer native pH because recent studies [123] revealed that at this pH it has the best conformation for our purpos. In fact, for pH values higher than 5.5 the methacrylic moiety undergoes full deprotonation and acquires a more hydrophilic character whose consequence is a coiling of the polymer into a micellar structure with the ionized block pulled outside the unimolecular aggregate and the PEG chains arranged in the core while at pH values lower than 5.5 the two moieties are equally arranged in the space, so that both PEG and

methacrylic moieties can be available to both template and stabilize the nanosol.
Since the ratio between gold precursor and polymer is a critical parameter to control the particle size [124-135], different Au/polymer ratios have been explored in order to find the best synthetic conditions to both synthesize and stabilize ultra-small gold nanoparticles. The samples have been characterized by means of UV-Visible Absorption, Small Angle X-Ray Scattering (SAXS), Atomic Force Microscopy (AFM) and Transmission Electron Microscopy (TEM).

3.4.2. Experimental section

$HAuCl_4 \cdot 3H_2O$ was purchased from Sigma-Aldrich, $NaBH_4$ and the monomers used for the synthesis were purchased from Aldrich Chemicals (Milan, Italy). Methacrylic acid (MAA) was distilled at reduced pressure and the fraction boiling at 65°C was used. Oligo(ethylene glycol) methylether methacrylate M_n = 475 Da (OEGMA, d = 1,08 g/ml at 25°C) and the initiator 4,4'-azobis(4-cyanopentanoic acid) (V-501) were purchased from Aldrich and used without further purifications.
The RAFT chain transfer agent (CTA) S,S'-bis(α,α'-dimethyl-α''-acetic acid) trithiocarbonate was synthesized according to the procedure reported by Lai et al. [136]. All the solvents were reagent grade and were used without further purification, HPLC-grade water was used for the polymerization while for the nanoparticles' synthesis water purified with a Millipore system (resistivity 18 MΩ·cm) has been employed.

Copolymer Synthesis. The RAFT synthesis of the poly(OEGMA-b-MAA-b-OEGMA) BMB-type three block copolymer of methacrylic acid (M block) and oligo(ethylene glycol) methylether methacrylate (B block) was carried out by polymerizing sequentially the two monomers, starting with OEGMA, and using S,S'-bis(α,α'-dimethyl-α''-acetic

acid) trithiocarbonate as the RAFT agent of the controlled free radical process.

A round bottomed flask was loaded with water (100 ml), OEGMA (8 g, $1.68 \cdot 10^{-3}$ mol), CTA (0.45, $1.6 \cdot 10^{-3}$ mol) and purged 30 min with N_2. The reaction mixture was heated to 70°C with a thermostated oil bath, under nitrogen atmosphere and magnetic stirring, and the V-501 (15 mg, $5.3 \cdot 10^{-5}$ mol) initiator was added to start the polymerization. The reaction was interrupted after 3 h by cooling down the reactor to room temperature.

The polyOEGMA homopolymer and RAFT macrotrasfer agent for the subsequent block copolymerization was purified from unreacted monomer by dialysis against water (membrane cutoff = 2kDa). After the purification the residual content of OEGMA monomer was below 2% as determined by ^{1}H-NMR.

Size exclusion chromatography (SEC) analysis was performed using two Ultrahydrogel Linear columns with a guard precolumn and an aqueous buffer ($NaHCO_3$ 0.05 M, $NaNO_3$ 0.1M, triethanolamine 0.02 M, NaN_3 0.03%) as eluent to determine molecular weight and polydispersity index I_d. A set of poly(ethylene oxide) standards (400; 1000, 4000; 8000; 12000; 20000; 40000 Da) was used for column calibration. The theoretical and experimental values are reported in Table 3.1.

The procedure for the second step of the synthesis of the block copolymer is analogous to the first one. The main difference is the polyOEGMA macrotransfer agent (8 g) that is used, instead of the CTA, to polymerize methacrylic acid (10 g, 0.12 mol) with V-501 (15 mg, $5.3 \cdot 10^{-5}$ mol) initiator.

The synthesized BMB copolymer was lyophilized and purified by extraction in soxhlet for 12 h with $CHCl_3$.

After this procedure only some traces of residual acid monomer could be detected by ^{1}H-NMR.

In Table 3.1 the values of the molecular weights and polydispersity index, as determined by SEC, of the copolymer are reported. The copolymer structure is shown in Figure 3.6.

Table 3.1. Calculated molecular weights ($M_{n,theor}$), experimental molecular weights (number average molecular weight, $M_{n,exp}$, and weight average molecular weight, $M_{w,exp}$) as determined by GPC, polydispersity index (I_d=$M_{w,exp}$/$M_{n,exp}$) and polymerization degree (PD = $M_{n,exp}$/M_{mono}).

	$M_{n,theor}$ (g/mol)	$M_{n,exp}$ (g/mol)	$M_{w,exp}$ (g/mol)	I_d	PD
B blocks	4700	3100	4600	1.5	7
BMB	11700	8100	11000	1.4	/
M block	7000	5000	6400	/	56

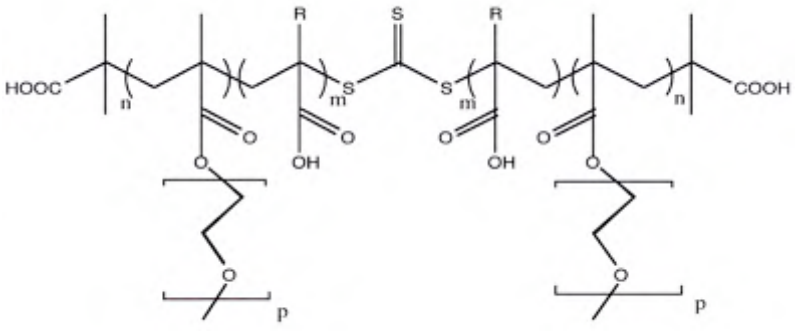

Figure 3.6. Structure of the tri-block copolymer; R= CH_3, n= 3-4, m= 28, p= 8.

Nanoparticles' Synthesis. Gold nanoparticles were prepared from $HAuCl_4 \cdot 3H_2O$ as gold source material; the reduction was performed in ice-cold water by addition of a proper amount of ice-cold 0.1 M $NaBH_4$. The reductant addition has been performed slowly, with an addition rate of 100 μL/min. The gold precursor concentration was $3 \cdot 10^{-4}$M for all the synthesis. In order to evaluate the influence of the polymer concentration on the final shape and size of the nanostructures, three different gold/polymer molar ratios employed: 10^3, 215 and 4.6 thus leading to three different samples, herein after referred to as sample A, B and C respectively.

SAXS. Small Angle X-Ray Scattering measurements were carried out with a HECUS SWAX-camera (Kratky) equipped with a position-sensitive detector (OED 50M) containing

1024 channels of width 54 μm. Cu K_α radiation of wavelength 1.542 Å was provided by a Seifert ID-3003 X-ray generator (sealed-tube type), operating at a maximum power of 2 kW. A 10 μm thick nickel filter was used to remove the CuK_β radiation. The sample-to-detector distance was 275 mm. The scattering path between the sample and the detector was kept under vacuum (P < 1mBar) during the measurements to minimize scattering from the air. The Kratky camera was calibrated using silver behenate, which is known to have a well-defined lamellar structure (d = 58.48 Å) [124]. Scattering curves were monitored in a Q-range from 0.009 to 0.55 $Å^{-1}$. Q, the scattering vector, is defined as $Q= 4\pi/\lambda \cdot sen\theta/2$, where λ is the wavelength of the scattering radiation and θ is the scattering angle. The liquid samples were filled into 1 mm quartz capillary using a syringe. Measurements were done at 25 °C. The temperature was controlled by a Peltier element, with an accuracy of ±0.1 °C. All scattering curves (slit smeared data) were corrected for the empty cell contribution (quartz capillary) containing water. The data were slit desmeared by linear method [125].

UV-Visible Absorption. Absorbance spectra were collected in the range 400 – 900 nm with a Perkin-Elmer Lambda 900 spectrophotometer for solutions of chemicals.

Atomic Force Microscopy. AFM analysis was carried out with a XE-100E system (PSIA). The images were acquired in Non Contact Mode; a silicon cantilever with tip radius of curvature <5 nm and force constant equal to 42 N/m was used. Samples were deposited on mica by spin-coating.

Transmission Electron Microscopy. TEM analysis was carried out with JEM 3010 (JEOL) electron microscope operating at 300 kV, point to point resolution at Scherzer defocus of 0.17 nm. Specimens for TEM analysis were sonicated in water and then transferred as a suspension to a copper grid covered with a lacey carbon film. The images were collected in bright field mode.

3.4.3. Results and Discussion.

The nanosols obtained from the synthesis are shown in Figure 3.7.

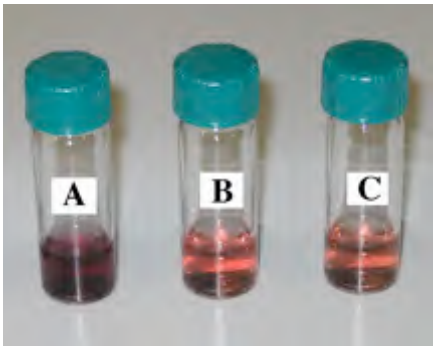

Figure 3.7. Pictures of the nanosols, showing the different colours of the dispersions, reflecting their different Surface Plasmon Resonance behaviour.

UV-Visible spectra show the characteristic Surface Plasmon Resonance typical of metallic nanoparticles [126]. In Figure 3.8 the absorption curves for the investigated samples are reported. UV-Visible spectra have been fitted with Lorentzian curves and a polynomial baseline. The choice of the Lorentzian shape is due to the fact that it is the typical line shape of SPR (Surface Plasmon Resonance) in the classic Mie theory [126], while the baseline has been fitted with a cubic polynomial function because the exponential decay, typical for ultra-small gold clusters with a size range of 1-2 nm [127], does not fit properly. The results of the fitting are also shown in Figure 3.8.

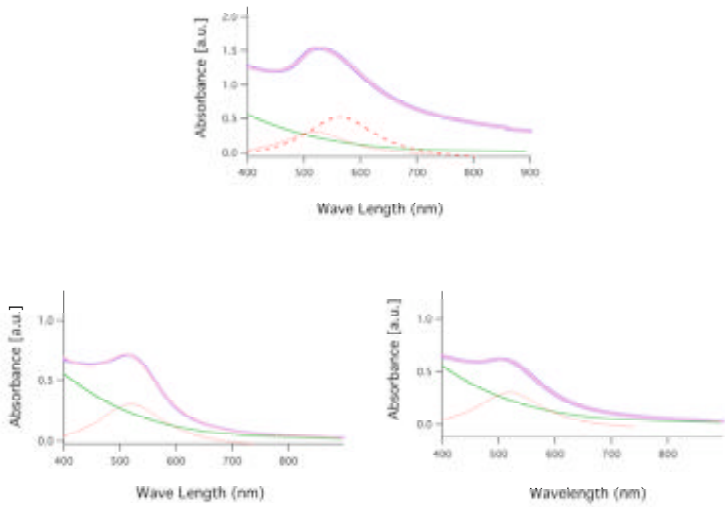

Figure 3.8. UV-Visible spectra of the three investigated samples (top: sample A; bottom: sample B (left) and sample C (right) and corresponding fitting curves.

While for samples B and C one Lorentzian peak is sufficient to fit the experimental absorption curves, for sample A two Lorentzian peaks are required. This suggests that in the latter sample we could have anisotropic particles or two different nanoparticles' populations in solution. This is confirmed by the analysis of TEM data: a comparison of sample A, B and C micrographs (Figures 3.9-3.11) highlights a significant difference between the samples: while B and C micrographs reveal spherical particles, sample A shows a coexistence of some spherical polydisperse particles and elongated structures. The size distribution histograms for B and C samples have Gaussian profiles [128-131], centered at 2.0 nm and 3.4 nm respectively (Figure 3.12). The fitting of the experimental data return a higher polydispersity, p, for sample B (p=0.22) than for sample C (p=0.15). The polydispersity in the case of a Gaussian curve has been defined as σ/r_{avg}.

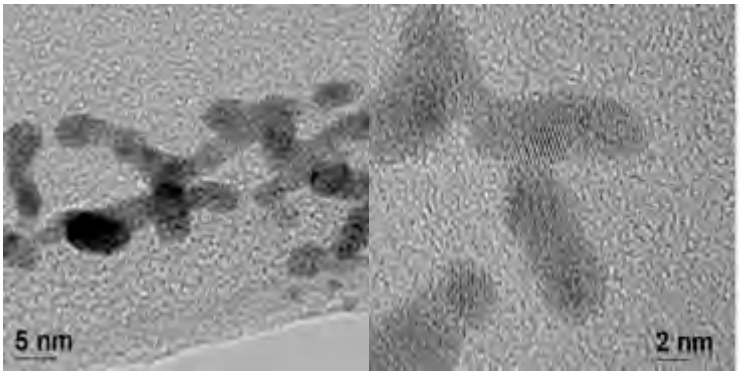

Figure 3.9. Representative TEM micrographs of sample A at 150k (left) and 800k (right) magnification.

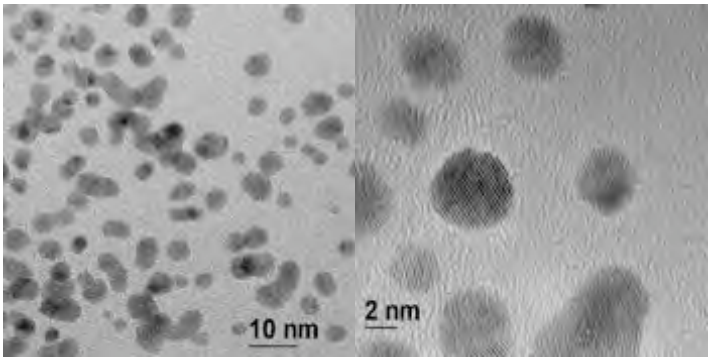

Figure 3.10. Representative TEM micrographs of sample B at 250k (left) and 800k (right) magnification.

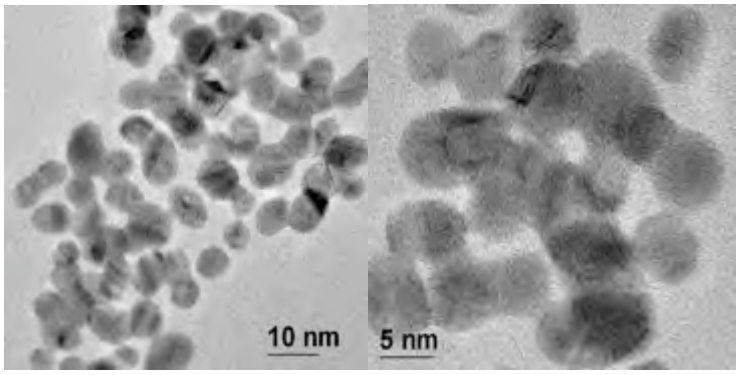

Figure 3.11. Representative TEM micrographs of sample C at 250k (left) and 500k (right) magnification.

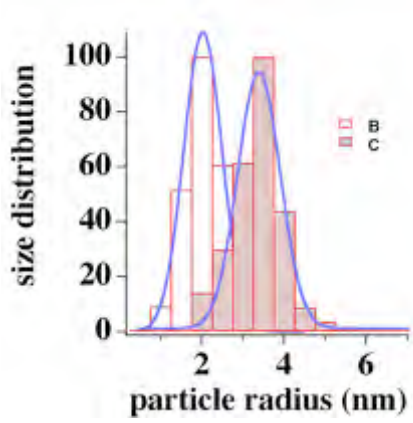

Figure 3.12. Size distribution of samples B and C obtained by the analysis of TEM micrographs and corresponding Gaussian fits.

Even if TEM measurements allow to obtain the particles' size distributions, no information can be deduced about the behaviour of the particles in solution: since TEM samples are obtained by drying few drops of the dispersions on a carbon coated copper grid, some aggregates imaged by this technique could be artefacts due to the drying process. In order to check if the nanobundles observed for sample A are simply due to stacking of more particles or if they are elongated structures produced by the sythethic conditions used, we performed an additional synthesis in order to verify if the polymer content can tune the particles' anisotropy. A gold/polymer molar ratio of $47 \cdot 10^{-3}$M has been used while the other synthetic conditions (gold precursor concentration, reductant addition rate, pH and temperature) have been kept equal to the ones of samples A, B, C. The as-obtained nanosol (sample 0) is stable and the corresponding TEM images are shown in Figure 3.13.

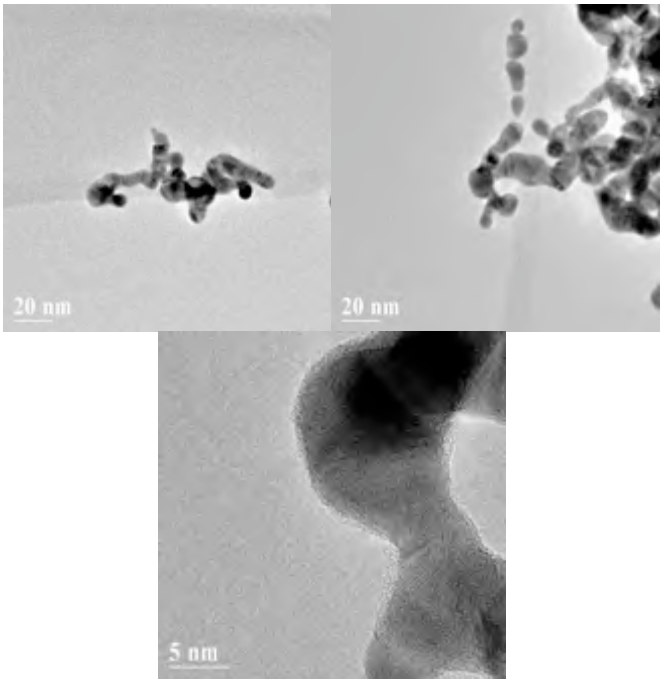

Figure 3.13. Representative TEM micrographs of sample 0 at 100k (left and middle) and 600k (right) magnification.

As clearly shown by Figure 3.13, sample 0 is composed by elongated crystalline structures, with a mean radius varying from 2.5 to 5 nm and a mean length ranging between 7 nm and several tenths of nanometers. Therefore the effect of a lower polymer concentration is reflected in a bigger mean size and higher anisotropy of the gold nanostructures. The bigger size of the ellipsoidal particles can be easily explained considering that a lower templating agent content cannot prevent the growth of the first nuclei formed in solution upon the addition of reductant, thus leading to final bigger objects, while the ellipsoidal shape is probably due to a preferred absorption of the polymer on the nuclei facets during the reduction, thus leading to an increased ellipticity of the final particles. This is clear from the analysis of the particles' shape and anisotropy in the TEM images of samples, where ranging from sample 0 (lower polymer content) to sample C (higher polymer content) the isotropy of the particles significantly increases.

Moreover, both in sample 0 than in sample A compact bundles are observed, but it is not easy to distinguish if they are stacked ellipsoids or bundles of aggregated particles already present in the dispersion, before TEM grid preparation. In order to have a more comprehensive picture of the aggregation behaviour of the particles in solution, Small Angle X-Ray Scattering measurements are required. SAXS is a powerful tool to investigate nanoparticles' size and shape in solution [132,133] and can also give a more statistical information about the sample, since it has access to the whole volume of the sample instead of few drops like with TEM measurements. In this way, possible aggregates not observed by TEM could be revealed. Therefore, samples A, B and C have been concentrated up to 1 mg/mL by diafiltration using Amicon Ultrafiltration System equipped with a regenerated cellulose membrane (MWCO= 10 kDa) in order to have a higher scattering intensity to perform SAXS measurements with respect to the as-synthesized dispersions.

In Figure 3.14 the scattering profiles for sample A, B and C are shown. As far as the scattering pattern is concerned, samples B and C show a similar scattering profile while sample A shows a different trend in the low-Q range. In particular, the analysis of the experimental intensity slope shows a Q^{-1} slope, confirming the previous TEM results, where the presence of elongated structures, responsible for the cylindrical scattering profile, has been revealed. Therefore, SAXS data have been analysed using a cylindrical-like form factor for sample A and a spherical form factor for samples B and C.

In particular, the model used for sample B and C accounts for the scattering of a polydisperse population of spheres with uniform scattering length density and Gaussian size distribution of radii. No structure factors have been included neither in this model, nor in the model used for sample A, due to the low concentration of particles in solution that do not give interparticle interference effects.

Therefore the scattering intensity, given only by the form factor P(Q), is:

$$I(Q) = AN_0P(Q) + bkg \qquad (3.1)$$

and in the case of the spherical form factor used it is:

$$I(Q) = AN_0P(Q) + bkg = \\ = A\left(4\pi/3\right)^2 N_0\Delta\rho^2 \int_0^\infty f(R)R^6F^2(QR)dR + bkg \quad (3.2)$$

where A is an instrumental factor, N_0 is the total number of particles per unit volume, bkg is the incoherent background, $\Delta\rho$ is the difference in scattering length density between the particle and the solvent (ρ_p-ρ_s), f(R) is the Gaussian distribution of radii and F^2(QR) is the scattering amplitude for a sphere:

$$F(QR) = \frac{\left[\sin(QR) - QR\cos(QR)\right]}{(QR)^3} \quad (3.3)$$

$$f(R) = \frac{1}{\sigma\sqrt{2\pi}} \exp - \left[\frac{1}{2\sigma^2}(R - R_{avg})^2\right] \quad (3.4)$$

where R_{avg} is the mean radius of the distribution and σ is the standard deviation.
The model used for sample A includes a form factor for a polydisperse circular cylinder with uniform scattering length density; the polydispersity is included by integrating the form factor, P(Q), over a Schultz distribution of cylinder radius. The integration has been normalized by the second moment of the radius distribution. This insures that the invariant is constant when the polydispersity is varied and all other structural parameters are held fixed. The size averaged form factor is thus:

$$\overline{P(Q)} = \frac{1}{V_{poly}} \int_0^x P(Q) f(R) dR \quad (3.5)$$

where *f(R)* is the normalized Schultz distribution of the radius. The limits of the integration are chosen automatically to cover the full range of the radius. The integral is

normalized to the polydisperse volume using the second moment:

$$V_{poly} = \pi r^2 L\left(\frac{z+2}{z+1}\right) \tag{3.6}$$

P(Q) is the orientation-averaged form factor of a cylinder of total length H and radius r:

$$P(Q) = \frac{\phi}{V_{cyl}} \int_0^{\pi/2} F^2(Q,\alpha)\sin\alpha d\alpha \tag{3.7}$$

where ϕ is the volume fraction and $F(Q,\alpha)$ is the scattering amplitude:

$$F(Q,\alpha) = 2V_{cyl}(\rho_{cyl} - \rho_{solv})\, j_0(QH\cos\alpha)\frac{J_1(QR\sin\alpha)}{(QR\sin\alpha)} \tag{3.8}$$

with $V_{cyl}=\pi r^2 L$ and $j_0(QH\cos\alpha)= \sin(QH\cos\alpha)/(QH\cos\alpha)$ and $J_1(QR\sin\alpha)$ is the first order Bessel function. α is defined as the angle between the cylinder axis and the scattering vector Q. The integral over α averages the form factor over all possible orientations of the cylinder with respect to Q.
The Schultz size distribution is:

$$f(R) = (z+1)^{z+1} x^z \frac{\exp[-(z+1)x]}{R_{avg}\Gamma(z+1)} \tag{3.9}$$

where R_{avg} is the mean radius of the distribution and $x=R/R_{avg}$, z is related to the polydispersity, $p=\sigma/R_{avg}$, by $z=1/p^2-1$. σ^2 is the variance of the size distribution.
No organic shell around the particles has been considered: due to the low contrast between the polymer and the solvent, calculated as $5.4\cdot10^{-6}$ Å^{-2}, the presence of a polymer shell around the gold particles would not be detectable by means of our SAXS experiments. Therefore, we simply modeled the particles as "naked" gold nanoparticles in water. The

theoretical value of scattering length density for bulk gold has been used.
The results of the fitting are shown in Table 3.2 for all the investigated samples.

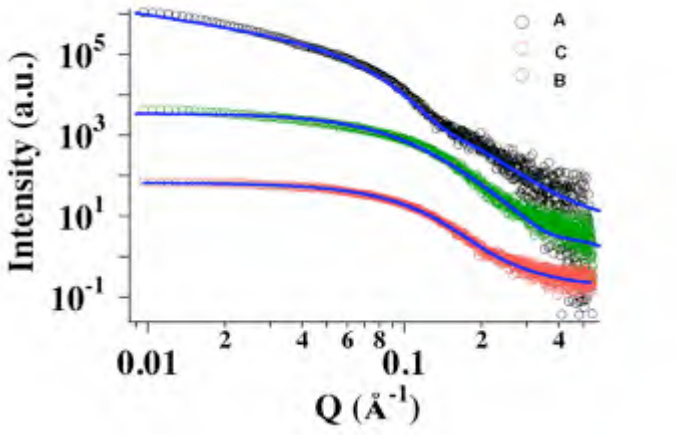

Figure 3.14. Experimental intensities (markers) and fitting curves (continuous lines) for all the investigated samples. Error bars are less than marker size.

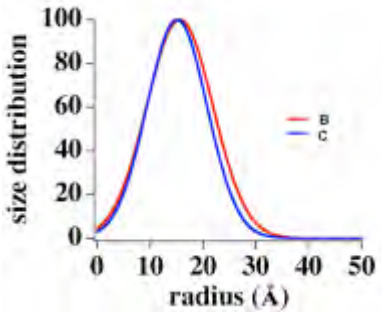

Figure 3.15. Gaussian size distributions for samples B and C as obtained by the fitting of SAXS data.

Table 3.2. SAXS data fitting results.

Spheres with Gaussian radius distribution model			**Cylinder with polydispersity on radius model**	
Model parameters	Sample B	Sample C	Model parameters	Sample A
Mean radius (nm)	1.4±0.1	1.5±0.1	*Radius (nm)*	1.5±0.1
Polydispersity (sig/avg)	0.40	0.37	*Length (nm)*	33.7
SLD sphere ($Å^{-2}$)	$1.23 \cdot 10^{-4}$	$1.23 \cdot 10^{-4}$	*Polydispersity of radius*	0.65
SLD solvent ($Å^{-2}$)	$9.36 \cdot 10^{-6}$	$9.36 \cdot 10^{-6}$	*SLD difference ($Å^{-2}$)*	$1.14 \cdot 10^{-4}$

The results of the fitting reveal the presence of smaller particles with respect to the results obtained by TEM measurements. Since a uniform Scattering Length Density (SLD) for gold has been used (in particular the bulk gold SLD), SAXS analysis can only reveal the crystalline gold core in the particles, therefore the size distributions returned from the fitting routines are centered at a radius significantly smaller than the ones obtained by TEM images analysis. As clearly visible by TEM images also, faceted particles are also present in the samples; since a spherical form factor has been used to analyze our SAXS data, these particles are only detectable by our fitting as a higher polydispersity of the populations.

Also for sample A the fitting reveals a smaller population: cylindrical objects with radius around 4 nm and length around 10 nm are visible in TEM images while SAXS data fitting returns values of 1.5 nm and 34 nm for the radius and the length respectively; the polydispersity in the radius is around 65%. The difference in the radius arising from the comparison of the two techniques can be ascribed in this case also to the difference in scattering length density between the inner core of the particles (bulk SLD) and the surface, while the longer length found with SAXS can arise from the presence of aggregates: in fact, SAXS spectra were acquired from more concentrated nanosols (1 mg/mL) while TEM grid

where prepared by dropping on the copper grid the original solutions (concentration around 0.1 mg/mL). In this case possible aggregates present in the more concentrated suspension could not be revealed.
In order to check if the particles' anisotropy can influence their assembly on a flat substrate, AFM measurement have been performed. AFM data analysis can easily show the arrangement of particles on a substrate [134-137]. Since the size of the particles, as inferred from the previous techniques, is around five nanometers, the samples have been deposited on mica, since this substrate is comparable to a flat surface at these lengthscales. Samples were deposited by spin coating 2 μL of the concentrated dispersions (1 mg Au/mL) at 3000 rpm for 60''. A solution of the polymer has been also deposited on mica substrate by spin coating 20 μL of a 0.3 wt% water solution at 3000 rpm for 60'' as "blank" sample. AFM images are shown in Figures 3.16-3.22.

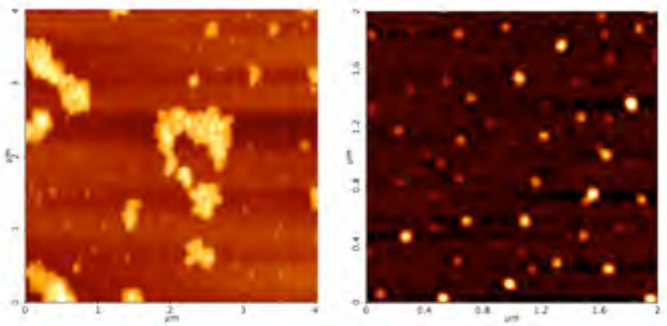

Figure 3.16. AFM images of sample A. Left: resolution 206x206 pxl; right: resolution 512x512 pxl.

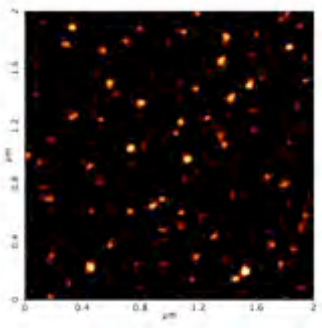

Figure 3.17. AFM images of sample B. Resolution 256x256 pxl.

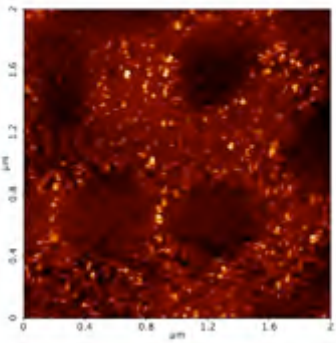

Figure 3.18. AFM image of sample C. Resolution 256 x 256 pxl.

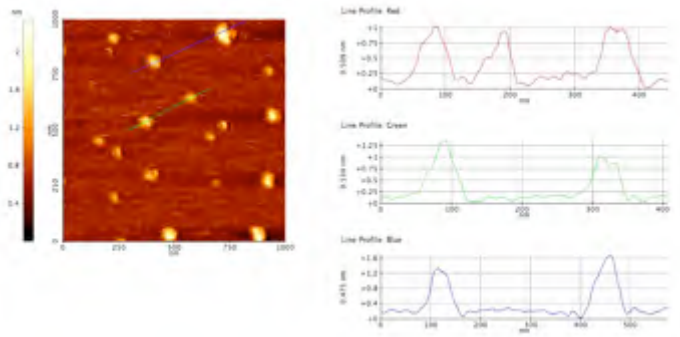

Figure 3.19. AFM image and height profile analysis of sample A. Resolution: 512x512 pxl.

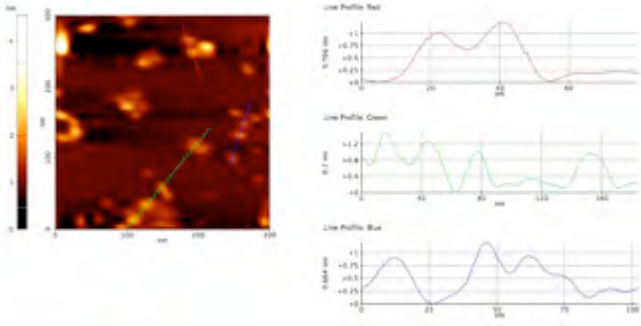

Figure 3.20. AFM image and height profile analysis of sample B. resolution: 512 x 512 pxl.

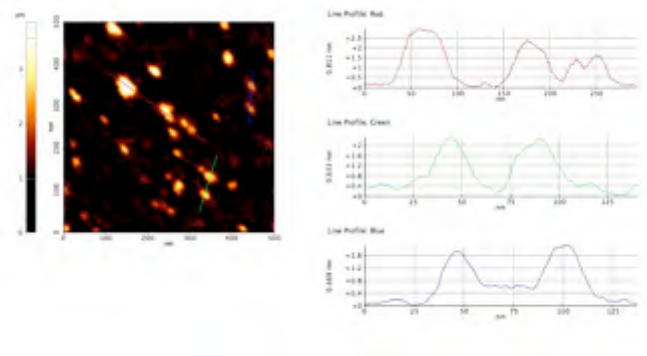

Figure 3.21. AFM image of sample C and corresponding height profile analysis. Resolution: 512x512 pxl.

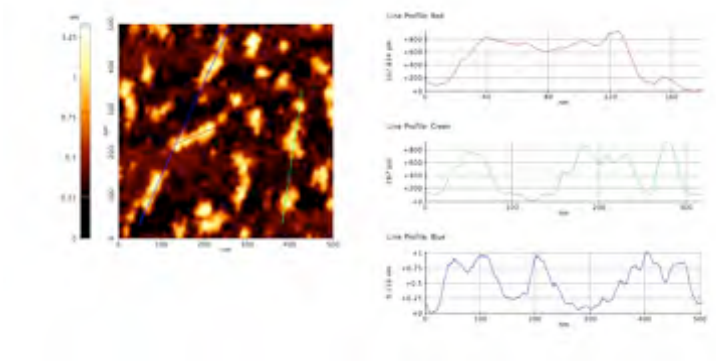

Figure 3.22. AFM height profile analysis of the polymer. Resolution: 256 x 256 pxl.

AFM images of the polymer show the presence of polymer bundles (Figure 3.22); the height analysis reveals that these structures have an average thickness of around 0.8 nm and irregular shape; therefore, the presence of spherical or elongated smooth structures in the AFM images of our samples can be ascribed to the metallic nanoparticles only.
The gold nanoparticles' sizes obtained from the height analysis are in agreement with the mean radii obtained by the previous techniques. As far as the morphology of the patterns obtained is concerned, in the case of sample A both aggregated bundles and some isolated particles are present as evident from Figure 3.16 while for samples B and C only

small aggregates composed of few particles are present; the latter probably due to the deposition method. These results are in agreement with SAXS data that already highlighted that in sample A, the one with the lower polymer content, aggregation occurs, probably due to the lack in stabilization of the particles due to the defect of stabilizer with respect to the two other samples. Therefore the polymer content also plays a key role in determining the pattern of the spin-coated thin films and could be used to drive the assembly of gold particles film with desired morphology on mica substrate. As clearly shown in Figure 3.13 for sample C, when the polymer content is higher a particular pattern is observed: a "patchy" film is obtained, and an inspection of the height profile reveal that there are some "holes" in the film where no particles are observed. This could be explained by a dewetting process of the polymer film with a consequent inhomogeneity of the particles' deposition on the substrate. This result also highlight that the polymer is firmly bound to the gold nanoparticles.

In order to understand the different amount of stabilizing chains that are present in each sample, a rough estimation can be made with some assumptions. Assuming a particle mean radius of about 2 nm, we can estimate the number of polymer chains/particle ratio. In order to first estimate the number of Au NP, the mean radius obtained by the analysis of TEM images, R_{TEM}, has been used as radius of the particles, not taking into account the polydispersity, and the volume of such particles, V_{NP}, has been calculated as:

$$V_{NP} = \frac{4}{3}\pi R_{TEM}^{\ 3} \qquad (3.10)$$

Then the ratio between the volume of a single atom (calculated using the gold atomic empirical radius, equal to 0.14 nm) and the volume of the particle has been calculated to obtain the number of Au atoms per particle, $N_{Au/NP}$; this value has been then used to estimate the average number of gold nanoparticles in solution, N_{NP}, according to:

$$N_{NP} = \frac{N_{Au}}{N_{Au/NP}} = \frac{mol_{Au} \cdot N_A}{N_{Au/NP}} \quad (3.11)$$

where mol_{Au} is the number of Au moles in solution and N_A is Avogadro's number.
Once obtained the average number of particles for each sample, the average number of polymer chains, N_{chains}, has been calculated. We assumed a polydispersity of the polymer molecular weight equal to one. The ratio between N_{chains} and N_{NP} gives an estimation of the number of polymer chains per particle in solution, N_{cpp}:

$$N_{cpp} = \frac{N_{chains}}{N_{NP}} = \frac{mol_{POL} \cdot N_A}{N_{NP}} \quad (3.12)$$

where mol_{POL} is the number of polymer moles in solution.
This calculation gives the results summarized in Table 3.3.

Table 3.3. Values of N_{ccp} for the three investigated samples.

	N_{cpp}
Sample A	27
Sample B	130
Sample C	650

In the case of sample A we obtained an average number of 27 chains for each particle, while in the B and C samples we found 130 and 650 chains respectively. These data evidence the low polymer content in sample A that can explain the aggregation occurring in this sample with respect to the other samples where the polymer content is higher.
To better understand the important role of the polymer chains as stabilizers, blank samples have also been prepared: the gold salt has been reduced in water without polymer in solution but using the same experimental conditions (gold concentration, reduction method) used for the corresponding polymer-containing samples. These reductions lead to unstable sample, and precipitation of the reduced products occurred within few hours, while samples A, B and C are stable for months. This clearly shows that the polymer chains,

also for low polymer concentration of the A samples, can not only template the particles' synthesis but also allow the nanosols to be stable for months, expecially for sample A, where the particles' mean size is higher than samples B and C and could more easily lead to flocculation and precipitation of the particles.
A significant difference between A and the other samples have been highlighted from all the investigation methods, showing that both B and C preparations lead to spherical isolated particles which radius is 2 nm and 3.5 nm respectively. The polydispersity for both samples is similar, showing that the templating effect, even if slightly smaller for the B sample (TEM images analysis gives p=0.22 for B versus p=0.15 for C), is already achieved with 130 polymer chains/particle. Further investigation concerning a screening of the polymer/gold ratio in the range from A and B experimental conditions could reveal a smaller polymer/gold ratio sufficient to obtain spherical non-aggregated particles.

3.4.4. Conclusions

A tri-block copolymer consisting of two PEG-methylacrylate chains anchored to a poly(methacrylic) moiety containing a trithiocarbonate unit has been synthesized by RAFT polymerization and has been used as templating agent in the synthesis of ultra-small gold nanoparticles by reduction of $HAuCl_4$ in water by the addition of ice-cold $NaBH_4$.
Different Au/polymer ratios have been explored; blank synthesis have been performed as well, showing that in the absence of the polymer the synthesis procedure leads to unstable particles, that precipitate within few hours. The samples have been extensively studied by means of UV-Visible Absorption, Small Angle X-Ray Scattering, Transmission Electron Microscopy and Atomic Force Microscopy.
The results show that the Au/polymer ratio has a strong effect on the morphology and size distribution of the particles obtained, varying from elongated and aggregated structures in the case of lower polymer content to monodisperse spherical

particles in the case of a higher templating agent content. In particular, a gold/polymer molar ratio equal to 10^3 leads to ellipsoidal particles and elongated structures, with mean radius of 1.5 nm and a mean length of about tenths of nanometers. Increasing the polymer content a higher isotropy is obtained: for a gold/polymer molar ratio equal to 4.6, monodispersed spherical particles with mean radius of 2.0 nm are obtained. The aggregation behavior of the as-obtained nanstuctures have been explored both in solution and on mica substrates, highlighting that the polymer plays a key role in the formation of particular patterns in spin-coated films.

These results reveal that this tri-block copolymer polymer is a good templating agent and by simply varying the polymer/gold ratio, nanostructures varying from monodipserse nanoparticles to elongated anisotropic structures with tunable optical properties can be easily obtained by a simple one-pot synthesis. The nanoparticles' dispersions can be concentrated up to 1g/L, perfectly retaining their stability over months.

3.5. Bibliography

[1] Daniel, M.-C. and Astruc, D., *Chem. Rev*. **2004**, *104*, 293.

[2] Turkevitch, J.; Stevenson, P. C.; Hillier, J. *Discuss. Faraday Soc*. **1951**, *11*, 55-75.

[3] Frens, G. *Nature: Phys. Sci.* **1973**, *241*, 20-22.

[4] Yonezawa, T.; Kunitake, T. *Colloids Surf. A: Physicochem. Eng. Asp*. **1999**, *149*, 193-199.

[5] Schmid, G.; Pfeil, R.; Boese, R.; Bandermann, F.; Meyer, S.; Calis, G. H. M.; van der Velden, J. W. A. *Chem. Ber.* **1981**, *114*, 3634-3642.

[6] Giersig, M.; Mulvaney, P.. *Langmuir* **1993**, *9*, 3408-3413.

[7] Hasan, M.; Bethell, D.; Brust, M. *J. Am. Chem. Soc.* **2003**, *125*, 1132- 1133.

[8] Brust, M.; Walker, M.; Bethell, D.; Schiffrin, D. J.; Whyman, R. J. *J. Chem. Soc., Chem. Commun.* **1994**, 801-802.

[9] Brust, M.; Fink, J.; Bethell, D.; Schiffrin, D. J.; Kiely, C. J. *J. Chem. Soc., Chem. Commun*. **1995**, 1655- 1656.

[10] Chen, S. *Langmuir* **1999**, *15*, 7551-7557.

[11] Chen, S.; Murray, R. W. *Langmuir* **1999**, *15*, 682-689.

[12] Hostetler, M. J.; Green, S. J.; Stokes, J. J.; Murray, R. W. *J. Am. Chem. Soc.* **1996**, *118*, 4212-4213.

[13] Ingram, R. S.; Hostetler, M. J.; Murray, R. W. *J. Am. Chem. Soc.* **1997**, *119*, 9175-9178.

[14] Templeton, A. C.; Wuelfing, W. P.; Murray, R. W. *Acc. Chem. Res.* **2000**, *33*, 27-36.

[15] Hostetler, M. J.; Wingate, J. E.; Zhong, C.-J.; Harris, J. E.; Vachet, R. W.; Clark, M. R.; Londono, J. D.; Green, S. J.; Stokes, J. J.; Wignall, G. D.; Glish, G. L.; Porter, M. D.; Evans, N. D.; Murray, R. W. *Langmuir* **1998**, *14*, 17-30.

[16] Templeton, A. C.; Hostetler, M. J.; Kraft, C. T.; Murray, R. W. *J. Am. Chem. Soc.* **1998**, *120*, 1906-1911.

[17] Hostetler, M. J.; Templeton, A. C.; Murray, R. W. D. *Langmuir* **1999**, *15*, 3782-3789.

[18] Waters, C. A.; Mills, A. J.; Johnson, K. A.; Schiffrin, D. J. *Chem. Commun.* **2003**, 540-541.
[19] Aslan, K.; Pérez-Luna, V. H. *Langmuir* **2002**, *18*, 6059-6065.
[20] Prasad, B. L. V.; Stoeva, S. I.; Sorensen, C. M.; Klabunde, K. J. *Langmuir* **2002**, *18*, 7515-7520.
[21] Prasad, B. L. V.; Stoeva, S. I.; Sorensen, C. M.; Klabunde, K. J. *Chem. Mater.* **2003**, *15*, 935-942.
[22] Andres, R. P.; Bielefeld, J. D.; Henderson, J. I.; Janes, D. B.; Kolagunta, V. R.; Kubiak, C. P.; Mahoney, W. J.; O. R. G. *Science* **1996**, *273*, 1690-1693.
[23] Lin, X. M.; Sorensen, C. M. *Chem. Mater.* **1999**, *11*, 198-202.
[24] Brown, L. O.; Hutchison, J. E.. *J. Phys. Chem. B* **2001**, *105*, 8911-8916.
[25] Stoeva, S. I.; Prasad, B. L. V.; Uma, S.; Stoimenov, P. K.; Zaikovsky, V.; Sorensen, C. M.; Klabunde, K. J. *J. Phys. Chem. B* **2003**, *107*, 7441-7448.
[26] Li, W.; Huo, L.; Wang, D.; Zeng, G.; Xi, S.; Zhao, B.; Zhu, J.; Wang, J.; Shen, Y.; Lu, Z. *Colloids Surf.* **2000**, *175*, 217-223.
[27] Wang, T.; Zhang, D.; Xu, W.; Zhu, D. *Synth. Met.* **2003**, *135-136*, 835-836.
[28] Kanehara, M.; Oumi, Y.; Sano, T.; Teranishi, T. *J. Am. Chem. Soc.* **2003**, *125*, 8708.
[29] Teranishi, T. In *Dendrimers and Nanoscience*; Astruc, D., Ed.; Compte-Rendus Chimie, Elsevier: Paris, 2003.
[30] Dieluweit, S.; Pum, D.; Sleytr, U. B. *Supramol. Sci.* **1998**, *5*, 15-19.
[31] Sarathy, K. V.; Kulkarni, G. U.; Rao, C. N. R. *Chem. Commun.* **1997**, 537-538.
[32] Ascencio, J. A.; Pérez, M.; José-Yacaman, M. *Surf. Sci.* **2000**, *447*, 73-80.
[33] Chushak, Y.; Bartell, L. S. *Eur. Phys. J. D* **2001**, *16*, 43-46.
[34] Yee, C. K.; Jordan, R.; Ulman, A.; White, H.; King, A.; Rafailovich, M.; Sokolov, J. *Langmuir* **1999**, *15*, 3486-3491.
[35] Selvakannan, P. R.; Mandal, S.; Pasricha, R.; Adyanthaya, S. D.; Sastry, M. *Chem. Commun.* **2002**,

1334-1335.
[36] Wei, G.-T.; Liu, F.-K.; Wang, C. R. C. *Anal. Chem.* **1999**, *71*, 2085-2091.
[37] Sun, L.; Crooks, R. M.; Chechik, V. *Chem. Commun.* **2001**, 359-360.
[38] Helcher, H. H. *Aurum Potabile oder Gold Tinstur*; J. Herbord Klossen: Breslau and Leipzig, 1718.
[39] Hayat, M. A. Colloidal Gold, Principles, Methods and Applications; Academic Press: New York, 1989.
[40] Napper, D. H. Academic Press: London, 1983.
[41] Tuzar, Z.; Kratochvil, P. Plenum Press: New York, 1993; Vol. 15.
[42] Mayer, A. B. R.; Mark, J. E. In *Nanotechnology, Molecularly Designed Materials*; Chow, G. M., Gonsalves, K. E., Eds.; ACS Symposium Series 622; American Chemical Society: Washington, DC, 1996.
[43] Roucoux, A.; Schultz, J.; Patin, H. *Chem. Rev.* **2002**, *102*, 3757-3778.
[44] Hyatt, A. D., Eaton, B. T., Eds.; CRC Press: Boca Raton, FL, 1993.
[45] Ziolo, R. F.; Giannelis, E. P.; Weinstein, B. A.; O'Horo, M. P.; Gamguly, B. N.; Mehrota, V.; Russel, M. W.; Huffman, D. R. *Science* **1992**, *257*, 219-223.
[46] Jordan, R.; West, N.; Chou, Y.-M.; Nuyken, O. *Macromolecules* **2001**, *34*, 1606-1611.
[47] Selvan, S. T.; Spatz, J. P.; Klock, H.-A.; Möller, M. *Adv. Mater*. **1998**, *10*, 132-134.
[48] Sayo, K.; Deki, S.; Hayashi, S. *Eur. Phys. J. D* **1999**, *9*, 429-432.
[49] Lee, J.; Sundar, V. C.; Heine, J. R.; Bawendi, M. G.; Jensen, K. F. *Adv. Mater*. **2000**, *12*, 1102-1105.
[50] Raula, J.; Shan, J.; Nuopponen, M.; Niskanen, A.; Jiang, H.; Kauppinen, E. I.; Tenhu, H. *Langmuir* **2003**, *19*, 3499-3504.
[51] Corbierre, M. K.; Cameron, N. S.; Sutton, M.; Mochrie, S. G. J.; Lurio, L. B.; Rühm, A.; Lennox, R. B. *J. Am. Chem. Soc.* **2001**, *123*, 10411-10412.
[52] Kolb, U.; Quaiser, S. A.; Winter, M.; Reetz, M. T. *Chem. Mater*. **1996**, *8*, 1889-1894.
[53] Hirai, H.; Toshima, N. In *Polymer-Attached Catalysts*;

Iwasawa, Y., Ed.; Kluwer: Dordrecht, 1986.
[54] Toshima, N.; Yonezawa, T. *New J. Chem*. **1998**, 1179-1201.
[55] Hirai, H.; Nakao, Y.; Toshima, *J. Macromol. Sci. Chem*. **1979**, *A13*, 727-750.
[56] Teranishi, T.; Miyake, M. *Hyomen* **1997**, *35*, 439-452.
[57] Esumi, K.; Susuki, A.; Aihara, N.; Usui, K.; Torigoe, K. *Langmuir* **1998**, *14*, 3157-3159.
[58] Reetz, M. T.; Helbig, W. *J. Am. Chem. Soc.* **1994**, *116*, 7401-7402.
[59] Schaaf, T. G.; Whetten, R. L. *J. Phys. Chem. B* **2000**, *104*, 2630-2641.
[60] Toshima, N.; Harada, M.; Yamazaki, Y.; Asakura, K. *J. Phys. Chem*. **1992**, *96*, 9927-9933.
[61] Harada, M.; Asakura, K.; Toshima, N. *J. Phys. Chem*. **1993**, *97*, 5103-5114.
[62] Toshima, N.; Yonezawa, T. *Makromol. Chem., Macromol. Symp*. **1992**, *59*, 281-295.
[63] Yonezawa, T.; Toshima, N. *J. Mol. Catal*. **1993**, *83*, 167-181.
[64] Yoneazawa, T.; Toshima, N. *J. Chem. Soc., Faraday Trans*. **1995**, *91*, 4111-4119.
[65] Astruc, D. Redox Catalysis. *Electron Transfer and Radical Processes in Transition Metal Chemistry*; VCH: New York, 1995; Chapter 7.
[66] Harada, M.; Asakura, K.; Toshima, N. J. *J. Phys. Chem*. **1993**, *97*, 5103.
[67] Spatz, J. P.; Mössmer, S.; Möller, M. *Chem.-Eur. J*. **1996**, *12*, 1552-1555.
[68] Spatz, J. P.; Mössmer, S.; Möller, M. *Angew. Chem., Int. Ed. Engl*. **1996**, *35*, 1510-1512.
[69] Spatz, J. P.; Roescher, A.; Möller, M. *Adv. Mater*. **1996**, *8*, 337-340.
[70] Bronstein, L. M.; Chernyshov, D. M.; Timofeeva, G. I.; Dubrovina, L. V.; Valetsky, P. M.; Obolonkova, E. S.; Khokhlov, A. R. *Langmuir* **2000**, *16*, 3626-3632.
[71] Frankamp, B. L.; Uzun, O.; Ilhan, F.; Boal, A. K.; Rotello, V. M. *J. Am. Chem. Soc*. **2002**, *124*, 892-893.
[72] Spatz, J. P.; Mössmer, S.; Harmann, C.; Möller, M.; Herzog, T.; Krieger, M.; Boyen, H.-G.; Ziemann, P.;

Kabius, B. *Langmuir* **2000**, *16*, 407-415.
[73] Gohy, J. F.; Willet, N.; Varshney, S.; Zhang, J.-X.; Jérôme, R. *Angew. Chem., Int. Ed*. **2001**, *40*, 3214-3216.
[74] Youk, J. H.; Park, M. K.; Locklin, J.; Advincula, R.; Yang, J.; Mays, J. *Langmuir* **2002**, *18*, 2455-2458.
[75] Walker, C. H.; St John, J. V.; Wisian-Neilson, P. *J. Am. Chem. Soc*. **2001**, *123*, 3846-3847.
[76] Otsuka, H.; Akiyama, Y.; Nagasaki, Y.; Kataoka, K. *J. Am. Chem. Soc*. **2001**, *123*, 8226-8230.
[77] Nuss, S.; Böttcher, H.; Wurm, H.; Hallensleben, M. L. *Angew. Chem., Int. Ed.* **2001**, *40*, 4016-4018.
[78] Mandal, T. K.; Fleming, M. S.; Walt, D. R. *Nano Lett.* **2002**, *2*, 3-7.
[79] Ohno, K.; Hoh, K.-m.; Tsuji, Y.; Fukuda, T. *Macromolecules* **2002**, *35*, 8989-8993.
[80] Kamata, K.; Lu, Y.; Xia, Y. *J. Am. Chem. Soc.* **2003**, *125*, 2384-2385.
[81] Marinakos, S. M.; Shultz, D. A.; Feldheim, D. L. *Adv. Mater.* **1999**, *11*, 34-37.
[82] Chah, S.; Fendler, J. H.; Yi, J. *J. Colloid Interface Sci.* **2002**, *250*, 142-148.
[83] Marinakos, S. M.; Novak, J. P.; Brousseau, L. C., III; House, A. B.; Edeki, E. M.; Feldhaus, J. C.; Feldheim, D. L. *J. Am. Chem. Soc.* **1999**, *121*, 8518-8522.
[84] Naka, K.; Itoh, H.; Chujo, Y. *Langmuir* **2003**, *19*, 5546-5549.
[85] Sohn, B.-H.; Seo, B.-W.; Yoo, S.-I. *J. Mater. Chem.* **2002**, *12*, 1730-1734.
[86] Cant, N. E.; Critchley, K.; Zhang, H.-L.; Evans, S. D. *Thin Solid Films* **2003**, *426*, 31-39.
[87] Gonsalves, K. E.; Carlson, G.; Chen, X.; Kumar, J.; Aranda, F.; Perez, R.; Jose-Yacaman, M. *J. Mater. Sci. Lett.* **1996**, *15*, 948-951.
[88] Mayer, A. B. R.; Mark, J. E. *Eur. Polym. J.* **1998**, *34*, 103-108.
[89] Teranishi, T.; Kiyokawa, I.; Miyake, M. *Adv. Mater.* **1998**, *10*, 596-599.
[90] Watson, K. J.; Zhu, J.; Nguyen, S. B. T.; Mirkin, C. A. *J. Am. Chem. Soc.* **1999**, *121*, 462-463.

[91] Watson, K. J.; Zhu, J.; Nguyen, S. B. T.; Mirkin, C. A. *Pure Appl. Chem.* **2000**, *72*, 67-72.
[92] Grabar, K. C.; Allison, K. J.; Baker, B. E.; Bright, R. M.; Brown, K. R.; Freeman, R. G.; Fox, A. P.; Keating, C. D.; Musick, M. D.; Natan, M. J. *Langmuir* **1996**, *12*, 2353-2361.
[93] Kim, M.; Sohn, K.; Na, H. B.; Hyeon, T. *Nano Lett.* **2002**, *2*, 1383-1387.
[94] Wolfe, D. B.; Oldenburg, S. J.; Westcott, S. L.; Jackson, J. B.; Paley, M. S.; Halas, N. J. *Langmuir* **1999**, *15*, 2745-2748.
[95] Takagi, K.; Ishiwatari, T. *Chem. Lett.* **2002**, 990-991.
[96] Wang, J.; Neoh, K. G.; Kang, E. T. *J. Colloid Surf. Sci.* **2001**, *239*, 78-86.
[97] Shchukin, D. G.; Caruso, R. A. *Chem. Commun.* **2003**, 1478-1479.
[98] Walker, C. H.; St. John, J. V.; Wisian-Neilson, P. *J. Am. Chem. Soc.* **2001**, *123*, 3846-3847.
[99] Mayer, C. R.; Neveu, S.; Cabuil, V. *Angew. Chem., Int. Ed.* **2002**, *41*, 501-503.
[100] Mayer, C. R.; Neveu, S.; Simonnet-Jégat, C.; Debiemme-Chouvry, C.; Cabuil, V.; Secheresse, F. *J. Mater. Chem.* **2003**, *13*, 338-341.
[101] Shan, J.; Nuopponen, M.; Jiang, H.; Kauppinen, E.; Tenhu, H. *Macromolecules* **2003**, *36*, 4526-4533.
[102] Dai, X.; Tan, Y.; Xu, J. *Langmuir* **2002**, *18*, 9010-9016.
[103] Zhou, Y.; Itoh, H.; Uemura, T.; Naka, K.; Chujo, Y. *Chem. Commun.* **2001**, 613-614.
[104] Youk, J. H.; Park, M.-K.; Locklin, J.; Advincula, R.; Yang, J.; Mays, J. *Langmuir* **2002**, *18*, 2455-2458.
[105] Mangeney, C.; Ferrage, F.; Aujard, I.; Marchi-Artzner, V.; Jullien, L.; Ouari, O.; El Rekai, D.; Laschewsky, A.; Vikholm, I.; Sadowski, J. W. *J. Am. Chem. Soc.* **2002**, *124*, 5811-5821.
[106] Cole, D. H.; Shull, K. R.; Rehn, L. E.; Baldo, P. M. *Nucl. Instrum. Methods Phys. Res. B* **1998**, *136-138*, 283-289.
[107] Liang, Z.; Susha, A.; Caruso, F. *Chem. Mater*. **2003**, *15*, 3176-3183.
[108] Falletta, E.; Fratini, E.; Ridi, F.; Vannucci, C.; Canton,

P.; Bianchi, S.; Castelvetro, V. and Baglioni, P. Submitted to *J. Phys. Chem. C*.
[109] Hussain, I.; Graham, S.; Wang, Z.; Tan, B.; Sherrington, D. C.; Rannard, S. P.; Cooper, A. I.; Brust, M. *J. Am. Chem. Soc.* **2005**, *127*, 16398-16399.
[110] Wang, Z.; Tan, B.; Hussain, I.; Schaeffer, N.; Wyatt, M. F.; Brust, M.; Cooper, A. I. *Langmuir* **2007**, *23*, 885-895.
[111] Kotal, A.; Mandal, T. K.; Walt, D. R. *J. Polym. Sci. Pol. Chem.* **2005**, *43*, 3631-3642.
[112] Abraham, S.; Kim, I.; Batt, C. A. *Angew. Chem. Int. Ed.* **2007**, *46*, 5720-5723.
[113] Kim, B. J.; Fredrickson, G. H.; Kramer, E. J. *Macromolecules* **2008**, *41*, 436-447.
[114] Sanchez-Gaytan, B. L.; Cui, W.; Kim, Y.; Mendez-Polanco, M. A.; Duncan, T. V.; Fryd, M.; Wayland, B. B.; Park, S.-J. *Angew. Chem. Int. Edit.* **2007**, *46*, 9235-9238.
[115] Abyaneh, M. K.; Pasricha, R.; Gosavi, S. W.; Kulkarni, S. K. *Nanotechnology* **2006**, *17*, 4129-4134.
[116] Aizawa, M.; Buriak, J. M. *Chem. Mater.* **2007**, *19*, 5090-5101.
[117] Gindy, M. E.; Panagiotopoulos, A. Z.; Prud'homme, R. K. *Langmuir* **2008**, *24*, 83-90.
[118] Dai, C.-A.; Wu, Y.-L.; Lee, Y.-H.; Chang, C.-J.; Su, W.-F. *J. Cryst. Growth* **2006**, *288*, 128-136.
[119] Meli, L.; Li, Y.; Lim, K. T.; Johnston, K. P.; Green, P. F. *Macromolecules* **2007**, *40*, 6713-6720.
[120] Abyaneh, M. K.; Paramanik, D.; Varma, S.; Gosavi, S. W.; Kulkarni, S. K. *J. Appl. Phys.* **2007**, *40*, 3771-3779.
[121] Alexandrov, A.; Smirnova, L.; Yakimovich, N.; Sapogova, N.; Soustov, L.; Kirsanov, A.; Bityurin, N. *Appl. Surf. Sci.* **2005**, *248*, 181-184.
[122] Azzam, T.; Eisenberg, A. *Langmuir* **2007**, *23*, 2126-2132.
[123] Vannucci, C.; Fratini, E.; Bianchi, S.; Castelvetro, V.; Baglioni, P. *Manuscript in preparation*.
[124] Blanton, T. N.; Huang, T. C.; Toraya, H.; Hubbard, C. R.; Robie, S. B.; Louer, D.; Goebel, H. E.; Will,

G.; Gilles, R.; Rafetery, T. *Powder Diffraction* **1995**, *10*, 91-100.
[125] Singh, M. A.; Ghosh, S. S.; Shannon, R. F. *J. Appl. Cristallogr.* **1993**, *26*, 787-794.
[126] Mie, G. *Ann Phys* **1908**, *25*, 377-445.
[127] Lica, G. C.; Zelakiewicz, B. S.; Constantinescu, M.; Tong, Y. Y. *J. Phys. Chem. B* **2004**, *108*, 19896-19900.
[128] Kürbitz, S.; Porstendorfer, J.; Berg, K.-J.; Berg, G. *Appl. Phys. B- Lasers O.* **2001**, *73*, 333-337.
[129] Hoefelmeyer, J. D.; Liu, H.; Somorjai, G. A.; Tilley, T. D. *J. Colloid Interf. Sci.* **2007**, *309*, 86-93.
[130] Dass, A.; Guo, R.; Tracy, J. B.; Balasubramanian, R.; Douglas, A. D.; Murray, R. W. *Langmuir* **2008**, *24*, 310-315.
[131] Chiu, J. J.; Kim, B. J.; Yi, G.-R.; Bang, J.; Kramer, E. J.; Pine, D. J. *Macromolecules* **2007**, *40*, 3361-3365.
[132] Bonini, M.; Fratini, E.; Baglioni, P. *Mater. Sci. Eng. C* **2007**, *27*, 1377-1381.
[133] Bonini, M.; Wiedenmann, A.; Baglioni, P. *Physica A* **2004**, *339*, 86-91.
[134] Vandamme, N.; Snauwaert, J.; Janssens, E.; Vandeweert, E.; Lievens, P.; Van Haesendonck, C. *Surf. Sci.* **2004**, *558*, 57-64.
[135] Shi, C.; Tian, L.; Wu, L.; Zhu, J. *J. Phys. Chem. C* **2007**, *111*, 1243-1247.
[136] Lai, J. T.; Filla, D. Shea, R. *Macromolecules* **2002**, *35*, 6754-6756.
[137] Luo, J.; Jones, V. W.; Han, L.; Maye, M. M.; Kariuki, N. N.; Zhong, C. J. *J. Phys. Chem. B* **2004**, *108*, 9669-9677.

4. Magnetic nanocomposites

4.1. Introduction

Magnetic nanoparticles are of great interest for researchers from a wide range of disciplines, including magnetic fluids [1], catalysis [2,3], biotechnology/biomedicine [4], magnetic resonance imaging [5, 6], data storage [7], and environmental remediation [8, 9]. While a number of suitable methods have been developed for the synthesis of magnetic nanoparticles of various different compositions, successful application of such magnetic nanoparticles in the areas listed above is highly dependent on the stability of the particles under a range of different conditions. In most of the envisaged applications, the particles perform best when the size of the nanoparticles is below a critical value, which is dependent on the material but is typically around 10–20 nm. Then each nanoparticle becomes a single magnetic domain and shows a superparamagnetic behavior when the temperature is above the so-called blocking temperature. Such individual nanoparticles have a large constant magnetic moment and behave like a giant paramagnetic atom with a fast response to applied magnetic fields with negligible remanence (residual magnetism) and coercivity (the field required to bring the magnetization to zero). These features make superparamagnetic nanoparticles very attractive for a broad range of biomedical applications because the risk of forming agglomerates is negligible at room temperature.

However, an unavoidable problem associated with particles in this size range is their intrinsic instability over longer periods of time. Such small particles tend to form agglomerates to reduce the energy associated with the high surface area to volume ratio. Moreover, naked metallic nanoparticles are chemically highly active, and are easily oxidized in air, resulting generally in loss of magnetism and dispersibility. For many applications it is thus crucial to develop protection strategies to chemically stabilize the naked magnetic nanoparticles against degradation during or after the synthesis. These strategies comprise grafting of or coating with organic species, including surfactants or polymers, or coating with an inorganic layer, such as silica or carbon. It is noteworthy that in many cases the protecting shells not only

stabilize the nanoparticles, but can also be used for further functionalization, for instance with other nanoparticles or various ligands, depending on the desired application.

4.2. Magnetic nanoparticles' synthesis

Magnetic nanoparticles have been synthesized with a number of different compositions and phases, including iron oxides, such as Fe_3O_4 (magnetite) and γ-Fe_2O_3 (maghemite) [10-12], pure metals, such as Fe and Co [13,14], spinel-type ferromagnets, such as $MgFe_2O_4$, $MnFe_2O_4$, and $CoFe_2O_4$ [15,16] as well as alloys, such as $CoPt_3$ and FePt [17,18]. In the last decades, much research has been devoted to the synthesis of magnetic nanoparticles. Especially during the last few years, many publications have described efficient synthetic routes to shape-controlled, highly stable, and monodisperse magnetic nanoparticles. Several popular methods including co-precipitation, thermal decomposition and/or reduction, micelle synthesis, hydrothermal synthesis, and laser pyrolysis techniques can all be directed at the synthesis of high-quality magnetic nanoparticles.

4.2.1. Synthesis by coprecipitation

Co-precipitation is a facile and convenient way to synthesize iron oxides (either Fe_3O_4 or γ-Fe_2O_3) from aqueous Fe^{2+}/Fe^{3+} salt solutions by the addition of a base under inert atmosphere at room temperature or at elevated temperature. The size, shape, and composition of the magnetic nanoparticles depends very much on the type of salts used (e.g. chlorides, sulfates, nitrates), the Fe^{2+}/Fe^{3+} ratio, the reaction temperature, the pH value and ionic strength of the media. With this synthesis, once the synthetic conditions are fixed, the quality of the magnetite nanoparticles is fully reproducible. The magnetic saturation values of magnetite nanoparticles are experimentally determined to be in the range of 30–50 emu·g^{-1}, which is lower than the bulk value, 90 emu·g^{-1}. Magnetite nanoparticles are not very stable under ambient conditions, and are easily oxidized to maghemite or dissolved in an acidic medium. Since maghemite is a ferrimagnet, oxidation is the lesser problem. Therefore, magnetite particles can be subjected to deliberate oxidation to

convert them into maghemite. This transformation is achieved by dispersing them in acidic medium, then addition of iron(III) nitrate. The maghemite particles obtained are then chemically stable in alkaline and acidic medium.

However, even if the magnetite particles are converted into maghemite after their initial formation, the experimental challenge in the synthesis of Fe_3O_4 by co-precipitation lies in control of the particle size and thus achieving a narrow particle size distribution. Since the blocking temperature depends on particle size, a wide particle size distribution will result in a wide range of blocking temperatures and therefore non-ideal magnetic behavior for many applications. Particles prepared by co-precipitation unfortunately tend to be rather polydisperse. It is well known that a short burst of nucleation and subsequent slow controlled growth is crucial to produce monodisperse particles. Controlling these processes is therefore the key in the production of monodisperse iron oxide magnetic nanoparticles.

Recently, significant advances in preparing monodisperse magnetite nanoparticles, of different sizes, have been made by the use of organic additives as stabilization and/or reducing agents. For example, magnetite nanoparticles with sizes of 4–10 nm can be stabilized in an aqueous solution of 1 wt% polyvinlyalcohol (PVA). However, when using PVA containing 0.1 mol% carboxyl groups as the stabilizing agent, magnetite nanoparticles in the form of chainlike clusters precipitate [19]. This result indicates that the selection of a proper surfactant is an important issue for the stabilization of such particles. Size-tunable maghemite nanoparticles were prepared by initial formation of magnetite in the presence of the trisodium salt of citric acid, in an alkaline medium, and subsequent oxidation at 90°C for 30 min by iron(III) nitrate. The particle sizes can be varied from 2 to 8 nm by adjusting the molar ratio of citrate ions and metal ions (Fe^{2+} and Fe^{3+}) [20]. The effects of several organic anions, such as carboxylate and hydroxy carboxylate ions, on the formation of iron oxides or oxyhydroxides have been studied extensively [21-23]. The formation of surface complexes requires both deprotonated carboxy and deprotonated a-hydroxy groups [24]. Recent studies showed that oleic acid is the best candidate for the stabilization of Fe_3O_4 [25,26]. The effect of organic ions on the formation of metal oxides or oxyhydroxides can be rationalized by two competing mechanisms. Chelation of the metal ions can prevent nucleation and lead to the formation of larger particles because the number of nuclei formed is small and the system is dominated by particle growth. On the other hand, the

adsorption of additives on the nuclei and the growing crystals may inhibit the growth of the particles, which favors the formation of small units.

4.3. Surfactant and Polymer Coating

Surfactants or polymers are often employed to passivate the surface of the nanoparticles during or after the synthesis to avoid agglomeration. In general, electrostatic or steric repulsion can be used to disperse nanoparticles and keep them in a stable colloidal state. The best known example for such systems are the ferrofluids which were synthesized by Papell in 1965 [27] In the case of ferrofluids, the surface properties of the magnetic particles are the main factors determining colloidal stability. The major measures used to enhance the stability of ferrofluids are the control of surface charge [28] and the use of specific surfactants [29-31]. For instance, magnetite nanoparticles synthesized through the co-precipitation of Fe^{2+} and Fe^{3+} in ammonia or NaOH solution are usually negatively charged, resulting in agglomeration. To achieve stable colloids, the magnetite nanoparticle after precipitation can be peptized (i.e. dispersing a precipitate to form a colloid) with aqueous tetramethylammonium hydroxide or with aqueous perchloric acid [28]. The magnetite nanoparticles can be acidified with a solution of nitric acid and then further oxidized to maghemite by iron nitrate. After centrifugation and redispersion in water, a ferrofluid based on positively charged γ-Fe_2O_3 nanoparticles was obtained, since the surface hydroxy groups are protonated in the acidic medium [32]. Commercially, water- or oil- based ferrofluids are available. They are usually stable when the pH value is below 5 (acidic ferrofluid) or over 8 (alkaline ferrofluid).

In general, surfactants or polymers can be chemically anchored or physically adsorbed on magnetic nanoparticles to form a single or double layer [33,34], which creates repulsive (mainly steric) forces to balance the magnetic and the van der Waals attractive forces acting on the nanoparticles. Thus, by steric repulsion, the magnetic particles are stabilized in suspension. Polymers containing functional groups, such as carboxylic acids, phosphates, and sulfates, can bind to the magnetite surface [35]. Suitable polymers for coating include poly(pyrrole), poly(aniline), poly(alkylcyanoacrylates), poly(methylidene malonate), and polyesters, such as

poly(lactic acid), poly (glycolic acid), poly(ε-caprolactone), and their copolymers [36-39]. Surface-modified magnetic nanoparticles with certain biocompatible polymers are intensively studied for magnetic-field-directed drug targeting, and as contrast agents for magnetic resonance imaging [40,41].

Chu et al. reported a synthesis of polymer-coated magnetite nanoparticles by a single inverse microemulsion [42]. The magnetite particles were first synthesized in an inverse microemulsion, consisting of water/sodium bis(2-ethylhexyl-sulfosuccinate)/ toluene. Subsequently, water, monomers (methacrylic acid and hydroxyethyl methacrylate), crosslinker (N,N'-methylenebis(acrylamide)), and an initiator (2,2'-azobis(isobutyronitrile)) were added to the reaction mixture under nitrogen, and the polymerization reaction was conducted at 55°C. After polymerization, the particles were recovered by precipitation in an excess of an acetone/ methanol mixture (9:1 ratio). The polymer-coated nanoparticles have superparamagnetic properties and a narrow size distribution at a size of about 80 nm. However, the long term stability of these polymer-coated nanoparticles was not addressed. Polyaniline can also be used to coat nanosized ferromagnetic Fe_3O_4 by oxidative polymerization in the presence of the oxidant ammonium peroxodisulfate [43]. The obtained nanoparticles are polydisperse (20–30 nm averaged diameter) and have the expected core–shell morphology. Asher et al. reported that single iron oxide particles (ca. 10 nm) can be embedded in polystyrene spheres through emulsion polymerization to give stable superparamagnetic photonic crystals [44]. Polystyrene coating of iron oxide nanoparticles was also achieved by atom transfer radical polymerization [45,46]. For instance, Zhang et al. have used this method for coating $MnFe_2O_4$ nanoparticles with polystyrene, yielding core–shell nanoparticles with sizes below 15 nm. $MnFe_2O_4$ nanoparticles (ca. 9 nm) were stirred overnight in aqueous initiator solution, 3-chloropropionic acid, at pH 4 [45]. After washing out the excess initiator, air-dried nanoparticles were added to a styrene solution under nitrogen, then xylene, containing CuCl and 4,4'-dinonyl-2,2'-dipyridyl was added. The solution was stirred and kept at 130°C for 24 h to give the polystyrene coated $MnFe_2O_4$ nanoparticles. When using a free radical polymerization with $K_2S_2O_8$ as the catalyst, predominantly polystyrene particles without a magnetic core were obtained. This result confirms that the surface-grafted initiator is important for the coating of the nanoparticles.

Metallic magnetic nanoparticles, stabilized by single or double layers of surfactant or polymer are not air stable, and are easily leached by acidic solution [47], resulting in the loss of their magnetization. A thin polymer coating is not a good enough barrier to prevent oxidation of the highly reactive metal particles. Polymer coating is thus not very suitable to protect very reactive magnetic nanoparticles.
Another drawback of polymer-coated magnetic nanoparticles is the relatively low intrinsic stability of the coating at higher temperature, a problem which is even enhanced by a possible catalytic action of the metallic cores. Therefore, the development of other methods for protecting magnetic nanoparticles against deterioration is of great importance.

4.4. Functionalization of Coated Magnetic Nanoparticles

As mentioned above, a protective shell does not only serve to protect the magnetic nanoparticles against degradation, degradation, but can also be used for further functionalization with specific components, such as catalytically active species, various drugs, specific binding sites, or other functional groups. The easy separation and controlled placement of these functionalized magnetic nanoparticles by means of an external magnetic field enables their application as catalyst supports, in immobilized enzyme processes [48], and the construction of magnetically controllable bio-electrocatalytic systems [49,50].
Salgueiriño-Maceira et al. reported a synthesis of iron oxide nanoparticles, coated with a silica shell that were subsequently functionalized with gold nanoparticles [51]. Aqueous dispersions of the iron oxide magnetic nanoparticles were coated with a silica shell by the Stöber process. The negatively charged silica surface was then sequentially coated with positively-negatively-positively charged polyelectrolyte polymers through electrostatic interactions, followed by the adsorption of citrate-stabilized 15 nm gold nanoparticles. Using those gold particles as seeds, the gold shell was formed onto the magnetic silica spheres step-by-step with reducing aliquots of $HAuCl_4$ and ascorbic acid in aqueous solution. These gold-coated magnetic silica spheres have a strong resonance absorption in the visible and near-infrared range and can be controlled by using an external magnetic field, which makes them very promising in biomedical

applications. The difficulty in preparing functional-polymer magnetic microspheres arises from the magnetic dipolar interaction between adjacent magnetic nanoparticles, this makes it impossible to carry out polymerization on the surface of inorganic magnetic nanoparticles. Recently, a successful example was published for the preparation of thermoresponsive- polymer magnetic microspheres based on cross-linked N-isopropylacrylamide (NIPAM) by a colloidal template polymerization. Briefly, magnetic nanoparticles were synthesized by co-precipitation and stabilized by trisodium citrate, then silica coated through the Stöber process. The silica-coated nanoparticles were then functionalized with 3-(trimethoxysily) propyl methacrylate, leading to the formation of C=C bonds on the surface. Finally, NIPAM was polymerized with N,N'-methylene bisacrylamide as the crosslinker by seed precipitation polymerization in the presence of MPS-modified (MPS=3-(trimethoxysily)propyl methacrylate) silica-coated nanoparticles as seeds, resulting in the formation of PNIPAM magnetic microspheres, which are thermoresponsive [52].
Another method for the functionalization of magnetic nanoparticles is ligand exchange, by which the as-synthesized magnetic nanoparticles in an organic phase can be converted into water soluble ones. Rotello and co-workers reported [53] that iron oxide nanoparticles dispersed in a toluene solution can be completely transferred into aqueous solution under stirring with octa(tetramethylammonium)– polyhedral oligomeric silsesquioxane (TMA–POSS). Interestingly, this TMA– POSS exchange strategy can be applied to different monolayer-protected magnetic nanoparticles, such as oleic acid stabilized iron oxide nanoparticles, and oleic acid, oleylamine, or hexadecanediol stabilized FePt nanoparticles. The watersoluble nanoparticles obtained have excellent stability in biologically relevant pH ranges and salt concentrations.

4.5. Magnetic fluids as smart materials

Unlike paramagnets and diamagnets, which can be gaseous, liquid or solid, ferromagnets are almost exclusively solid. There exist, however, liquids with a susceptibility of roughly one, not as high as many ferromagnets, but still much higher than that of many paramagnets. As ferromagnets they can

easily reach their saturation magnetization. These so-called magnetic fluids or ferrofluids are actually two-phase systems, composed of small ferro-or ferrimagnetic particles dispersed in a liquid [54-56]. The surface of the magnetic particles has to be modified, for example by the grafing of a proper stabilizer, such as oleic acid. A second approach is surface charging, by adjusting the pH, to prevent particle agglomeration.

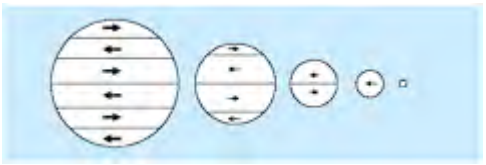

Figure 4.1. Schematic figure of the change of numbers of domain according to the particle size.

Because of their small size, these magnetic colloids contain usually a single domain, and therefore have a permanent magnetic moment proportional to their volume (Figure 4.1). Although magnetic colloids are ferromagnetic on the molecular scale, they resemble a paramagnet on the colloidal scale, with the difference that the magnetic moments of magnetic colloids are much larger than the moments in a paramagnet. This is the reason why ferrofluids are sometimes called *superparamagnetic*. In order to be s*uperparamagnetic*, the dipole moment of each particle must be free to rotate on the time scale of the experiment. Two modes of rotation are operative in magnetic colloids. One of them is Brownian rotation, with a relaxation time of

$$\tau_B = \frac{3v\eta_0}{kT} \qquad (4.1)$$

where v is the particle-volume, η_0 the solvent viscosity, k the Boltzmann constant and T the temperature. For typical 10 nm colloids in a solvent with η_0=10^{-3} Pa·s, τ_B = 0.1 μs. The other mode is Néel rotation, which involves rotation of the magnetization with respect to crystal lattice of the magnetic colloid. For this process the relaxation time is:

$$\tau_N = f_0^{-1} \exp\left[\frac{K v}{kT}\right] \qquad (4.2)$$

where K is the (material-dependent) anisotropy constant, and f_0 is the Larmor frequency, about 10^9 s^{-1}. It is obvious, that the Néel relaxation time strongly depends on the particle volume. For example, the τ_N of magnetite colloids ($K = 1.1 \cdot 10^4$ Jm^{-3}) increases from 4 ns to 70 μs upon increasing the particle diameter from 10 nm to 20 nm.

4.5.1. Interactions between magnetic colloids

In principle a fluid of dipolar hard spheres can model the macroscopic behaviour of ferrofluids.
Because of the colloid's Brownian motion, the behaviour of a magnetic fluid is dictated by thermodynamics, with temperature and concentration as characteristics. Therefore, the system adopts a state or phase that minimizes its free energy. The anisotropic nature of magnetic interaction leads to a rich phase behaviour of magnetic fluids. For example, because magnetic interaction favours head-to-tail configurations of magnetic colloids, worm-like structures can be expected in dilute solutions of strongly interacting magnetic colloids [57]. In concentrated magnetic fluids, calculations suggest that strong interaction may lead to macroscopic parallel alignment of dipole moments, yielding a permanent magnet [58,59]. These two phases have not yet been found experimentally, and some question if the spontaneously magnetized liquid exists at all [60]. Another unresolved and actively debated issue is, if magnetic attraction can lead to a gas-liquid separation [61], i.e. spontaneous separation of an initially homogenous magnetic fluid into two fluids with different concentrations.
However, accounting for dipolar interactions has proven to be a difficult problem.
Interactions in ferrofluids can be experimentally investigated with magnetic susceptibility measurements. Much effort has been put in the measurement of the temperature-dependence

of the susceptibility [62,63]. Nonetheless, the investigation, if ferrofluids have, just as other ferromagnets, a Curie temperature, T_c, is an important issue [64-67] since it is the temperature above which a ferromagnetic material loses its permanent magnetism (for iron, T_c=768°C).
The probably most studied ferrimagnetic particles consisting of single domains are Fe_3O_4 particles with a diameter of about 10 nm [54]. All particles, which were studied in this theory, are grafted with oleic acid grafted onto their surfaces, which makes them soluble in organic solvents such as cyclohexane.
They can be considered as point dipoles with a magnetic moment, located at the centre of spherical domains, of

$$m = (\pi/6) \cdot M_{s,b} d_m^3 \tag{4.3}$$

where $M_{s,b}$ denotes the bulk saturation magnetization and d_m the diameter of the magnetic core.
The magnetic interaction between two particles with magnetic moments m_1 and m_2 at distance r_{12} (Figure 4.2) is

$$U_{dd} = \frac{\mu_0 m_1 m_2}{4\pi r_{12}^3} [\hat{m}_1 \hat{m}_2 - 3(\hat{m}_1 \cdot \hat{r}_{12})(\hat{m}_2 \cdot \hat{r}_{12})] \tag{4.4}$$

where the hat above symbols denotes a unit vector. In the energetically most favourable configuration, the magnetic moments point in the same direction and are laying head-to-tail. In addition to magnetic interaction, magnetic colloids also experience (isotropic) London-Van der Waals attraction. The Van der Waals attraction between Fe_3O_4 cores is [68]

$$U_{VDW} = -\frac{A}{12}\left[\frac{1}{s^2-1} + \frac{1}{s^2} + 2\ln\left(\frac{s^2-1}{s^2}\right)\right] \tag{4.5}$$

with A being the Hamaker constant (approximately 4.10-20 J for iron oxides in a solvent [68,69] and $s = r_{12}/d$.

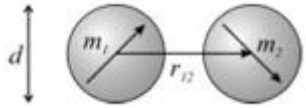

Figure 4.2. Interaction between two magnetic colloids.

Figure 4.3 shows that at closest approach (r = 14 nm) Van der Waals attraction is small (-0.1 kT), where dipole-dipole interaction is significant (-1.1 kT). Moreover, the range of dipole-dipole interaction strength between particles is much larger than that of Van der Waals interaction.
The thickness of the organic shell, not yet determined well, is often assumed to be about 2 nm.

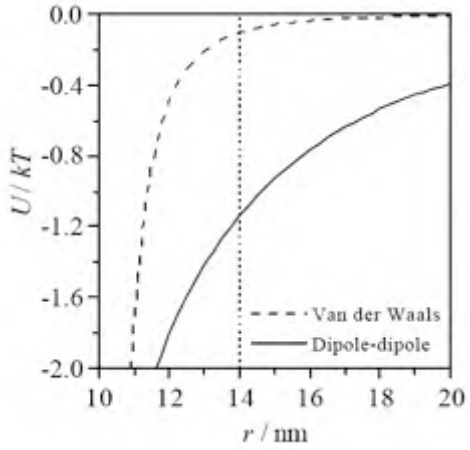

Figure 4.3. Distance-dependence of Van der Waals and maximum dipole-dipole interaction between two magnetic particles with a core diameter of 10 nm. The dotted line indicates the distance of closest approach.

In Figure 4.4 the Van der Waals and dipole-dipole interaction between touching particles is plotted for different particle sizes. The plot shows the weak Van der Waals interaction and dependence, in contrast to the strong dipolar dependence on particle size. Even for the largest particles, with a core of 15 nm, Van der Waals attraction remains weak (-0.27 kT). It has to be reminded, that the Van der Waals energies calculated here are based on just an assumed layer thickness of 2 nm. If

the layer is thinner, Van der Waals attraction will be much stronger than the estimated values.

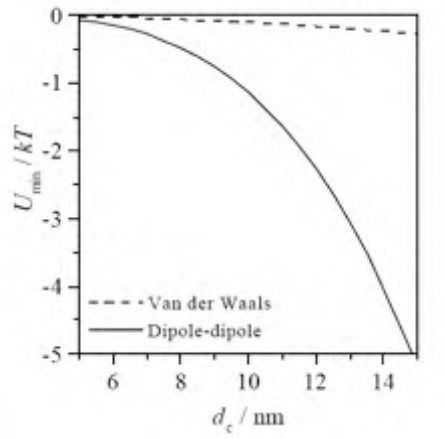

Figure 4.4. Size-dependence of Van der Waals and maximum dipole-dipole interaction between two touching magnetic particles. d_c is the diameter of the Fe_3O_4 core. The thickness of the oleic acid layer is taken 2 nm.

4.6. Poly(acrylamide)-based magnetic "nanosponges" [70]

4.6.1. Introduction

Nanocomposite materials have recently been shown to represent a powerful approach in the preparation of functional materials [71,72]. In particular, polymeric nanocomposites where a polymer matrix is combined with inorganic nanoparticles have gathered much attention during the past years [71,73-75]. The size and properties of polymers make them a convenient scaffold to disperse and arrange other nanoscaled objects to produce nanocomposites with enhanced properties. In particular, nanocomposites consisting of a polymeric network that embeds magnetic nanoparticles (MagNPs) represent a feasible approach in the preparation of magnetic gels [76-79]. In this context, the research of materials able to combine the peculiar properties of both permanent hydrogels and MagNPs is an important step in the formulation of smart functional materials.

In this work, we synthesized and characterized a gel that is able to load a large amount of water-based formulations, with a structure that can be modified and adapted to specific functions. In view of synthesizing a permanent hydrogel, where MagNPs are chemically connected to the network structure, basic requirements should be addressed. First, the gel structure should be capable to load as much water as possible. Therefore we choose an acrylamide-based gel formulation, as the water-loading properties of acrylamide are known to be very good. Second, in order to connect the acrylamide network to the MagNPs, we used a strategy similar to that previously reported by Gupta and Wells [80]. To this purpose, a polymerizable polyethylene glycol (PEG)-derivative was prepared by esterification of PEG with maleic anhydride (MA). The PEG backbone was chosen because of its hydrophylicity. The complete esterification with MA leads to the formation of a linear polymer where two carboxylic moieties are introduced at both endings of the chain, together with two double bonds that represent the polymerizable groups (see the Experimental Section for further details). The carboxylic groups are then used to link the MagNPs to the PEG-derivative: in fact, the binding reaction between MagNPs and carboxylic acids is well-known to take to a complete coupling of the carboxylic headgroup onto the

surface of the particles [81]. On the other hand, the double bonds were used to incorporate the MagNP-PEG adducts into the polyacrylamide gel network, which was obtained by polymerizing acrylamide and *N*,*N*'-methylene bisacrylamide. Following this approach, we successfully prepared nanocomposite materials that combine the properties of permanent hydrogels to those of magnetic responsive nanoparticles, called hereinafter nanomagnetic sponges. The structure was studied by using Small-Angle X-ray Scattering (SAXS) and Small-Angle Neutron Scattering of Polarized Neutrons (SANSPOL). Furthermore, we showed by scanning electron microscopy (SEM) that these nanomagnetic sponges can be used as active containers for water-based formulations. To this purpose we uploaded an oil-in-water microemulsion (μE) into the porous structure of the magnetic hydrogel and we showed that the μE can also be released in the presence of an external magnetic stimulus. An example of the potentialities of these new materials has been recently reported in the context of the Conservation of Cultural Heritage [78].

4.6.2. Experimental section

Nanomagnetic Gel Synthesis. As outlined in the Introduction, a PEG-derivative was properly synthesized to embed the MagNPs into the acrylamide gel structure. Chloroform (200 mL, HPLC grade, 99.9% purity, obtained from Aldrich, Milan) was deoxygenated through Argon purging for 15 min. Twenty grams of Polyethylene glycol (0.1 mol, $M_w \approx 200$ g/mol, Sigma, Milan) was added together with 19.6 g of MA (Sigma, Milan) still under Argon purging. The reaction was then carried out in the dark for 24 h at 37 °C. During the reaction, two ester bonds are formed as a result of the chemical reaction between the MA anhydride group and the hydroxyl groups of PEG (see Figure 5). Thereinafter, we will refer to the obtained product as MA-PEG-MA.
MagNPs were synthesized as already reported in detail elsewhere [82-86]. A stable ferrofluid consisting of positively charged $CoFe_2O_4$ nanoparticles dispersed in water was obtained. The concentration of nanoparticles was adjusted to 1% wt/wt to obtain the ferrofluid used throughout the rest of the synthesis (referred to as FF). The size and polydispersity of the nanoparticles agreed with a previous nanoparticle batch that was previously investigated [84], showing a mean

diameter of about 8 nm and a polydispersity of about 0.4.
A solution of MA-PEG-MA was prepared by dissolving 0.5 g in 10 mL of water. This solution was then added to the FF (5 mL, 0.5 g of MagNP), and the mixture was sonicated for 15 min (Eurosonic 22). In this step, as outlined in the Introduction, the carboxylic groups react with the surface of the nanoparticles to form a slightly viscous magnetic fluid (see Figure 4.5) [81].
Separately, a clear solution containing 0.75 g of acrylamide (Fluka, Milan, purity ≥99%) and 60 mg of *N*,*N*'-methylene bisacrylamide (Fluka, Milan, purity >98%) in 10 mL of water was prepared.
The acrylamide solution and magnetic fluid were then purged with N_2 and mixed together. Ammonium persulfate (Aldrich, Milan, purity >98%) was then added as a radical initiator, and the reaction was carried out at 42 °C for 4 h. Throughout the rest of the paper we will refer to the sample prepared by means of such procedure as MagGel. In order to check the effect of the stirring over the obtained gel structure, one sample was polymerized without any mixing (hereinafter referred to as NS-MagGel). A reference gel (RefGel) containing no MagNPs was prepared as well.
At the end of the polymerization, a magnetic black gel is obtained in the cases of the samples containing MagNPs, while the reference gel is slightly opalescent. Only in the case of gel prepared without stirring, phase separation was observed, with one fluid phase on top containing nonmagnetic particles and a gel-phase on the bottom containing almost the totality of magnetic particles. Pristine gels showed a pH ~1. In order to increase the pH, each gel was washed, at least 10 times, with a large excess of water (purified by a Millipore Organex system; $R \geq 18$ MΩ cm) until a pH ~ 4 was reached.
The stability of the hydrogels was checked by freeze-drying the hydrogels to xerogels and rehydrating them in an excess of water. Lyophilized gels return to the completely swollen state in a few minutes. As usual for permanent gels, this process can be repeated several times without any detectable change in the structure.
Similarly to a xerogel, the reference gel is a porous white powder, while gels containing cobalt-ferrite nanoparticles appear homogeneously black.

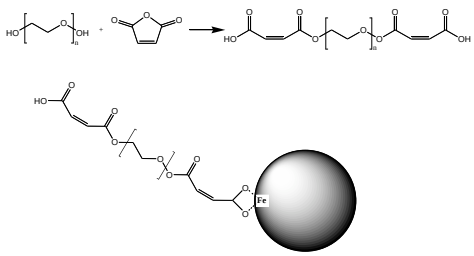

Figure 4.5. Scheme of the reaction between ethylene glycol and MA (top) and sketch of coupling between the surface of MagNP and the ethylene glycol dicarboxyl derivative (bottom) [70].

Dehydration Tests. In order to evaluate hydrophilic properties of the gels, a known amount of the freeze-dried xerogel was fully hydrated by dipping it in water for a few minutes. We found that, in both the reference and the magnetic gels, the maximum amount of loaded water was slightly higher than 90% by weight of the final hydrated sample. In order to investigate the differences between the gels' behavior, xerogels were first hydrated with a known amount of water (90 wt% of water, 10 wt% of freeze-dried powder). Then they were stored in a controlled humidity chamber (50% relative humidity), and their weight was checked during the following 30 days.

Thermal analysis. Thermogravimetric analysis was performed with an SDT Q600 apparatus (TA Instruments, Milan, Italy). The temperature range was 25–800 °C, with a scan rate of 20 °C/min. The run was performed with alumina pan and under a nitrogen flux of 100 mL/min.

Rheology. Oscillatory shear measurements were conducted on a Paar Physica UDS 200 rheometer working in controlled shear stress equipped with a 1° cone and plate geometry of 25 mm diameter. The dependence of the rheological parameters *G'*, *G''*, and η^* from the oscillation frequency (ω) was obtained from the phase lag between the applied shear stress and the related flow and from the ratio between the amplitudes of the imposed oscillation and the response of the gel. The complex viscosity is given by

$$\left|\eta^*(\omega)\right| = \sqrt{\frac{G'^2(\omega) + G''^2(\omega)}{\omega^2}} \qquad (4.6)$$

The storage modulus (*G'*) and the loss modulus (*G''*) were measured over the frequency range 0.001-50 s^{-1}. The values of the stress amplitude were checked by means of an amplitude sweep test in order to ensure that all measurements were performed within the linear viscoelastic region.
All the samples were equilibrated for 1 h at 20 °C before the experiments. All the measurements were performed at a temperature of 20.00 ± 0.01 °C (Peltier temperature control system).
With regards to the gel preparation, it is important to state that is impossible to finely tune the water content in the investigated samples: in fact, when the conically shaped measurement head approaches the gel deposited onto the plate, the material is partially squeezed out from the head-plate gap and, at the same time, a minimum amount of water is released from the gel network. This makes it impossible to exactly know the real water content. Nevertheless, in order to make the measurements reliable, we always used the same amount of fully hydrated sample on the plate, and we always maintained the same measurement conditions. All measurements were repeated at least five times in order to obtain a good reproducibility.

SANSPOL. SANSPOL measurements were carried out to investigate the nanostructure of the magnetic gel. In this particular case, the xerogel sample was rehydrated with D_2O (Eurisotop, Saclay, France) in order to maximize the contrast between the "solvent" and the gel network and to minimize the incoherent background contribution. SANSPOL experiments were performed at the V4 instrument at the BERII reactor of the Hahn-Meitner Institute, Berlin.
A horizontal magnetic field (about 1 T) was applied at the sample position, oriented perpendicularly to the incoming neutrons. Polarized neutrons are provided by a transmission polarizing supermirror cavity. The polarization direction is reversed using a spin flipper in front of the sample. Data were reduced to absolute intensities according to the conventional method used at HMI by using the BerSANS-PC software package [87].

SAXS. The measurements were carried out with a Nanoviewer (Rigaku), equipped with a Mercury70 Charge Coupled Device detector (1024x1024 pixels, pixel dimension: 68 μm). Cu K_α radiation (λ=1.5418 Å) was provided by a Micromax007 X-ray rotating anode (Rigaku),

operating at a maximum power of 0.8 kW with a focal spot diameter of 70 μm. X-rays were conditioned using a Confocal Max-Flux Mirror (Rigaku/Osmic) in order to totally remove the Cu K_β maintaining the high flux and symmetry of the rotating anode source. X-ray collimation was performed through a three-point collimation system. The sample-to-detector distance was about 605 mm. The volume between the sample and the detector was kept under vacuum during the measurements to minimize scattering from the air. The Q-range was calibrated using silver behenate, which is known to have a well-defined lamellar structure (d=58.48 Å) [88] where the scattering vector Q is defined as $Q=4\pi/\lambda \sin(\theta/2)$, with θ being the scattering angle. Scattering curves were monitored in a Q-range from 0.01 to 0.3 $Å^{-1}$. The gel samples were filled into a demountable solid samples holder consisting of two thin Kapton windows and a 1 mm stainless steel spacer. The experimental temperature (25 °C) was controlled by a Peltier element, with an accuracy of ± 0.1 °C. All two-dimensional (2D) spectra were corrected for the dark current, and a dezingering procedure was applied to all images in order to remove spurious signals. The empty cell contribution (Kapton windows) was subtracted using the empty cell/sample transmission ratios. Finally, 2D spectra were azimuthally averaged in order to obtain the correspondent one-dimensional (1D) scattering intensity distribution.

SEM. SEM observations were carried out by means of a Cambridge Stereoscan 360S, working at 25 kV of acceleration potential, with a working distance of 25 mm. Few milligrams of the xerogel were deposited onto the stub and coated with a gold film (Agar automatic sputter coater) in order to make the sample conductive.

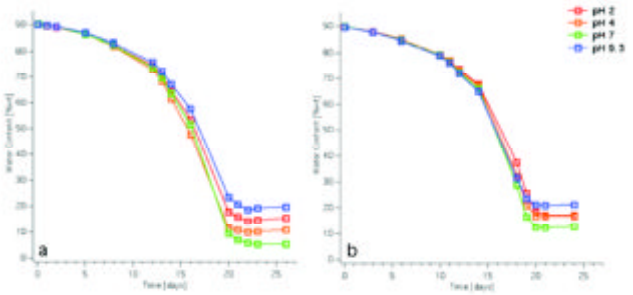

Figure 4.6. Dehydration curves of samples RefGel (a) and MagGel (b) at different pH values.

Table 4.1. Final water content values for the gel and three different pH values.

	water [% w]			
sample	pH 2	pH 4	pH 7	pH 9
RefGel	15.6	11.1	5.6	20.0
MagGel	17.0	16.6	12.6	20.9

4.6.3. Results and discussion

Dehydration Behavior. Dehydration curves are shown in Figure 4.6 for RefGel (a) and MagGel (b). As the gels have a polyelectrolyte nature (amidic and carboxylic groups are present in large amount), the dependency of the dehydration behavior against the pH was considered. Four different pH values were investigated: 2, 4, 7, and 9.3 (pH was adjusted by washing the gel in NaOH water solution). We note that all the dehydration curves show a similar behavior, with a nearly linear water loss during the first 10 days, followed by a faster decrease during the next week, ending in a plateau after about 20 days. The presence of MagNPs only slightly changes the water retention properties of the gel structure that can be evidenced in the final part of the curves (see Table 4.1).
Let us first discuss the behavior of the sample RefGel. It is well-known that the swelling properties of polyacrylamide-based gel [89] dramatically depend on the pH: in particular, the gel structure at neutral pH is largely more swollen than at acid or alkaline pH. On the other hand, the water still bound to the gel network after about 1 month consists of molecules trapped in smaller pores, since most of the water has been already released from the large pores. One should expect that pores size is strictly related to the swollen degree of the gel (that, in the present case, depends on the pH) and, consequently, the lower amount in the final water content fairly explains the results found at pH 7, that is, the pH where the gel is more swollen.
MagNPs introduced in the gel structure influence the water retention properties depending on the pH. At pH 2 and 9.3, the samples show quite similar values, while at pH 4 and, in particular, at pH 7, a clear dependency on the MagNP content is present. This is due to the “structuring effect” of the nanoparticles over the gel structure: i.e., each nanoparticle acts as an anchoring point for the PAAm/PEO. The part of the gel located in the proximity of the particles cannot be swollen as in the reference gel. As a consequence, the size of

the pores situated in these regions is not really affected by the pH, since their local structure is dictated by steric constrictions. It is important to stress that this effect can not be ascribed to a charge effect of the nanoparticles: in fact, the point of zero charge (PZC) of the MagNP surface is around pH 7 [90]. Moreover, the MagNP surface is coated with the carboxylic acid moieties during the condensation reaction.

SANSPOL. More insight into the nanocomposite gel structure was obtained through SANSPOL experiments. This technique has already been proven very useful to explore MagNPs [84,85,91-94].
The sample investigated by SANSPOL was prepared as described for sample MagGel in the Experimental Section, freeze-dried, and then the xerogel was rehydrated with fully deuterated water (80% by weight of D_2O, 20 wt % of gel powder).
In Figure 4.7 (top) the results for the nonpolarized intensity are shown, while, in the bottom, the SANSPOL intensities are shown together with the fitting results. The scattering behavior of gels formed from gelatin has been deeply investigated in the past [95-98]. It has been shown that the total intensity arising from a gelatin can be considered as the sum of two contributions (see below). In our case, because of the presence of MagNPs, a third component should be considered:

$$I(Q)=I_{Lorentz}(Q)+I_{excess}(Q)+I_{MagNP}(Q)+bkg \qquad (4.7)$$

where bkg is the incoherent background.
The scattering intensity due to the MagNPs ($I_{MagNP}(Q)$) was modeled according to the formalism introduced by Bartlett and Ottewill for polydisperse spherical particles [99]. In this approach, the particles are described as spherical objects with a Schultz distribution of radii [100,101]. (More details about the fitting procedure in the Appendix). The parameters obtained from the fitting are the volume fraction of the MagNPs, their average radius and polydispersity, and both particles' nuclear and magnetic scattering length densities (SLDs).
The Lorentzian component can be described as:

$$I_{Lorentz}(Q) = \frac{I_{Lorentz}(0)}{1+Q^2\xi^2} \qquad (4.8)$$

where $I_{Lorentz}(0)$ is the Lorentzian intensity at $Q=0$, Q is the

scattering vector, and ξ is the mesh size of the gel network.
According to the Debye-Bueche theory [96] an excess scattering term has to be introduced to account for the inhomogeneities [98]:

$$I_{excess}(Q) = \frac{I_{excess}(0)}{\left(1 + Q^2 a^2\right)} \tag{4.9}$$

where $I_{excess}(0)$ is the Debye-Bueche intensity at Q=0, and a is the inhomogeneity domains' size.
As mentioned in the Experimental Section, the SANSPOL technique allows the separation of the nuclear and magnetic contributions to the scattering intensity. In the case of our gel, the magnetic content is quite low, as only 20 wt% consists of polymer and magnetic particles. This is consistent with the small variations between the nonpolarized and the flipper ON and OFF polarized intensities (see Figure 4.7). Nevertheless, this small variation allows for the simultaneous fitting of the structural parameters of both the MagNPs and the gel network.

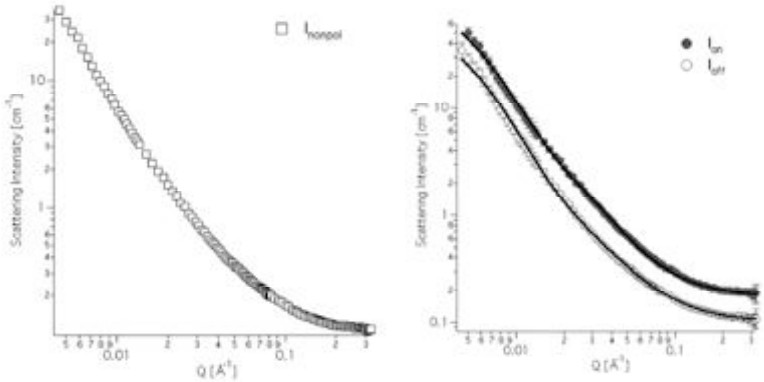

Figure 4.7. SANS (left) and SANSPOL (rigth) intensities of the MagGel sample together with the fit results (black solid lines). For the sake of clarity, in the bottom panel, I_{on} and the relative fit were offset by 5 cm^{-1}.

Table 4.2. Parameters resulting from the simultaneous fit of SANSPOL and SAXS intensities.

Structure	Parameter	SANSpol results	SAXS results
MagNP	Volume fraction	$0.00227 \pm 9.9 \times 10^{-5}$	
	Average radius	38.6±1.4 Å	36.7±0.3 Å
	Polydispersity	0.419±0.004	0.498±0.042
	Nuclear/atomic SLD	$5.77 \times 10^{-6} \pm 0.3 \times 10^{-8}$ Å^{-2}	3.98×10^{-5} Å^{-2}
	Magnetic SLD	$6.8 \times 10^{-7} \pm 2 \times 10^{-8}$ Å^{-2}	
gel	I_0 Lorentz	1.21±0.05 cm^{-1}	
	ξ	42.8±9.8 Å	42.8±17.7 Å
	I_0 excess	63.1±7.4 cm^{-1}	
	a	158.4±9.0 Å	149.0±22.3 Å
	Solvent SLD	$6.36 \times 10^{-6} \pm 9 \times 10^{-8}$ Å^{-2}	9.33×10^{-6} Å^{-2}
	Incoherent bkg	0.1009±0.0006 cm^{-1}	

The fitting results reported in Table 4.2 show that the size distribution of the MagNPs, as well as both the magnetic and the nuclear SLDs, are in very good agreement with previously published results [84]. Furthermore, the MagNPs volume fraction is consistent with the concentration of nanoparticles as obtained by thermogravimetric analysis indicating that the nanoparticles are homogeneously distributed into the gel matrix. Two weight losses are clearly visible (Figure 4.8): the first one due to water evaporation and the second one due to the burning of the organic matrix of the gel. Therefore, the constant residual weight from 700°C can be ascribed to the solid metallic content of the gel, equal to 0.65 %wt as inferred from TGA data analysis.
The mesh and inhomogeneity domain size of the gel structure are about 4 and 16 nm, respectively. These values show a very good agreement with previously reported results for similar kind of gelatin structures [97,98] confirming that the investigated samples consist of a gel matrix where the MagNPs are embedded and distributed thoroughly the gel matrix.

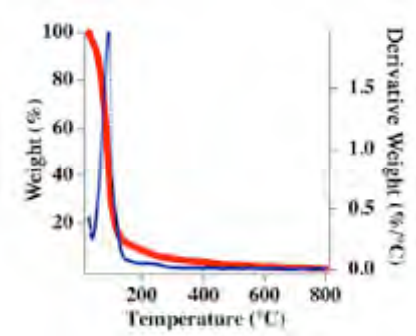

Figure 4.8. TGA plot of the hydrated gel; continuous line, sample weight; markers, derivative weight.

SAXS. The nanocomposite structure of the nanomagnetic gel was also investigated by means of SAXS. The sample was the same one used for SANSPOL analysis, but H_2O was used instead of D_2O. In the SAXS experiment, the electronic density of the nanoparticles is so high (with respect to both water and the gel structure) that the scattering arising from them nearly overrules all the other contributions, that is, only the nanoparticles can be seen. SAXS intensity distribution is shown in Figure 4.9, together with the curve obtained by fitting experimental results according to the same model used for the SANSPOL data. Furthermore, SANSPOL results were used as starting values in the SAXS fitting procedure. The parameter values resulting from the fit are reported in Table 4.2, showing a very good agreement with results obtained by SANSPOL.

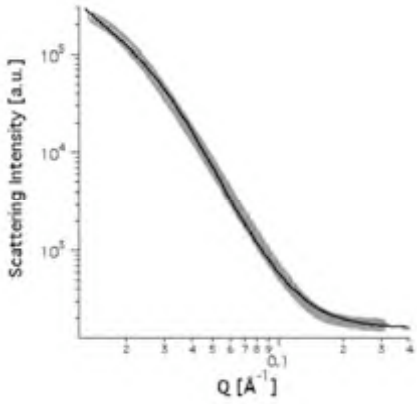

Figure 4.9. SAXS curve (gray circles) of the MagGel sample together with the fit result (black solid line).

Since SAXS results are in arbitrary units, the values of

MagNP volume fraction, I_0-*Lorentz*, I_0-*excess*, and incoherent background, are meaningless parameters, while the SLD values were fixed according to their theoretical values for X-rays. The results obtained by SAXS, reported in Table 4.2, are in excellent agreement with those obtained from SANSPOL and confirm both the geometrical features of the nanoparticle and their distribution into the gel.

Rheology. The rheological properties of samples RefGel and MagGel were investigated. In order to ensure that all measurements were performed within the linear viscoelastic region, the values of the stress amplitude were checked by means of an amplitude sweep test. Figure 4.10 shows amplitude sweep results for samples RefGel and MagGel at an angular frequency of 1 s^{-1}.
Considering that the storage modulus *G'* and the loss modulus *G''* are independent from the applied strain above a critical value of almost 1%, it is possible to apply the linear viscoelasticity theory to analyze the results.
Dynamic mechanical properties of samples RefGel and MagGel were investigated by frequency sweep oscillation tests. Figure 4.11 shows the storage modulus *G'*, the loss modulus *G''*, and the complex viscosity η^* dependency on the frequency at a constant strain of 5%. The storage modulus of the RefGel sample is always larger than the loss modulus, and no crossover between the *G'* and *G''* curves is observed within the range of the accessible frequencies; this behavior is typical of solid-like materials with infinite relaxation time. Furthermore, Figure 4.11 indicates that, while *G'* is almost constant, *G''* shows a minimum at intermediate frequencies. Upon the addition of the MagNPs, the relative trend of the shear moduli remains almost the same, but their values increase. In particular, a more elastic response is observed: the *G'* average value passes from almost 80 Pa for the reference sample to almost 200 Pa for the MagGel sample. This trend is the same observed in the amplitude sweep measurements.

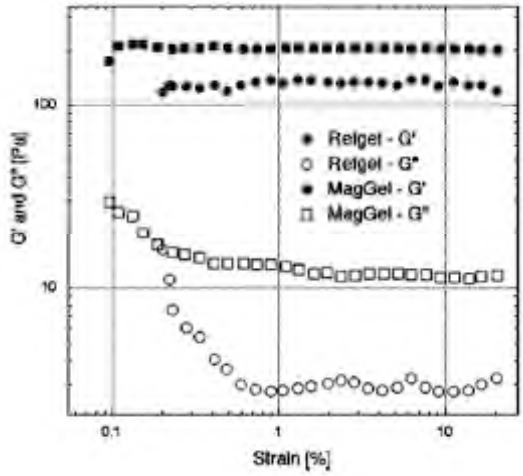

Figure 4.10. Amplitude sweep results for samples RefGel and MagGel at an angular frequency of 1 s^{-1}.

More than discussing the absolute values, it is important to stress that the reference and nanocomposite gels show very similar viscoelastic behavior, indicating that the rheological properties are very similar. Furthermore, being for both the investigated samples the *G'* values almost independent from the frequency of the applied stress, the average values of *G'* can be considered equal to the intrinsic elastic shear modulus of the gel *G* [102] and we can correlate *G* to the entanglement density ρ_e as follows: $G = \rho_e k_B T$. An increase in the elastic modulus *G'* values indicates an increase in the entanglement density induced by the nanoparticles, even if the rheological behavior remains very similar [103]. This effect can be attributed to the anchoring of the PAAm/PEO chains to the MagNP's surface, which plays the role of "entanglement sites" and increases the structure of the gel.
As introduced in the Experimental Section, even if the rheology results cannot be quantitatively discussed because of the sample preparation procedure, it is possible to conclude that the viscoelastic properties of the reference gel are qualitatively retained in the nanocomposite gel where the nanoparticles loading induces an increase of the strength of the 3D network, further confirmed by the increase of the complex viscosity η^* (for the MagGel is almost double the RefGel).

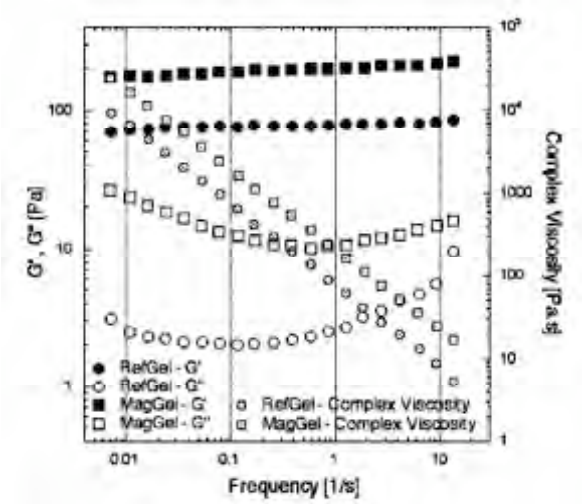

Figure 4.11. Storage moduli *G'*, the loss moduli *G''*, and the complex viscosities η^* dependency on the frequency at a constant strain of 5% for samples RefGel and MagGel.

SEM. Two representative SEM pictures are shown in Figure 4.12. The presence of the MagNPs (very electron-rich) is responsible for the brightest parts of the images. These nanoparticle aggregates are also identifiable by the irregular shape, while the pure gel appears as darker gray areas (less electron-rich) with a smooth surface. The structure is very porous, with pores having diameter from hundreds of nanometers to several microns. Note that this porous structure enables this material to work as a "container" for other substances such as, for example, solutions or μEs [8].

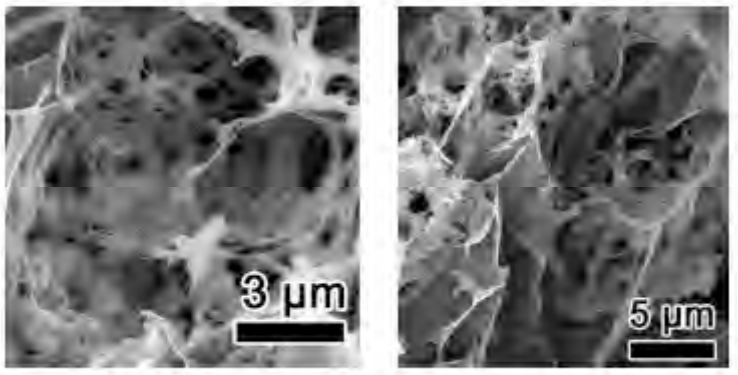

Figure 4.12. SEM micrographs of the MagGel sample at two different magnifications.

Microemulsions. In order to demonstrate the efficiency of these nanomagnetic sponges to act as containers for water-based formulations, we uploaded a μE widely used in the cleaning of damaged works of art [104,105]. The μE was prepared as previously described [104,105] and it was then uploaded simply by dipping the MagGel xerogel in the μE. The μE was finally recovered from the μE-loaded MagGel by applying an anisotropic magnetic field with the aid of a permanent magnet (maximum field ca. 1.44 T).
In the presence of a magnetic field, the MagGel shrinks as a result of its magnetic nature, releasing its liquid content. Both the μEs (before uploading and after recovery) were studied by means of SAXS to verify whether the μE maintains its nanostructure or the preferential adsorption of its constituents to the gel suprastructure destroys it. Figure 4.13 shows the results, together with the fitting obtained according to a model introduced by Chen and co-workers [106]. Without going into the fitting details (see Appendix), the μE is modeled as electrostatically charged polydisperse core-shell spheres (t being the thickness of the shell, r_c being the average radius of the core, and Z being the effective charge number per micelle). According to the values of the coefficients resulting from the fit (see Table 4.3), the two μEs (before the uploading and after the recovery) are almost identical. The only difference is the slight decrease in the size of the core radius after recovery.

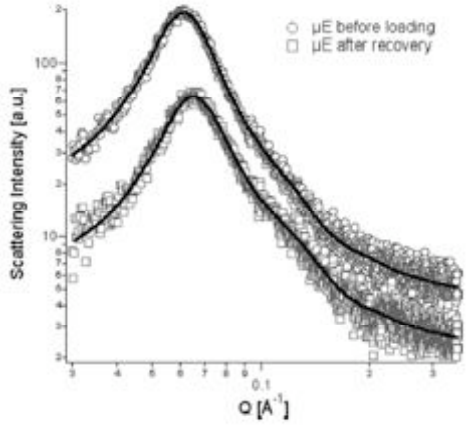

Figure 4.13. SAXS curves of the μE before uploading it on MagGel and after its recovery. Curves resulting from the fitting routine are shown as solid lines. For the sake of clarity, both experimental data and fitting

results are offset (+50 au).

Table 4.3. Parameters resulting from the fit of SAXS intensitie on μEs.

Coefficient	Before loading	After recovery
Rc core radius	28.8±1.4 Å	25.3± 2.4 Å
Core polydispersity	0.28±0.01	0.29±0.03
t, shell thickness	5.3±0.5 Å	5.7±0.9 Å
Z, micellar charge	28.1±1.3	27.4±2.7

This is probably due to the weak interaction between the organic part of the μE (i.e., the solvents constituting the droplets) and the hydrophobic regions of the gel. This corresponds to a decrease in the hydrophobic content of the μE, which is expected to produce a decrease in the droplets' size.

4.6.4. Conclusions

In this paper we report the formulation and the characterization of a nanomagnetic sponge where the mechanical and hydrophilic properties of acrylamide gels are combined with the magnetoresponsive properties of MagNPs. A linear linker consisting of an ethylene glycol core, a carboxylic group at each extremity of the linker, and two polymerizable anchor points was synthesized by coupling PEG and MA. Such a linear linker was used to embed the MagNPs into the acrylamide-based gel network.

The nanocomposite sponge was studied by means of SAXS and SANSPOL. In particular, this last technique is extremely well-suited in the characterization of nanoscaled magnetic objects and allowed us to reveal both the gel structure and the nanoparticle arrangement within.

The mechanical properties of this novel nanocomposite material were investigated by means of rheological measurements, showing that the viscoelastic properties of acrylamide gels are qualitatively retained in the nanomagnetic gel, where the presence of nanoparticles only induces an

increase in the mechanical strength of the 3D network. Hydrophilic properties were also studied, demonstrating that the magnetic nanosponge can be efficiently used to load a large amount of water: in fact, the nanocomposite gel can be used to load water-based formulations up to about 9 times its dry weight. This is made possible thanks to its highly porous structure, as shown by the SEM results. Moreover, the magnetic sponge can be magnetically squeezed, dried, and swollen again.

Finally, it is important to emphasize that such nanomagnetic gel structure opens up new perspectives in the use of smart materials in applications where water-based formulations must be locally and selectively applied and cleanly removed. Here, the uploading and recovery of an oil-in-water μE was studied, showing the effectiveness of such a nanomagnetic sponge as an active container. In particular, we have already shown how this approach can be successfully applied in the cleaning of works of art [78].

This new nanomagnetic gel is a clear example of how the bottom-up approach represents a powerful tool in the design of materials with enhanced functionalities.

4.6.5. Appendix

Small Angle Scattering Fitting Procedure used for the nanocomposite samples.

For polarized neutrons, where the neutron spins are aligned anti-parallel (+) or parallel (-) to the magnetic field vector **H**, the scattering cross-sections depend on the polarization of the incident neutrons $I^{+}(Q)$ and $I^{-}(Q)$, respectively. The scattering intensity relationships (denoted here as SANSPOL) has been previously derived [107,108] When the magnetic moments and neutron polarization are fully aligned along the external field, the SANSPOL intensities perpendicular to the applied field are given for the two states by:

$$I^{-,+}(Q\perp H) \propto [P_N \pm P_M]^2 S(Q) \tag{4.10}$$

where P_N and P_M represents the nuclear and magnetic form factors, respectively, and $S(Q)$ is the inter-particle structure factor. The arithmetic mean of the parallel and anti-parallel intensities perpendicular to the applied field corresponds to the cross-section for un-polarized neutrons:

$$[I^{-}(Q\perp H) + I^{+}(Q\perp H)]/2 = I^{unpol}(Q\perp H) \propto [P_N^2 \pm P_M^2] S(Q) \tag{4.11}$$

The scattering cross-section parallel to **H** is independent of the polarization state since it depends from pure nuclear contrast and is given by:

$$I(Q//H) \propto P_N^2 S(Q) \tag{4.12}$$

The difference between the two intensities represents a magnetic-nuclear cross term, allowing the magnetic contrast with respect to the nuclear contrast to be determined:

$$I^{-}(Q,\alpha) - I^{+}(Q,\alpha) \propto P_N P_M S(Q) \qquad (4.13)$$

where α is the azimuth angle between the magnetic field vector **H** and the scattering vector **Q** (**Q** = $\mathbf{k_i}$ - $\mathbf{k_s}$), where $\mathbf{k_i}$ and $\mathbf{k_s}$ are the incident and scattered wave vectors, respectively).

Both the perpendicular and the parallel intensities have been calculated in two separate ways, obtaining identical results: i) by adjusting the 2-D pattern to the $\sin^2\alpha$ dependence, and ii) by averaging the 2-D pattern only over sectors with a width of 5º respectively centred at α=90° and 270º for the perpendicular intensities, and centred at α = 0° and 180º for the parallel intensities. As expected, the parallel intensities for the two flipper states resulted identical: in fact, as indicated by eq 4.13, these intensities account only for the nuclear scattering.

SANSPOL results on the magnetic gel have been fitted according to the following equation:

$$I(Q) = I_{Lorentz}(Q) + I_{excess}(Q) + I_{MagNP}(Q) + bkg \qquad (4.14)$$

where bkg is the incoherent background.

The only contribute that is dependent on the magnetization is $I_{MagNP}(Q)$.

The Lorentzian component can be described as:

$$I_{Lorentz}(Q) = \frac{I_{Lorentz}(0)}{1 + Q^2\xi^2} \qquad (4.15)$$

where $I_{Lorentz}(0)$ is the Lorentzian intensity at Q=0, Q is the scattering vector, and ξ is the mesh size of the gel network.

According to the Debye-Bueche theory [109] an excess scattering term has to be introduced to account for the inhomogeneities due to strand-strand interactions [110]:

$$I_{excess}(Q) = \frac{I_{excess}(0)}{\left(1 + Q^2 a^2\right)} \tag{4.16}$$

where $I_{excess}(0)$ is the Debye-Bueche intensity at Q=0 and a is the inhomogeneity domains' size.
The scattering intensity due to the MagNPs ($I_{MagNP}(Q)$) was modeled according to the formalism introduced by Bartlett and Ottewill for polydisperse spherical particles [111]. In this approach, the particles are described as spherical objects with a Schultz distribution of radii [112,113]. The contribute to the total scattering intensity arising from these objects was calculated according to the following equations:

$$P(Q) = \frac{1}{V_p}\int_0^\infty G(r_c)F^2(Qr_c)dr \tag{4.17}$$

$$F(Qr_c) = \frac{4\pi}{Q^3}(\rho_{shell} - \rho_{core})\left\{\rho_{scaled}\, j\left(Qr_c + \frac{t}{r_c}Qr_c\right) - j(Qr_c)\right\} \tag{4.18}$$

$$\rho_{scaled}=(\rho_{solv}-\rho_{shell})(\rho_{core}-\rho_{shell}) \tag{4.19}$$

$$j(Qr_c)=sin(Qr_c)-(Qr_c)cos(Qr_c) \tag{4.20}$$

where r_c is the core radius, t is the shell thickness, V_p is the particle volume, and ρ_{core}, ρ_{shell} and ρ_{solv} are the scattering length densities (SLDs) of core, shell and solvent, respectively.

The function $G(r_c)$ is the normalized probability of finding a particle with a core radius between r_c and r_c+dr_c, and it accounts for the polydispersity of the cores according to a Schultz distribution [112,113]:

$$G(r_c) = \frac{r_c^z}{\Gamma(Z+1)}\left(\frac{Z+1}{\langle r_c \rangle}\right)^{Z+1} \cdot \exp\left[-\frac{r_c}{r_{avg}}(Z+1)\right] \qquad (4.21)$$

where $\Gamma(Z+1)$ is the gamma function and the parameter Z is related to the polydispersity σ_c of the core radius by the expression:

$$\sigma_c = \frac{\sqrt{\langle r_c^2 \rangle - \langle r_c \rangle^2}}{\langle r_c \rangle} = \frac{1}{\sqrt{Z+1}} \qquad (4.22)$$

The fitting routine has been constrained to globally fit all the SANSPOL curves for each sample: i.e. the fitting parameters are the same for the SANSPOL intensities parallel and perpendicular (flipper ON and OFF) to the magnetic field, excepted for the core scattering length density that changes as a function of the polarization of the neutrons and the angle between **Q** and **H**. This is summarized in Equation 4.23 where the nuclear part of the core scattering length density is the same for all the SANSPOL intensities, while the magnetic contribution is null for the parallel direction and it has the same value for the two perpendicular curves:

$$\rho_{core} = \rho_{core}^{nucl} \pm \rho_{core}^{mag} \qquad (4.23)$$

Small Angle Scattering Fitting Procedure used for the microemulsion, before the uploading into the nanosponge and after the recovery.

In the fitting model we assume the microemulsion as composed of polydisperse coreshell spheres with a mean aggregation number, N_{agg}, and an effective charge Z. The external hydrophilic shell having dimension t is formed mainly by the SDS polar heads, the OH groups of the 1-pentanol molecules, the first methylene group of both 1-pentanol and SDS [114], the hydration water, and a fraction of counterions. The hydrophobic core of spherical shape, with

a radius rc, contains the surfactant hydrocarbon tails (i.e. $C_{11}H_{23}$ and C_4H_9 of SDS and 1-pentanol respectively) and the molecules of p-xylene and nitrodiluent.
Within these assumptions the scattering intensity can be written as [115]:

$$I(Q) = A\,\phi\,P(Q)S(Q) + bkg \qquad (4.24)$$

where A is a constant accounting for the instrumental factor (intensities are not in absolute scale), ϕ is the microemulsion volume fraction, $P(Q)$ is the averaged intraparticle structure factor for polydisperse spherical particles as already described by eqs 4.18-4.22 considering the SLD profile in the microemulsion case, $S(Q)$ is the averaged center interparticle structure factor, and *bkgb* the instrumental background.

$$S(Q) = 1 + \frac{\langle F(Qr_c)\rangle^2}{\langle F(Qr_c)^2\rangle}\left[S_{MM}(Q) - 1\right] \qquad (4.25)$$

where $\langle F(Qr_c)\rangle$ represents an average over the size distribution and $S_{MM}(Q)$ has been calculated, as described by Liu et al. [115] by solving the Ornstein-Zernicke equation for the pair correlation function within the non-additive radius multicomponent mean spherical approximation closure that yields analytical solutions. For each sample the adjustable parameters were the core radius r_c, the shell thickness t, the micellar charge Z and the background contribution *bkg*; the amplitude A was assumed to be equal for all the samples so that the two scattering curves have been simultaneously fitted under this constraint. In the case of the microemulsion before the incorporation in the gel the volume fraction has been calculated by its chemical composition. After the recovery from the gel this parameter has been left free to vary.

Table 4.4. Parameters resulting from the fit of the SAXS intensities on microemulsions.

Coefficient	Before Loading	After recovery

Volume fraction	0.150	0.134
Average core radius	28.8 Å	25.3 Å
Core polidispersity	0.283	0.293
Shell thickness	5.3 Å	5.7 Å
SLD core ($Å^{-2}$)	7.3×10^{-6}	7.3×10^{-6}
SLD shell ($Å^{-2}$)	1.11×10^{-5}	1.10×10^{-5}
SLD solvent ($Å^{-2}$)	9.37×10^{-6}	9.37×10^{-6}
Micellar charge	28.1	27.4
Monovalent salt (M)	0	0
Temperature (K)	298	298

4.7. Bibliography

[1] S. Chikazumi, S. Taketomi, M. Ukita, M. Mizukami, H. Miyajima, M. Setogawa, Y. Kurihara, *J. Magn. Magn. Mater*. **1987**, *65*, 245.

[2] A.-H. Lu, W. Schmidt, N. Matoussevitch, H. Bönnermann, B. Spliethoff, B. Tesche, E. Bill, W. Kiefer, F. Schüth, *Angew. Chem*. **2004**, *116*, 4403; Angew. Chem. Int. Ed. 2004, *43*, 4303.

[3] S. C. Tsang, V. Caps, I. Paraskevas, D. Chadwick, D. Thompsett, *Angew. Chem*. **2004**, *116*, 5763; *Angew. Chem. Int. Ed.* **2004**, *43*, 5645.

[4] A. K. Gupta, M. Gupta, Biomaterials **2005**, *26*, 3995.

[5] S. Mornet, S. Vasseur, F. Grasset, P. Verveka, G. Goglio, A. Demourgues, J. Portier, E. Pollert, E. Duguet, *Prog. Solid State Chem*. **2006**, *34*, 237.

[6] Z. Li, L. Wei, M. Y. Gao, H. Lei, *Adv. Mater*. **2005**, 17, 1001.

[7] T. Hyeon, *Chem. Commun*. **2003**, 927.

[8] D. W. Elliott, W.-X. Zhang, Environ. *Sci. Technol*. **2001**, *35*, 4922.

[9] M. Takafuji, S. Ide, H. Ihara, Z. Xu, *Chem. Mater*. **2004**, *16*, 1977.

[10] S. Neveu, A. Bee, M. Robineau, D. Talbot, *J. Colloid Interface Sci*. **2002**, *255*, 293.

[11] F. Grasset, N. Labhsetwar, D. Li, D. C. Park, N. Saito, H. Haneda, O. Cador, T. Roisnel, S. Mornet, E. Duguet, J. Portier, J. Etourneau, *Langmuir* **2002**, *18*, 8209.

[12] S. Sun, H. Zeng, *J. Am. Chem. Soc*. **2002**, *124*, 8204.

[13] S.-J. Park, S. Kim, S. Lee, Z. Khim, K. Char, T. Hyeon, *J. Am. Chem. Soc*. **2000**, *122*, 8581.

[14] V. F. Puntes, K. M. Krishan, A. P. Alivisatos, *Science* **2001**, *291*, 2115.

[15] Q. Chen, A. J. Rondinone, B. C. Chakoumakos, Z. J. Zhang, *J. Magn. Magn. Mater*. **1999**, *194*, 1.

[16] J. Park, K. An, Y. Hwang, J.-G. Park, H.-J. Noh, J.-Y. Kim, J.-H. Park, N.-M. Hwang, T. Hyeon, *Nat. Mater*. **2004**, *3*, 891.

[17] S. Sun, C. B. Murray, D. Weller, L. Folks, A. Moser, *Science* **2000**, *287*, 1989.

[18] E. V. Shevchenko, D. V. Talapin, A. L. Rogach, A. Kornowski, M. Haase, H. Weller, *J. Am. Chem. Soc*. **2002**, *124*, 11480.
[19] J. Lee, T. Isobe, M. Senna, *Colloids Surf. A* **1996**, *109*, 121.
[20] A. Bee, R. Massart, S. Neveu, *J. Magn. Magn. Mater*. **1995**, *149*, 6.
[21] T. Ishikawa, S. Kataoka, K. Kandori, *J. Mater. Sci*. **1993**, *28*, 2693.
[22] T. Ishikawa, T. Takeda, K. Kandori, *J. Mater. Sci*. **1992**, *27*, 4531.
[23] K. Kandori, Y. Kawashima, T. Ishikawa, *J. Colloid Interface Sci*. **1992**, *152*, 284.
[24] R. M. Cornell, P.W. Schindler, *Colloid Polym. Sci*. **1980**, *258*, 1171.
[25] A. L. Willis, N. J. Turro, S. O'Brien, *Chem. Mater*. **2005**, *17*, 5970.
[26] B. L. Cushing, V. L. Kolesnichenko, C. J. O'Connor, *Chem. Rev*. **2004**, *104*, 3893.
[27] S. S. Papell, US Patent 3215572, 1965.
[28] R. Massart, *IEEE Trans. Magn*. **1981**, 1247.
[29] K. Raj, R. Moskowitz, *J. Magn. Magn. Mater*. **1990**, *85*, 107.
[30] M. De Cuyper, M. Joniau, *Langmuir* **1991**, *7*, 647.
[31] A. Wooding, M. Kilner, D. Lambrick, *J. Colloid Interface Sci*. **1992**, *149*, 98.
[32] D. Zins, V. Cabuil, R. Massart, *J. Mol. Liq*. **1999**, *83*, 217.
[33] L. Shen, P. E. Laibinis, T. A. Hatton, *Langmuir* **1999**, *15*, 447.
[34] M. H. Sousa, F. A. Tourinho, J. Depeyrot, G. J. da Silva, M. C. F. L. Lara, *J. Phys. Chem. B* **2001**, *105*, 1168.
[35] R. M. Cornell, U. Schertmann, The Iron Oxides: Structure, Properties, Reactions, Occurrence and Uses, VCH, Weinheim, 1996.
[36] M. Wan, J. Li, *J. Polymer. Sci*. **1998**, *36*, 2799.
[37] M. D. Butterworth, S. A. Bell, S. P. Armes, A.W. Simpson, *J. Colloid Interface Sci*. **1996**, *183*, 91.
[38] P. Tartaj, M. P. Morales, T. Gonzalez-Carreno, S.

Veintemillas-Verdaguer, C. J. Serna, *J. Magn. Magn. Mater*. **2005**, *28*, 290.
[39] G. Barratt, Cell. Mol. *Life Sci*. **2003**, *60*, 21.
[40] L. A. Harris, J. D. Goff, A. Y. Carmichael, J. S. Riffle, J. J. Harburn, T. G. St. Pierre, M. Saunders, *Chem. Mater*. **2003**, *15*, 1367.
[41] A. F. Thunemann, D. Schutt, L. Kaufner, U. Pison, H. Möhwald, *Langmuir* **2006**, *22*, 2351.
[42] P. A. Dresco, V. S. Zaitsev, R. J. Gambino, B. Chu, *Langmuir* **1999**, *15*, 1945.
[43] J. Deng, X. Ding, W. Zhang, Y. Peng, J. Wang, X. Long, P. Li, A. S. C. Chan, *Polymer* **2002**, *43*, 2179.
[44] X. Xu, G. Friedman, K. Humfeld, S. Majetich, S. Asher, *Adv. Mater*. **2001**, *13*, 1681.
[45] C. R. Vestal, Z. J. Zhang, *J. Am. Chem. Soc*. **2002**, *124*, 14 312.
[46] Y. Wang, X. Teng, J.-S. Wang, H. Yang, *Nano Lett*. **2003**, *3*, 789.
[47] D. Farrell, S. A. Majetich, J. P.Wilcoxon, *J. Phys. Chem. B* **2003**, *107*, 11022.
[48] A. Dyal, K. Loos, M. Noto, S.W. Chang, C. Spagnoli, K. V. P. M. Shafi, A. Ulman, M. Cowman, R. A. Gross, *J. Am. Chem. Soc*. **2003**, *125*, 1684.
[49] R. Hirsch, E. Katz, I. Willner, *J. Am. Chem. Soc*. **2000**, *122*, 12053.
[50] I. Willner, E. Katz, *Angew. Chem*. **2003**, *115*, 4724; *Angew. Chem. Int. Ed*. **2003**, *42*, 4576.
[51] V. Salgueiriño-Maceira, M. A. Correa-Duarte, M. Farle, A. López-Quintela, K. Sieradzki, R. Diaz, *Chem. Mater*. **2006**, *18*, 2701.
[52] Y. Deng, W. Yang, C. Wang, S. Fu, *Adv. Mater*. **2003**. *15*, 1729.
[53] B. L. Frankamp, N. O. Fischer, R. Hong, S. Srivastava, V. M. Rotello, *Chem. Mater*. **2006**, *18*, 956.
[54] R. E. Rosensweig, '*Ferrohydrodynamics*', Cambridge University Press, Cambridge (1985).
[55] '*Magnetic fluids and applications handbook*', ed. B. Berkovski and V. Bashtovoy, Begel House Inc., New York (1996).
[56] E. Blums, A. Cebers, and M. M. Maiorov, '*Magnetic*

fluids', Walter de Gruyter, Berlin (1997).
[57] Bonini, M. ; Fratini, E. and Baglioni, P. *Mat. Sci. Eng. C* **2007**, *27* (5-8), 1377-1381.
[58] A.O. Tsebers, *Magnetohydrodynamics* **1982**, 18, 137.
[59] K. Sano and M. Doi, *J. Phys. Soc. Jpn.* **1983***, 52*, 2810.
[60] L. Onsager, *J. Am. Chem. Soc.* **1936***, 58*, 1486.
[61] A.K. van Helden and A. Vrij, *J. Colloid Interface Sci.* **1980***, 78*, 312.
[62] F. Söffge and E. Schmidbauer, *J. Magn. Magn. Mater.* **1981***, 24*, 54.
[63] K. O'Grady, J. Popplewell, and S. W. Charles, *J. Magn. Magn. Mater.* **1983***, 39*, 56.
[64] K. O'Grady, A. Bradbury, S. W. Charles, S. Menear, J. Popplewell, and R. W. Chantrell, *J. Magn. Magn. Mater.* **1983***, 31-34*, 958.
[65] J. Popplewell, B. A. Aisheh, and N. Y. Ayoub, *J. Appl. Phys.***1988***, 64*, 5852.
[66] M. Holmes, K. O'Grady, and J. Popplewell, *J. Magn. Magn. Mater.* **1990***, 85*, 47.
[67] H. D. Williams, K. O'Grady, S. W. Charles, and K. J. Davies, *J. Magn. Magn. Mater.* **1993***, 122*, 134.
[68] P. Scholten, J. Magn. Magn. Mater.**1983**, 39, 99.
[69] D. Y. C. Chan, D. Henderson, J. Barojas, and A. M. Homola, IBM. J. Res. Develop. **1985**, 29, 11.
[70] M. Bonini, S. Lenz, E. Falletta, F. Ridi, E. Carretti, E. Fratini, A. Wiedenmann and P. Baglioni, *Langmuir* **2008**, *24* (21) 12644-12650.
[71] Mark, J. E. *Acc. Chem. Res*. **2006**, *39*, 881–888.
[72] Hussain, F.; Hojjati, M.; Okamoto, M.; Gorga, R. E. *J. Compos. Mater.* **2006**, *40*, 1511–1575.
[73] Bourgeat-Lami, E. *J. Nanosci. Nanotechnol*. **2002**, *2*, 1–24.
[74] Shenhar, R.; Rotello, V. M. *Acc. Chem. Res*. **2003**, *36*, 549–561.
[75] Pomogailo, A. D.; Kestelman, V. N. Metallopolymer Nanocomposites; Springer Verlag: Berlin, 2005.
[76] Francois, N. J.; Silvia, S. A.; Jacobo, E.; Daraio, M. E. *J. Appl. Polym. Sci*. **2007**, *105*, 647–655.
[77] Millan, A.; Palacio, F.; Snoeck, E.; Serin, V.; Lecante, P. In Polymer Nanocomposites; Mai, Y.-W., Yu, Z.-Z.,

Eds.; Woodhead Publishing Limited: Cambridge, U.K., 2006.
[78] Bonini, M.; Lenz, S.; Giorgi, R.; Baglioni, P. *Langmuir* **2007**, *23*, 8681–8685.
[79] Hernández, R.; López, G.; Lópeza, D. *J. Mater. Res*. **2007**, *22*.
[80] Gupta, A. K.; Wells, S. *IEEE Trans. Nanobiosci*. **2004**, *3*, 66–73.
[81] Sartoratto, P. P. C.; Neto, A. V. S.; Lima, E. C. D.; Rodrigues de Sá, A. L. C.; Morais, P. C. *J. Appl. Phys*. **2005**, *97*, 10Q917.
[82] Massart, R. C. R. Hebd. Seances Acad. Sci., Ser. C **1980**, 291, 1–3.
[83] Massart, R. *IEEE Trans. Magn.* **1981**, *17*, 1247–1248.
[84] Bonini, M.; Wiedenmann, A.; Baglioni, P. *J. Phys. Chem. B* **2004**, *108*, 14901–14906.
[85] Bonini, M.; Wiedenmann, A.; Baglioni, P. *Physica A* **2004**, *339*, 86–91.
[86] Bonini, M.; Wiedemann, A.; Baglioni, P. *Mater. Sci. Eng. C: Biomimetic Supramol. Syst.* **2006**, *26*, 745–750.
[87] Keiderling, U. *Appl. Phys. A: Mater. Sci. Process.* **2002**, *74*, s1455-s1457.
[88] Blanton, T.; Huang, T. C.; Toraya, H.; Hubbard, C. R.; Robie, S. B.; Louer, D.; Gobel, H. E.; Will, G.; Gilles, R.; Raftery, T. *Powder Diffr.* **1995**, *10*, 91–95.
[89] Gemeinhart, R. A.; Guo, C. In *Reflexi*V*e Polymers and Hydrogels*; CRC Press, LLC: Boca Raton, FL, 2004, pp 245-257.
[90] Tourinho, F. A.; Campos, A. F. C.; Aquino, R.; Lara, M. C. F. L.; da Silva, G. J.; Depeyrot, J. *Braz. J. Phys.* **2002**, 32.
[91] Wiedenmann, A. *J. Appl. Crystallogr.* **2000**, *33*, 428–432.
[92] (22) Keller, T.; Krist, T.; Danzig, A.; Keiderling, U.; Mezei, F.; Wiedenmann, A. *Nucl. Instrum. Methods Phys. Res., Sect. A* **2000**, *451*, 474–479.
[93] Wiedenmann, A. *Physica B* **2001**, *297*, 226–233.
[94] Wiedenmann, A. In *Lecture Notes in Physics*; Odenbach, S., Ed.; Springer: Berlin, 2002, pp 33-61.
[95] Pezron, I.; Djabourov, M.; Leblond, J. *Polymer* **1991**, *32*, 3201–3210.

[96] Debye, P.; Bueche, A. M. *J. Chem. Phys.* **1948**, *16*, 573.
[97] Benguigui, L.; Boue, F. *Eur. Phys. J. B* **1999**, *11*, 439–444.
[98] Vesperinas, A.; Eastoe, J.; Wyatt, P.; Grillo, I.; Heenan, R. K. *Chem. Commun.* **2006**, *4407*, 4409.
[99] Bartlett, P.; Ottewill, R. H. *J. Chem. Phys.* **1992**, *96*, 3306–3318.
[100] Hayter, J. In *Physics of Amphiphiles: Micelles, Vesicles and Microemulsions*; DeGiorgio, V., Corti, M., Eds.; North Holland: Amsterdam, 1983, pp 59-93.
[101] Hayter, J. B.; Penfold, J. *Mol. Phys.* **1981**, *42*, 109–118.
[102] Raghavan, S. R.; Kaler, E. W. *Langmuir* **2001**, *17*, 300–306.
[103] Schubert, B. A.; Kaler, E. W.; Wagner, N. J. *Langmuir* **2003**, *19*, 4079– 4089.
[104] Carretti, E.; Salvadori, B.; Baglioni, P.; Dei, L. *Studies in Conservation* **2005**, *50*, 1–8.
[105] Carretti, E.; Dei, L.; Baglioni, P. *Langmuir* **2003**, *19*, 7867–7872.
[106] Liu, Y. C.; Baglioni, P.; Teixeira, J.; Chen, S.-H. *J. Phys. Chem.* **1994**, *98*, 10208–10215.
[107] Wiedenmann, A. In Lecture Notes in Physics; Odenbach, S., Ed.; Springer: Berlin, 2002, pp 33-61.
[108] Wiedenmann, A. J. Appl. Cryst. 2000, 33, 428-432.
[109] Debye, P.; Bueche, A. M. J. Chem. Phys. 1948, 16, 573.
[110] Vesperinas, A.; Eastoe, J.; Wyatt, P.; Grillo, I.; Heenan, R. K. Chem. Commun. 2006, 4407 - 4409.
[111] Bartlett, P.; Ottewill, R. H. J Chem Phys 1992, 96, 3306-3318.
[112] Hayter, J. In Physics of Amphiphiles: Micelles, Vesicles and Microemulsions; DeGiorgio, V., Corti, M., Eds.; North Holland: Amsterdam, 1983, pp 59-93.
[113] Hayter, J. B.; Penfold, J. Molecular Physics 1981, 42, 109-118.
[114] Zemb, T.; Charpin, P. J. Physique 1985, 46, 249-256.
[115] Liu, Y. C.; Baglioni, P.; Teixeira, J.; Chen, S.-H. J. Phys. Chem. 1994, 98, 10208- 10215.